Modeling Paraffin Wax Deposition from Flowing Oil onto Cold Surfaces

by

Luqman Hakim Ahmad Mahir

A dissertation submitted in partial fulfillment
of the requirements for the degree of
Doctor of Philosophy
(Chemical Engineering)
in the University of Michigan
2020

Doctoral Committee:

Professor H. Scott Fogler, Co-Chair
Professor Ronald G. Larson, Co-Chair
Professor Angela Violi
Professor Robert Ziff

Luqman Hakim Bin Ahmad Mahir

luqmanh@umich.edu

ORCID iD: 0000-0002-8117-4023

Dedication

To my parents Ahmad Mahir Razali and Azizah Md. Zain…

Acknowledgements

Segala puji bagi Tuhan sekalian alam yang telah mengizinkan penghasilan dissertasi ini. My journey towards materializing this dissertation has been amazing. I could not have reached this milestone without the support of many wonderful people. First and foremost, I would like to thank my co-chairs, Prof. Fogler and Prof. Larson for their relentless guidance, patience, support, and dedication towards my professionalism. I would also like to acknowledge Dr. Rama Venkatesan at Chevron, Dr. Thierry Palermo, Mohamed Saidoun, Marie Francois, Mayela Rivero, and Khalid Mateen at Total for their support to the flow assurance research at Michigan. I am grateful for the research sponsorship from Chevron, Total, Assured Flow Solutions, and Nalco Champion. Without their financial assistance, this dissertation would not have been possible.

Former members of the Fogler group, Dr. Cláudio Favero and Dr. Sheng "Mark" Zheng have been invaluable allies during this work. I value their insights during all the intellectual discussions we had. I also will never forget the all the times spent together with members of the Fogler and Larson groups.

During my time at Michigan, I have had the opportunity to work with many undergraduate and Master's students. Their contributions to this dissertation are immense, including how they all have shaped the way I think and interact with people. I also cherished the activities we spent together both in the lab, and outside.

Finally, I would like to acknowledge my parents, Ahmad Mahir Razali and Azizah Mohd Zain for their never fading support and love from the other side of the Earth during the course of the preparation of this thesis.

Table of Contents

List of Tables

List of Figures

List of Appendices

Abstract

Paraffins with large molecular weights precipitate out of solution when temperature decreases, forming a three-dimensional network of crystals that can impede oil flow in a pipe, which is undesirable during crude oil production. One way to assess the potential and severity of a paraffin wax deposition is to employ a first principle mathematical model that can predict the growth rate and evolution of paraffin wax gel or deposit as a function of time. In this thesis, a wax deposition model that includes transient heat transfer and transient mass transfer that are coupled was developed.

The model takes the cold finger geometry as a basis and assumes that the heat and mass transfer occur primarily in the radial direction and negligible in other directions while allowing for the possible effects of yield stress on the deposition through a critical solid wax concentration at the deposit-fluid interface, C_{pi}. This new parameter is the precipitated wax concentration needed to withstand the shear stress imposed by the flow at the interface and reflects the dependence of the deposit yield stress on precipitate concentration and the fluid shear stress at the interface. Wax is taken to be a pseudo one-component that can exist in either a molecular (soluble) or precipitated state. Precipitation is described by a first order reaction where the rate law is given by the product of a rate coefficient and the difference between the local soluble wax concentration and the local solubility limit. Precipitated waxes are assumed to not diffuse and can revert back into soluble waxes if the local soluble wax concentration becomes lower than the local solubility limit.

Model predictions were found to be in good agreement with experimental data obtained using a cold finger apparatus. A model oil with a relatively high concentration of wax (in this work composed of 10wt% n-C28 in n-C12), was found able to form gels at a very low precipitated wax concentration where the effect of C_{pi} is insignificant (close to zero), thus as a result the rate of advancement of the gel-oil interface is dominantly controlled by the heat transfer rate. However, even after reaching a steady-state thickness, n-C28 in the bulk oil continues to diffuse into the gel, densifying the gel. This observation signifies that mass transfer must be taken into account regardless of whether heat or mass transfer is controlling the growth rate. It was also found that after reaching the maximum gel thickness, the gel-oil interface can also retreat back and approaches a new steady-state location which is reached at a much slower rate of days to weeks. This retreat of the front was found to be the result of the depletion of wax in the bulk oil. Experiment performed using a dilute wax model oil (in this work composed of 0.8wt% n-C36 in mineral oil) revealed that its gel growth rate is controlled dominantly by mass transfer. In a dilute wax model oil, the concentration of precipitated waxes is so small that a stable gel is unable to form until mass transfer carrying wax molecules from the bulk oil to the cold surface have accumulated sufficient precipitated waxes around the vicinity of the surface. In this regard, the parameter C_{pi} in the model becomes significant (C_{pi} greater than zero).

Chapter 1 Introduction

Despite efforts to replace fossil fuels with renewable energy sources, fossil fuels including petroleum continue to dominate the world energy consumption[1,2]. In 2018, the U.S. Energy Information Administration reported that not only there was a 1% increase in petroleum derived energy consumption compared to 2017, but petroleum also constitutes about 37% of the total energy consumption (Figure 1-1). This trend is expected to increase in the coming years.

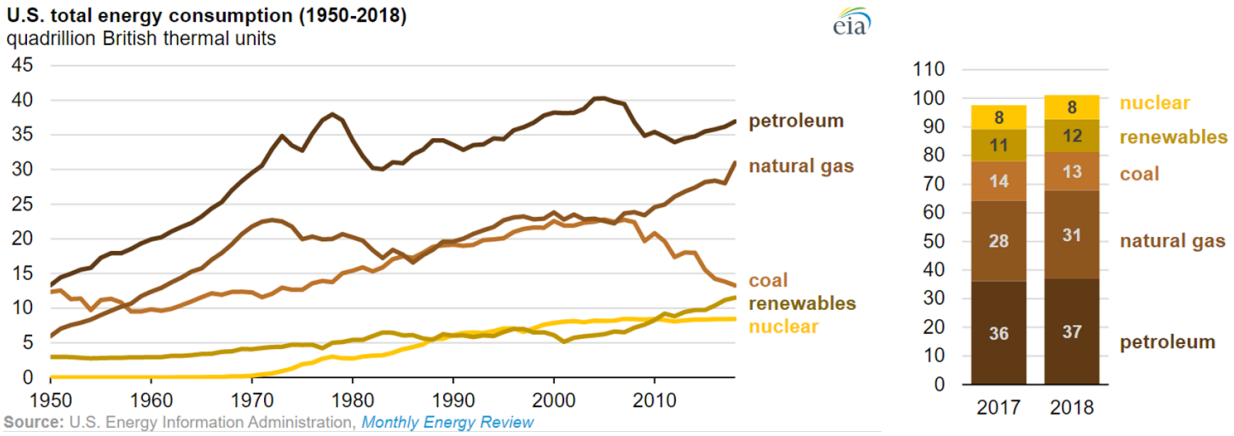

Figure 1-1: Data in the last ten years show a gradual increase in consumption of energy derived from petroleum. Plots were taken from the U.S. Energy Information Administration[3].

Therefore, researches to address existing challenges in oil production such as paraffin wax deposition are still valuable. Paraffin wax deposition inside subsea crude oil pipelines have been a major problem in offshore crude oil production for decades. The terms paraffins and waxes are used interchangeably, and they both refer to a complex mixture of normal and non-normal alkanes, with paraffin carbon numbers ranging anywhere from C5 all the way to C100+. A representative wax molecule is shown in Figure 1-2.

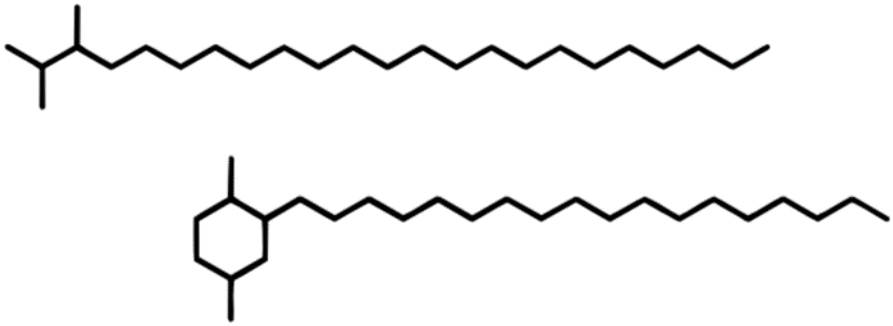

Figure 1-2: Average structure of a paraffin wax[4].

The exact composition depends strongly on the geographical origin of the crude. The precursor to paraffin wax deposition is the formation of crystalline solid due to precipitation of paraffin waxes. Waxes remain dissolved in the oil phase until the temperature drops below their solubility limit where they start aggregating into a three-dimensional network of crystals. Wax crystal networks typically trap other molecules within their pore space that are still in the liquid phase. Such solid-fluid mixtures possess viscoelasticity, plasticity and a yield stress. The yield stress increases with increasing density of solid crystal, eventually forming a solid deposit. Numerous observations show that the incipient layer of a gel contains both solid or precipitation waxes and entrapped fluid phase constituents and that a small precipitated wax concentration is sufficient to form a gel. It is generally accepted that a temperature gradient is necessary to have a gel formation at the inner wall of a pipe. If left untreated, the wax gel will continue to grow until the pipeline becomes clogged. Figure 1-3 shows a location where deposition may occur in a subsea pipeline and a cross-section of a pipe that was not treated after deposition has occured.

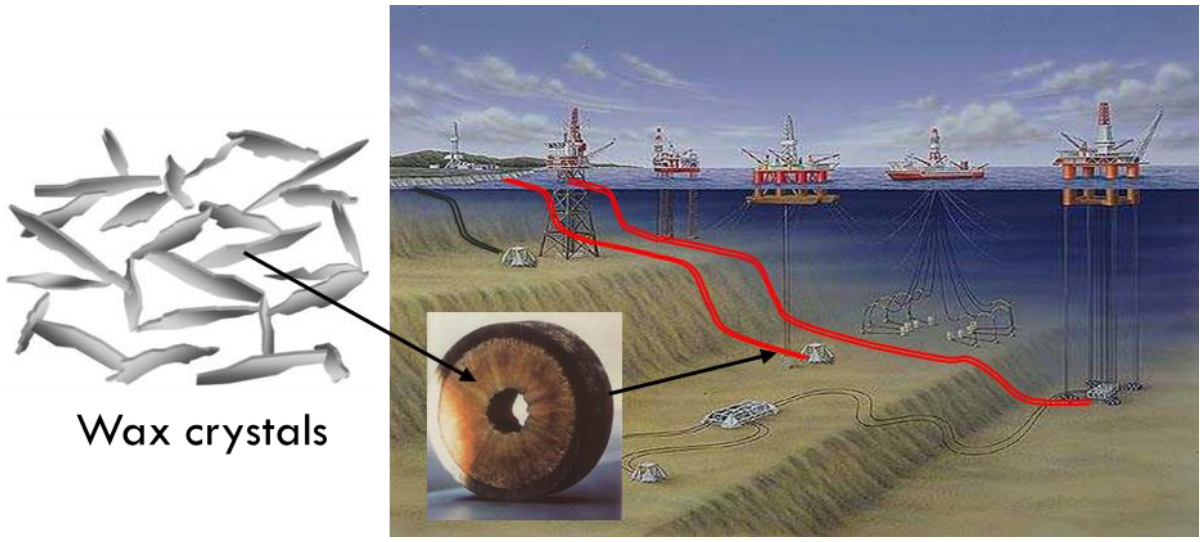

Figure 1-3: Paraffin wax deposition can impede crude oil production.

In the field, crude oil production is usually stopped every so often to give some time for remediation of the inner surface of the pipeline. A device called a Pipeline Inspection Gauge, or pig for short, is inserted from one end of the pipe in a process called pigging. The device scrapes off the wax gel on the wall as it traverse through the pipe and is received at the other end of the pipe. Running this procedure regularly prevents wax gel from growing to an extend that is too thick and too hard to be removed. However, too frequent pigging is inefficient and costly. Because of this very issue, there has been efforts to develop predictive tools that could help optimize pigging frequency. One such tool is a mathematical model based on thermodynamics and transport phenomena that computes wax gel mass or volume as a function of time. This information can then be used to make decisions on the pigging frequency for a particular oil field.

A number of mechanisms have been proposed to be responsible for the formation of wax gel on the inside of a pipeline. These mechanisms are:

- Molecular diffusion[5–8]
- Brownian diffusion[8]

- Shear dispersion[8–10]
- Gravity settling[8,11,12]
- Gelation[5,13–15]

Molecular diffusion of dissolved or soluble waxes takes place when a gradient of soluble wax concentration exists between the center of the pipe and wall. The gradient of soluble wax concentration is established when the temperature is below the Wax Appearance Temperature (WAT) and a temperature gradient exists between the pipe center and the wall. When precipitation occurs, it creates a local region containing a lower soluble wax concentration thus initiating molecular diffusion. As molecular diffusion drives more soluble waxes near the wall, eventually the local concentration of waxes will rise above the local wax solubility limit. More waxes will precipitate out, leading to more molecular diffusion. The accumulation of precipitated waxes at the wall results in the build-up of wax gel or deposit at the wall.

In some situations, the temperature at the center of the pipe can become lower than the WAT, leading to precipitation everywhere in the pipe. Precipitated wax or wax crystals are said to experience Brownian diffusion. The Brownian motion was theorized to transport precipitated waxes from the bulk to the wall. Nevertheless, after the idea was proposed by Burger et al.[8], there has not been any findings to support the importance of this mechanism.

The presence of precipitated waxes also have been hypothesized to distort the flow profile inside the pipe due to the shape and size and wax crystals. In shear dispersion theory, the distorted flow profile allows wax crystals to get transported to the wall, leading to the accumulation of precipitated waxes there. Shear dispersion is also another mechanism that has not been observed to be significant.

When precipitated waxes are present, gravity may play a role in accumulating these precipitates at the lower half of the pipe cross section. Density of wax crystals normally increases with the molecular weight of the wax. However, because the difference in density between the lightest liquid phase wax to the heaviest wax is not significant (lightest ~0.8 g/cm^3, heaviest ~0.9g/cm^3), settling by gravity tends to be slow and negligible. Furthermore, most pipe flows in the field are turbulent, where mixing is very efficient. Settling of wax crystals are only dominant during pipe flow startup and shutdown, as well as in flow in vertical tubes[11,12].

The least discussed mechanism of wax deposition is gelation. In field of flow assurance, gelation has sometimes been used to refer to the general process of paraffin gel formation on a surface, but in the context of this dissertation, gelation is the process whereby the precipitation of waxes near the wall initiates the yielding of the oil flowing near the wall. This yielding event can occur owing to the waxy oil's possession of a yield stress, one of the non-Newtonian characteristics exhibited by waxy oil found through various rheological studies[16–19]. Precipitation of waxes lead to the formation of a structure of wax crystals that are able to resist shear. The greater the concentration of precipitated waxes, the easier it is for the oil to yield.

An effort at modeling gelation during formation of paraffin deposit/gel in a pipeline was made by Zheng et al.[14,15]. In their model, the flow is characterized by the Herschel-Bulkley constitutive equation, with each of the parameter in the constitutive equation being a function of the local precipitated wax concentration. The model keeps molecular diffusion, meaning precipitated wax concentration can accumulate near the wall, leading to a gradual increase in the local yield stress. When the local yield stress exceeds the shear stress being imposed locally by the flow, the local flow ceases. Theoretically, the rate by which the gel grows on the surface should highly depend on how sensitive the yield stress is to the precipitated wax concentration,

among other factors. If an oil possesses a very high yield stress even at low precipitated wax concentrations, the gel formed from this oil should be able to grow very quickly as long as the mass transfer rate can supply sufficient amount of waxes to the wall required for the gelation. Formation of a deposit in this situation is fast and the resulting gel tends to have a composition very similar to the oil that was initially flowing. This process of gelation can be thought of as the freezing of a waxy oil.

Mehrotra and co-workers[20–32] found in various experiments that the gel formation in their systems can be described by a transient heat transfer process and that the composition of the deposits or gels were very similar to the starting oil composition. These observations are very different from other works that mainly focus on molecular diffusion. Although Mehrotra et al. never used the term gelation in their work, these observations seem to suggest the occurrence of gelation where the waxy oil mixture quickly gains a yield stress even at low precipitated wax concentrations. Based on the findings from Mehrotra et al. and other works that support molecular diffusion, there exists a gap in knowledge on what dictates whether gelation or molecular diffusion would be dominant under a particular set of conditions. Addressing this question is important for field scale deposition predictions as the rates of deposition resulting from these two mechanisms can be significantly different.

The goal of this thesis is to advance our understanding of wax deposition mechanism by focusing on the gelation of waxy oil and its interplay with molecular diffusion. Chapter 2 describes the materials and methods used in the experimental studies of this thesis. Chapter 3 studies wax deposition and deposit aging using a cold finger apparatus. Chapter 4 is dedicated to the modeling of the deposition in the cold finger apparatus. In Chapter 5, a new modeling

approach for deposition in a pipe flow is proposed. In Chapter 6, conclusions drawn from the Chapters 2 – 5 are discussed and future directions of research are proposed.

Chapter 2 Materials and Methods

2.1 Model Waxes and Oils

For all of the experiments performed in this thesis, model oils were used instead of actual crude oils. Model oil were prepared by mixing paraffin waxes of choice with a solvent. There are a number of benefits for using model oils. Firstly, the properties of the oil can be easily tuned by adjusting the composition and concentration of the oil's constituents. Secondly, when the waxes are above their solubility limits, the mixture is transparent, allowing visualization of the oil flow. Thirdly, modeling and deciphering the mechanisms of deposition is made simpler because all of the components of the oil are known. While crude oils tend to have other hydrocarbons in them such as asphaltenes which could influence wax deposition characteristics, the most important features of an actual waxy crude oils such as the solubility behavior and molecular diffusion of waxes can still be captured using model oils.

Table 2-1 shows the list of model oils used in the following chapters. The pure n-C28 has a melting point of 64°C. The binary mixture of n-C28 and n-C12 has a Wax Appearance Temperature (WAT) of 32.5°C and n-C28 is the only precipitable component at all experimental conditions (T > 0°C). Figure 2-1 shows the solubility of n-C28 in n-C12 as a function of temperature. The dots represent the experimental measurements obtained by measuring the WAT of mixtures with different n-C28 concentrations. The smooth curve is the solubility curve generated from the thermodynamic model by Coutinho[33]. As can be seen from Figure 2-1, Coutinho's model is reliable in describing the solubility behavior of n-C28-nC12 mixture. This

solubility information is used in Chapter 4 in model predictions. Details on the Coutinho model are provided in Appendix B.

Table 2-1: Composition of Model Oils

Mixture/Material Name	Wax Constituent (s)	Solvent
Pure n-C28	n-C28	-
Binary n-C28/n-C12	n-C28 (10 wt% of mixture)	n-C12 (90 wt% of mixture)
n-C28/mineral oil	n-C28 (10 wt%)	Crystal Plus 70T mineral oil from STE Oil (90 wt%)
n-C36/mineral oil	n-C36 (0.8wt%)	Crystal Plus 70T mineral oil from STE Oil (99.2 wt%)
Septenary mixture	n-C16 (2.1 wt%) n-C20 (1.9 wt%) n-C24 (1.7 wt%) n-C28 (1.6 wt%) n-C32 (1.4 wt%) n-C36 (1.3 wt%)	n-C12 (90 wt%)
Commercial wax mixture (Clarus mixture)	7:2:1 mixture by mass of CSP 123, CSP 138, and CSP 159 from Clarus Specialty Products (10 wt%)	Crystal Plus 70T mineral oil from STE Oil (90 wt%)

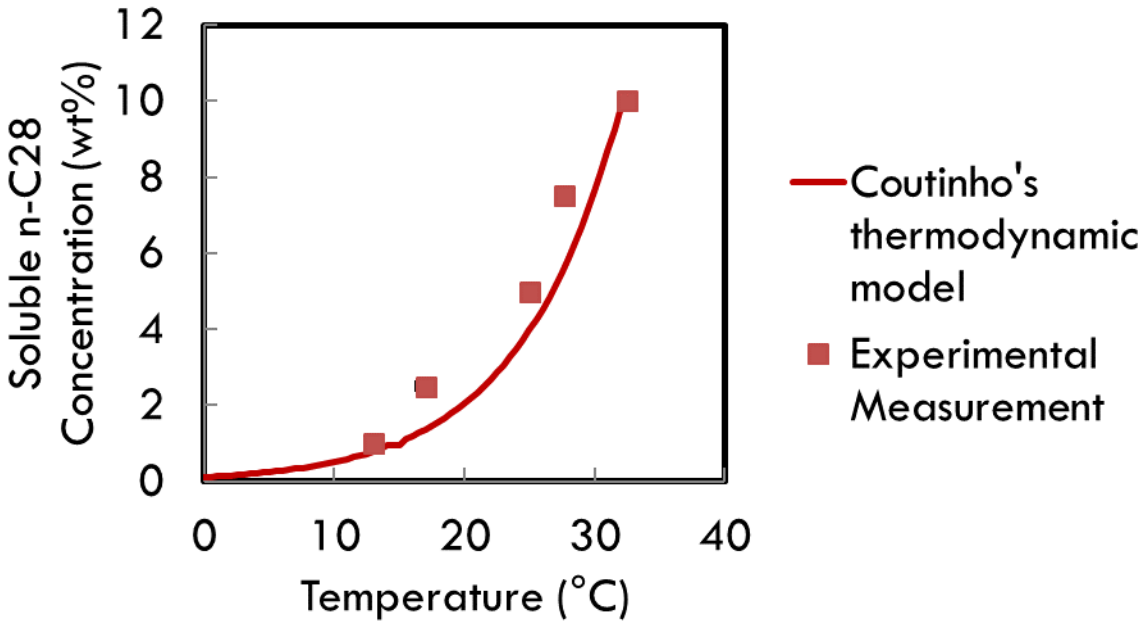

Figure 2-1: Solubility of n-C28 in n-C12

The n-C28/mineral oil and n-C36/mineral oil mixtures are multicomponent in the sense that the solvent has more than one type of hydrocarbon, but the precipitable component remains n-C28 and n-C36, respectively. They both have a WAT of 40°C but very different solubility and concentration of precipitated wax at any given temperature. The n-C36/mineral oil mixture does not form a gel when T > 0°C whereas the n-C28/mineral oil mixture gels at temperatures as high as 38°C. The precipitation curves of these two mixtures are shown in Figure 2-2.

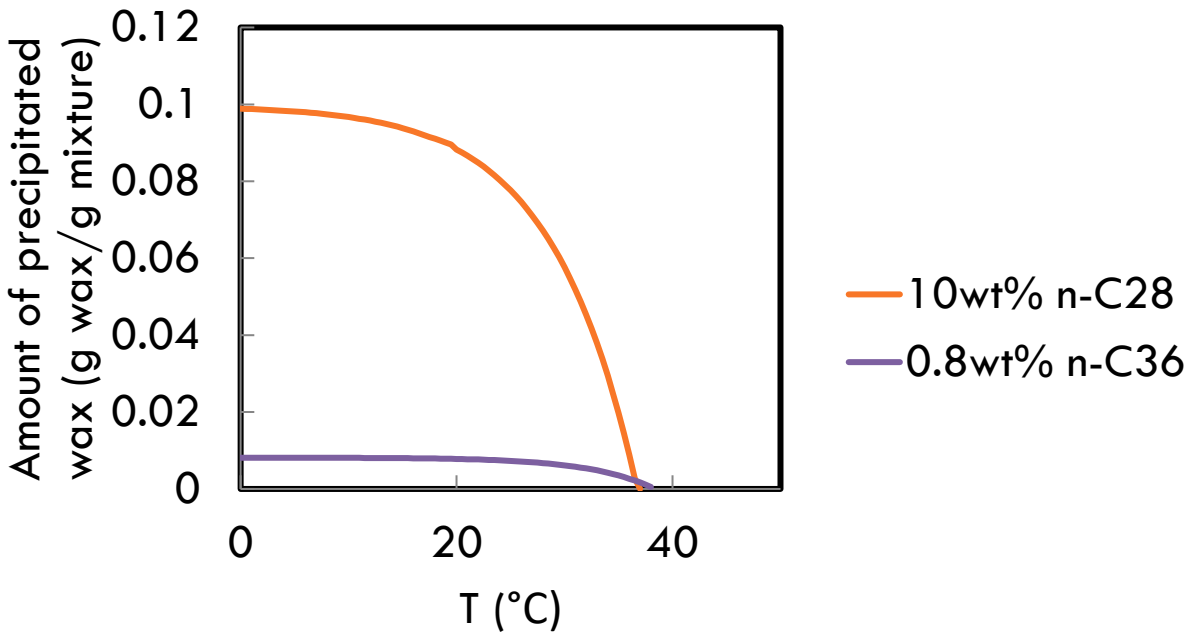

Figure 2-2: Wax precipitation curve of n-C28/mineral oil and n-C36/mineral oil mixtures as computed by the Coutinho model.

Next, two multicomponent wax mixtures were used: a mixture of seven normal alkanes (n-C12, n-C16, n-C20, n-C24, n-C28, n-C32 and n-C36) and a mixture of three commercial waxes with a mineral oil. The three commercial waxes are CSP 123, CSP 138, and CSP 159 mixed in a 7:2:1 ratio by mass and were obtained from Clarus Specialty Products. The mineral oil is a Crystal Plus 70T tech grade white mineral oil from STE Oil. The commercial wax mixture has a log-normal carbon number distribution with a wax carbon number range of C23+ as shown in Figure 2-3. This log-normal carbon number distribution is a characteristic of most crude oils. The septenary model oil has a WAT of 32.5°C whereas the commercial wax model oil has WAT of 34°C.

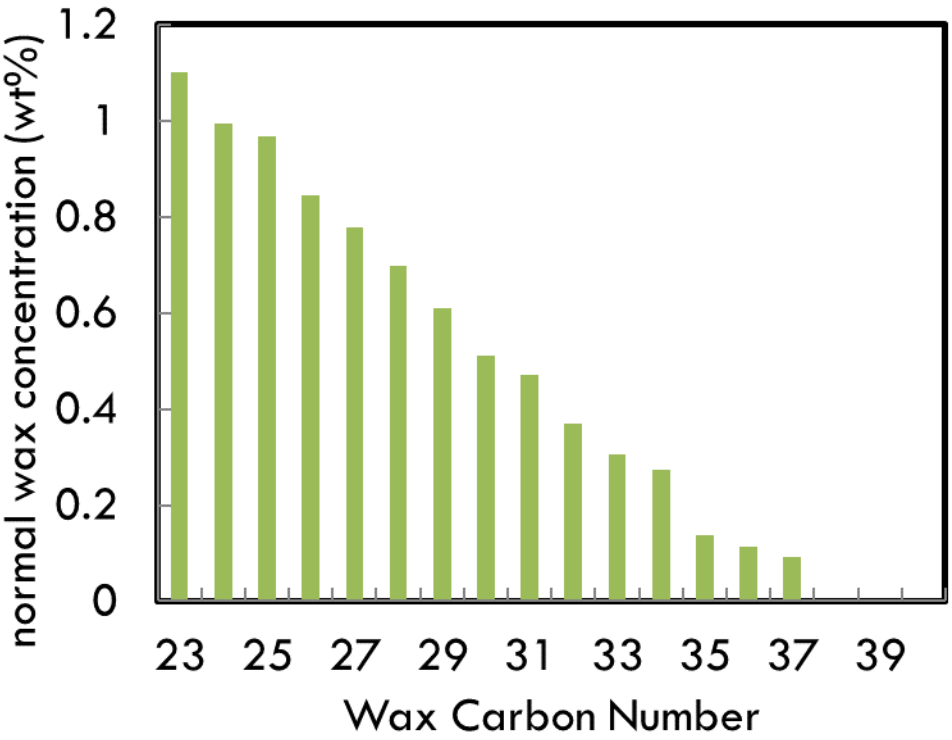

Figure 2-3: Wax carbon number distribution of 10wt% 7:2:1 mixture of Clarus Specialty Products' waxes in Crystal Plus 70T mineral oil

Table 2-1 summarizes the composition of the model oils used across this dissertation.

2.2 Deposition Apparatus and Experimental Procedure

Deposition experiments were carried out using a cold finger apparatus. A schematic of this setup is shown in Figure 2-4(a). The apparatus consists of a 250 mL jacketed beaker containing a model oil with an inner radius of 32.5 mm connected to a circulating water thermostatic bath and a 10 mm outer diameter hollow cylindrical stainless-steel rod (i.e., cold finger) placed in the center of the jacketed beaker. Cooling water flows through the inside of the cold finger, keeping its temperature below the WAT. For a typical experiment, the height of the oil in the jacketed beaker is 70 mm and the height of the stainless-steel rod immersed in the oil is 60 mm. A magnetic stir bar rotating at a fixed rate keeps the temperature of the oil uniform spatially. Six thermocouples were installed, two of which measure the cooling water temperature

entering, $T_{cw,in}$, and leaving, $T_{cw,out}$, the inner side of the cold finger rod, respectively, another two measure the heating water temperature entering, $T_{jac,in}$, and leaving, $T_{jac,out}$, the jacketed beaker, the fifth thermocouple measures the temperature, T_b, located at the radial midpoint between the cold finger outer wall and the jacketed beaker inner wall, and the last thermocouple measures the temperature on the outer surface of the cold finger, $T_{cf,out}$. Figure 2-4(b) depicts the locations of these thermocouples in the experimental setup. Measurements from these thermocouples were used to either calculate heat transfer coefficients or validate model predictions.

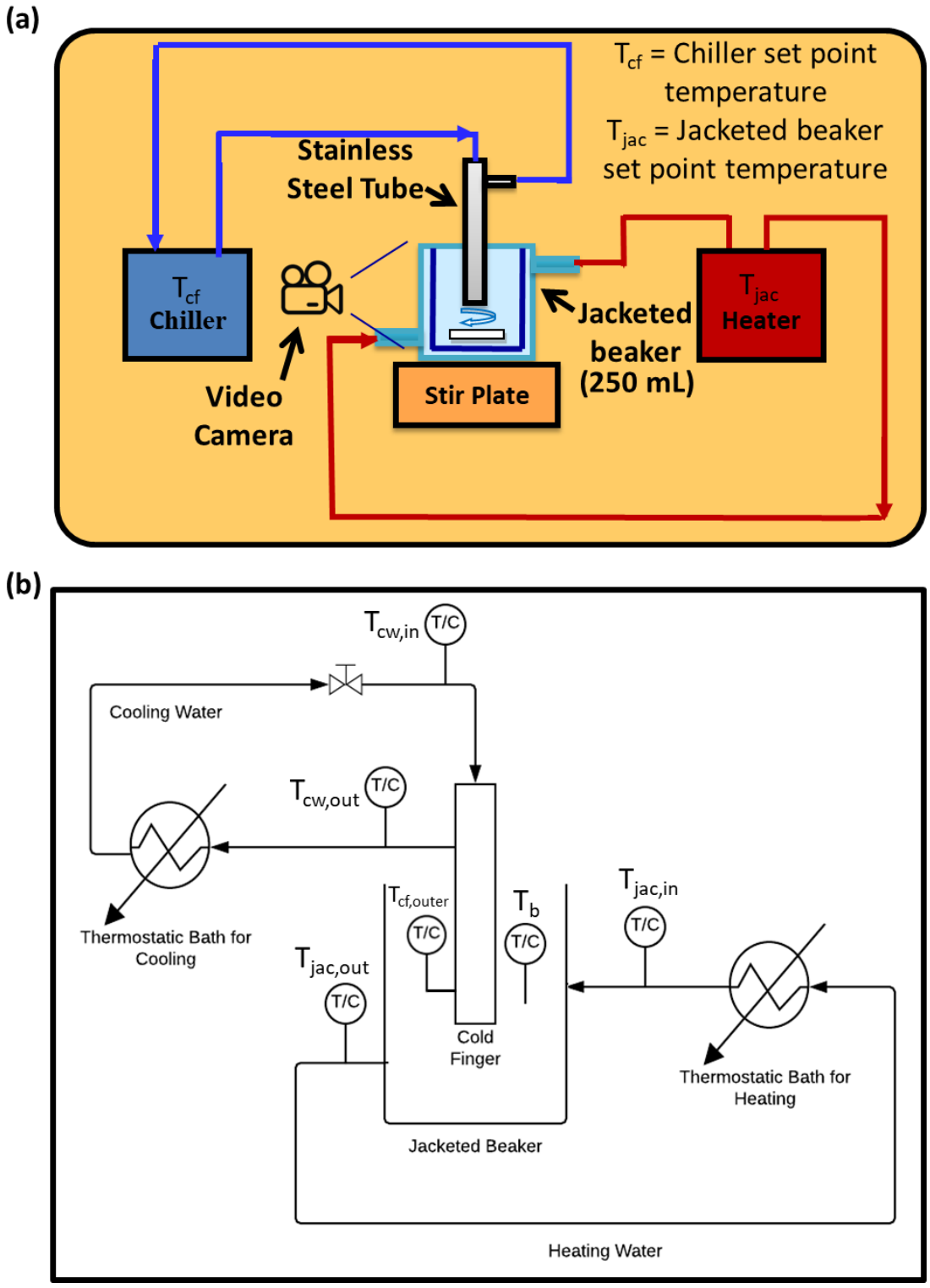

Figure 2-4: (a) Schematics of the cold finger apparatus. (b) Location of six thermocouples in the experimental setup

The temperature of the cold finger thermostatic bath, T_{cf}, and the temperature of the jacketed beaker thermostatic bath, T_{jac}, were set to the desired values prior to the start of deposition. Once thermal steady state was reached, wax deposition was initiated by quickly inserting the cold finger into the jacketed beaker filled with the oil. The deposition was monitored continuously via a video recording. A snapshot of a typical deposit is shown in Figure 2-5. The location of the gel−oil interface (and thus the deposit thickness) was determined from analyzing such images taken from the video recording. This technique was made possible by the clear boundary that exists between the gel and the oil. This technique will not work for oil that is not transparent, which will be the case, for example, if the oil temperature is below the WAT.

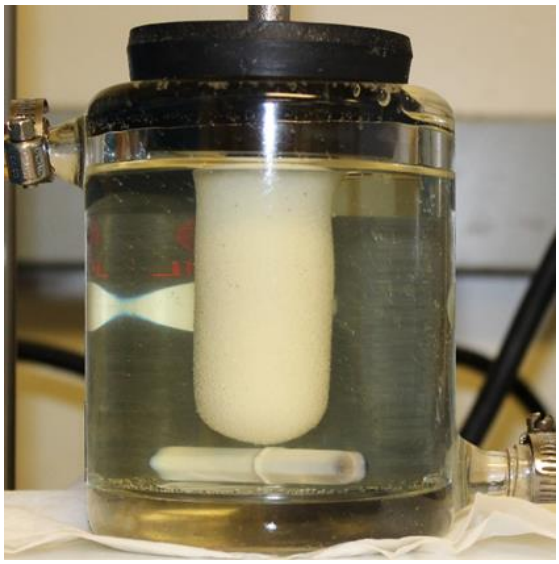

Figure 2-5: A wax deposit forming on a cold finger

To determine how the gel deposit composition changes with time, deposits formed at different times were collected from the cold finger by scraping off 2 mm thickness of the deposit, one from the outer edge, and another from the inner edge of the deposit. When the deposit's total thickness was less than 4mm, the center line of the deposit was used as a standard to collect the samples. High-temperature gas chromatography (HTGC) was used to measure the wax concentration in the deposit. To maintain the uniformity of the samples when injecting them into

the HTGC, samples for the HTGC test were pre-heated using the heating plate prior to HTGC injection.

2.3 Method of Measuring Heat Transfer Coefficients

The experiments to obtain the heat transfer coefficients U_{jac}, U_i, h_i and h_{cf} were performed in the absence of any deposition, i.e. using the wax-free oil. U_{jac}, the overall heat transfer coefficient that characterizes the convective heat transfer rate from the heating water to the stirred oil in the jacketed beaker (without the cold finger), was measured by performing a transient heat transfer experiment. The jacketed beaker filled with a wax-free n-C12 was first equilibrated at 5°C under stirring by flowing cooling water through the jacket at 5°C. The cold jacketed beaker was then quickly connected to a heating water flow with T_{jac} at 35°C. The temperature of the stirred solution, T_b, increased due to the heating and eventually reached a new thermal equilibrium with $T_b = T_{jac}$. An overall energy balance around the oil, shown in Equation (2-1), was then used to fit U_{jac} to the measured time-dependent temperature.

$$\rho \widehat{c_p} V_{oil} \frac{dT_b}{dt} = U_{jac} A_{jac} \left(T_{jac,avg} - T_b\right) \tag{2-1}$$

Here ρ denotes the oil density, $\widehat{c_p}$ the oil specific heat capacity, V_{oil} the volume of oil in the jacketed beaker, A_{jac} the jacketed area, and $T_{jac,avg}$ the average between $T_{jac,in}$ and $T_{jac,out}$, where these two temperatures typically differed by around is 0.2°C. **Error! Reference source not found.** shows how T_b obtained from Equation (2-1) compares to the actual T_b for different oil stirring rates.

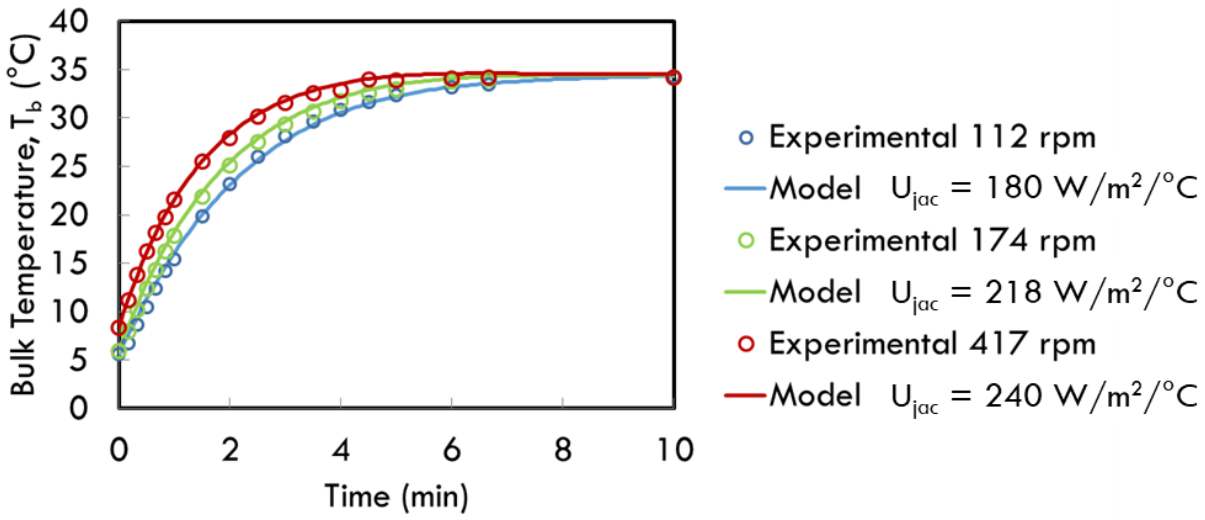

Figure 2-6: Bulk oil temperature, T_b versus time after supplying hot water to the jacket, used to determine the U_{jac} for different stirring rates.

The coefficient h_i characterizes the convective heat transfer rate between the stirred oil and the surface of the cold finger while h_{cf} characterizes the convective heat transfer rate between the inner surface of the cold finger and the cooling water flowing inside the cold finger. Obtaining both coefficients requires first measuring U_i, the overall convective/conductive heat transfer coefficient for heat transported from the stirred oil to the cooling water. U_i was obtained by running the same transient heat transfer experiment as before, except with the cold finger simultaneously immersed in the oil. Equation (2-2) was used to fit U_i to the experimental data.

$$\rho \hat{c_p} V_{oil} \frac{dT_b}{dt} = U_{jac} A_{jac} \left(T_{jac,avg} - T_b\right) - U_i A_{cf,avg} \left(T_b - T_{cw,avg}\right) \qquad (2\text{-}2)$$

Here $A_{cf,avg}$ is the average of the outer and inner surface areas of the cold finger that are immersed in the oil (where there is a 10% difference between the two; i.e., 19 vs. 17 cm^2) and $T_{cw,avg}$ is the average of $T_{cw,in}$ and $T_{cw,out}$, which typically differ by 0-1°C. U_i is not used in the deposition model developed in Chapter 4. Instead, two additional heat transfer coefficients, h_i and h_{cf} are required as discussed in Chapter 4.

The coefficient h_i characterizes the convective heat transfer rate between the stirred oil and the surface of the cold finger, whereas h_{cf} characterizes the convective heat transfer rate between the inner surface of the cold finger and the cooling water flowing inside the cold finger. Both h_i and h_{cf} can be derived from U_i. By the conservation of energy, assuming that the temperatures $T_{cw,avg}$ and $T_{cf,out}$ adjust rapidly to any changes in T_b so that they are at pseudo-steady state, Equation (2-3) holds.

$$U_i A_{cf,avg}\left(T_b - T_{cw,avg}\right) = h_i A_{cf,outer}\left(T_b - T_{cf,out}\right) \tag{2-3}$$

Here $A_{cf,outer}$ is the outer surface area of the cold finger. All of the temperature and surface area terms can be directly measured, and U_i was already obtained through the transient heat transfer test described previously, leaving h_i as the only unknown. Once h_i was determined, h_{cf} was calculated using the well-known analysis of series thermal resistances in series.

$$\frac{1}{U_i A_{cf,avg}} = \frac{1}{h_i A_{cf,out}} + \frac{r_{cf,out} \ln \frac{r_{cf,out}}{r_{cf,in}}}{k_{ss} A_{cf,out}} + \frac{1}{h_{cf} A_{cf,in}} \tag{2-4}$$

where k_{ss}, $r_{cf,out}$, $r_{cf,in}$, and $A_{cf,in}$denote stainless steel thermal conductivity, outer radius, inner radius and inner surface area of the cold finger respectively. We assume that all heat transfer coefficients are unchanged from those for a wax layer depositing onto the cold finger, although we account for the time-dependent increase in $A_{cf,outer}$ due the growth of the deposit layer on the cold finger.

2.4 Method of Measuring Mass Transfer Coefficient

The mass transfer coefficient, k_c was determined by dissolving a pure wax slab into wax-free oil as shown in Figure 2-7. This process can be considered to be the reverse of deposition, in

that soluble waxes migrate into the oil from the pure wax slab as opposed to the reverse of this during deposition.

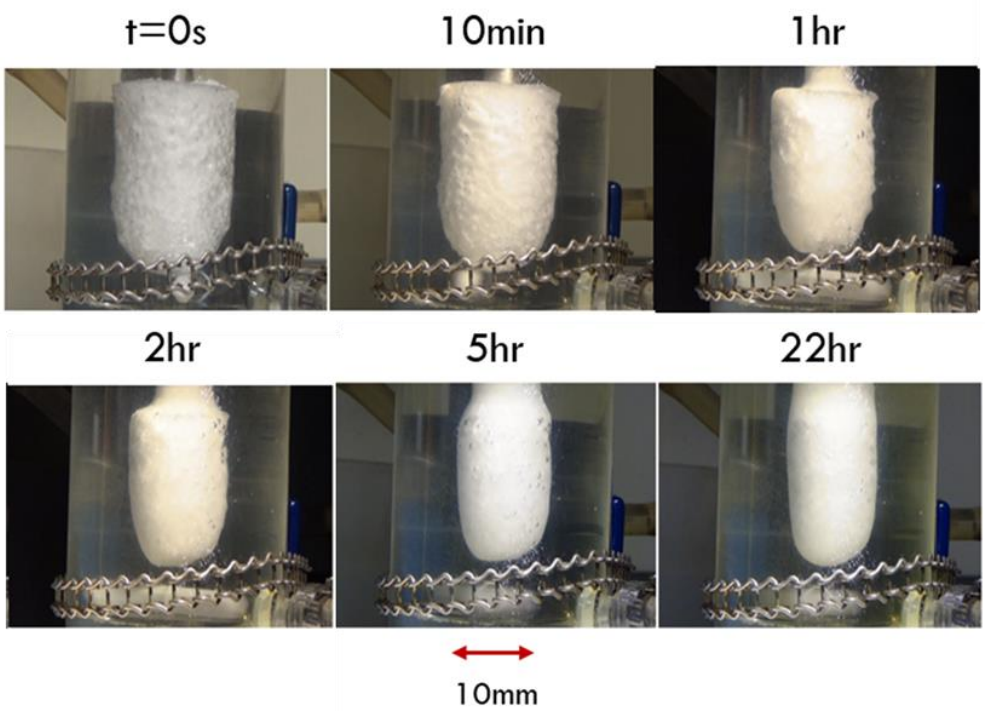

Figure 2-7: Dissolution of a pure n-C28 slab into an initially wax-free n-C12. The solid-liquid interface stops receding when the oil becomes fully saturated.

Equations (2-5) and (2-6), which correspond to the heat and mass balances respectively, evaluated at the slab-oil boundary, can describe the time trajectory of pure wax slab thickness δ during the dissolution.

$$\rho \Delta H \frac{d\delta}{dt} = h_i(T_b - T_i) - k\frac{dT}{dr}_{i^-} \tag{2-5}$$

$$\rho \frac{d\delta}{dt} = k_c\left(C_{sb} - C_{s,eq,i}(T_i)\right) \tag{2-6}$$

where ρ is the density of the pure wax slab, ΔH the specific latent heat of crystallization, h_i the heat transfer coefficient for the convective heat transfer rate at the slab-oil interface, T_i the interface temperature, $\frac{dT}{dr}_{i^-}$ the temperature gradient at the interface on the slab side, C_{sb} the

concentration of soluble wax inside the oil, and $C_{s,eq,i}(T_i)$ the soluble wax concentration at its solubility limit at the interface. C_{sb} is zero at the beginning because the starting oil is wax-free, and $C_{s,eq,i}(T_i)$ is coupled to T_i through the solubility function. Additionally, because thermal equilibrium is attained much more quickly than the time it takes for the slab dissolution to reach equilibrium, at pseudo-steady-state $\frac{dT}{dr_i}_{-} \sim \frac{(T_{cw,avg}-T_i)}{r_{cf,out}+\delta} \frac{1}{\ln\left(\frac{r_{cf,out}}{r_{cf,out}+\delta}\right)}$ is obtained from the steady heat conduction equation in radial coordinates. T_b, T_i, C_{sb}, and δ are all unknowns that evolve with time. The rest of the parameters are constants. To obtain T_b, T_i, C_{sb}, and most importantly δ, Equations (5) and (6), along with an energy balance of the oil and a mass balance of wax in the oil are simultaneously solved.

This technique works well because 1) there is no diffusion inside the pure wax slab, thus simplifying the model, and 2) the rate at which wax dissolves into the oil is always limited by the rate of mass transfer at the interface, allowing k_c to be determined. For this method to work, the rest of the parameters, including the heat transfer coefficients, must be measured or known a priori, allowing the single remaining parameter k_c to be obtained by matching the model prediction to the experimental dissolution profile.

Figure 2-6 shows how a single value of $k_c = 1 \times 10^{-5}$ m/s can describe the dissolution profile at different jacket temperatures at a given stirring rate. If the stirring rate is changed, a new k_c must be re-determined from a dissolution experiment at that stirring rate.

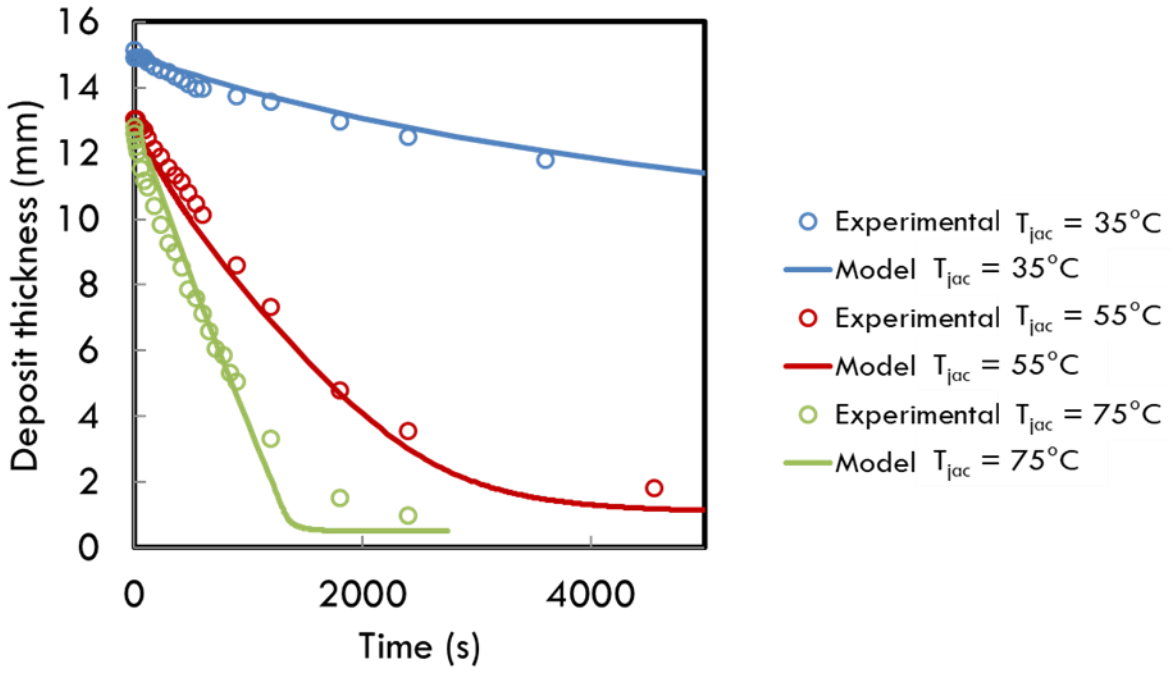

Figure 2-8: Dissolution profiles of n-C28 into n-C12 for different T_{jac} at a stirring rate of 174 RPM. All of the predictions were generated from using $k_c = 1 \times 10^{-5}$ m/s.

Chapter 3 Wax Deposition on Cold Finger

3.1 Introduction

Of the mathematical models developed to predict wax deposition thickness, the model based on molecular diffusion is regarded as the most accurate for predicting wax deposition rates and thicknesses at the industrial scale. One such model is the Michigan Wax Predictor (MWP), which has been validated experimentally in the lab at various temperature and flow conditions through dozens of flow loop studies. However, in some cases relevant for industrial operating conditions, the predicted deposition thickness trajectories were observed to deviate from the actual deposition thickness trajectories, for reasons that remain unclear, but presumably arise from limitations in the molecular diffusion model used[5–7,34]. Consequently, to improve the accuracy and reliability of a wax deposition modeling for industrial use, further investigations of wax deposition mechanisms are necessary.

While the purely molecular diffusion based Michigan Wax Predictor (MWP) model captures the trends of deposition thickness trajectories with varying operational conditions[7,34,35], this model tends to underpredict deposition rates at low operating flow rates and temperatures. At temperatures below the WAT, waxes that precipitate give the waxy oil solid-like properties, including a yield stress, which is the minimum stress that must be applied to the fluid for it to start flowing. At low temperatures and low flow rates, the yield stress of waxy oils is higher than the shear stress imposed by the flow, causing the waxy oil to solidify or gel. Under these conditions, waxy oil solidification tends to be controlled by transient heat transfer, and the deposition rate may be more rapid than that predicted by molecular diffusion. Furthermore, some

studies found that transient heat transfer is sufficient to explain the growth kinetics of some waxy deposits[21,25,32,36]. Assuming that wax deposition can either be heat transfer controlled or mass transfer controlled, we here aim to examine the requirements for a transition between these two mechanisms.

In this study, we employed a cold finger apparatus that has been modified to allow visualization of the deposit formation. Through video recording of the deposit formation process, deposit thickness can be reproducibly measured with an accuracy of ±0.3mm. Using this technique, time resolved evolution of the deposition thickness can be obtained in a less time-consuming manner than the conventional method of measuring deposit mass at the end of a deposition experiment. The full trajectory of the deposition thickness can be obtained from a single experimental run using this technique.

We started first with the simplest system: a pure wax where only a simple single phase transition and heat transfer are the only phenomena involved. We then studied fluids in increasing complexity, from a single-component-wax in a binary mixture, to a seven-component-wax, i.e. septenary model oil, to a multicomponent mixture of commercial wax model oil. The goal was to be able to narrow down the necessary physics involved in the deposition process as well as to observe the progression in their deposition characteristics as oil composition evolves by using known components. This is help us put in the pieces to build a comprehensive model for wax deposition.

In this chapter, the experimental results for the deposition thickness trajectory and deposit composition are presented. The trends of the deposition trajectory were obtained by performing the deposition test at various cold finger temperatures, T_{cf}, and reservoir jacket temperatures, T_{jac}, and stirring rates. The results for deposition from pure n-C28, a binary mixture of 10wt% n-

C28, 90wt% n-C12, n-C28/mineral oil and n-C36/mineral oil, septenary mixture, and commercial wax mixture are presented and discussed in Section 3.2, 3.3, 3.4, 3.5 and 3.6 respectively.

3.2 Pure n-C28 Deposition

Figure 3-1 shows the deposit thickness as a function of time on a semi-log scale for pure n-C28 deposition.

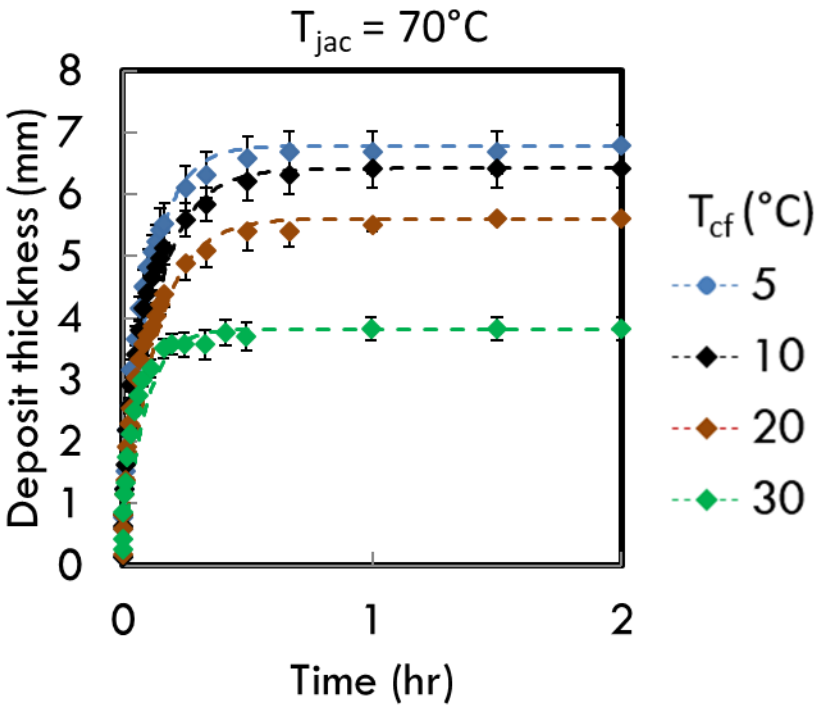

Figure 3-1: Pure C28 experimental deposition thickness versus time at various T_{cf} values while keeping T_{jac} at 70°C. The dashed lines are only guides to the time trajectory trend.

These experiments were performed at different cold finger temperatures, T_{cf}, while keeping the jacket temperature, T_{jac}, constant at 70°C. Deposit thickness increases to a plateau in less than two hours. When the deposit forms on the cold finger, it insulates and decreases the heat flow from the reservoir into the cold finger, eventually balances the heat flow from the jacket to the reservoir, leading to steady state.

The final deposit thickness increases with decreasing cold finger temperature, T_{cf}, as a consequence of an increasing driving force for the heat flow rate into the cold finger.

At any given time or cold finger temperature, T_{cf}, the variation in the axial thickness along the cold finger axis is minimal. This observation shows that the heat flow into the cold finger is nearly axisymmetric despite the complex velocity profile created by the stir bar motion. Consequently, the axial temperature variation can be neglected in the heat transfer modeling. The final deposit thickness increases with decreasing cold finger temperature, T_{cf}, as a consequence of an increasing driving force for the heat flow rate into the cold finger.

Figure 3-2 shows the deposit thickness as a function of time for experiments performed at different jacket temperatures, T_{jac}, while keeping cold finger temperature, T_{cf}, constant at 5°C.

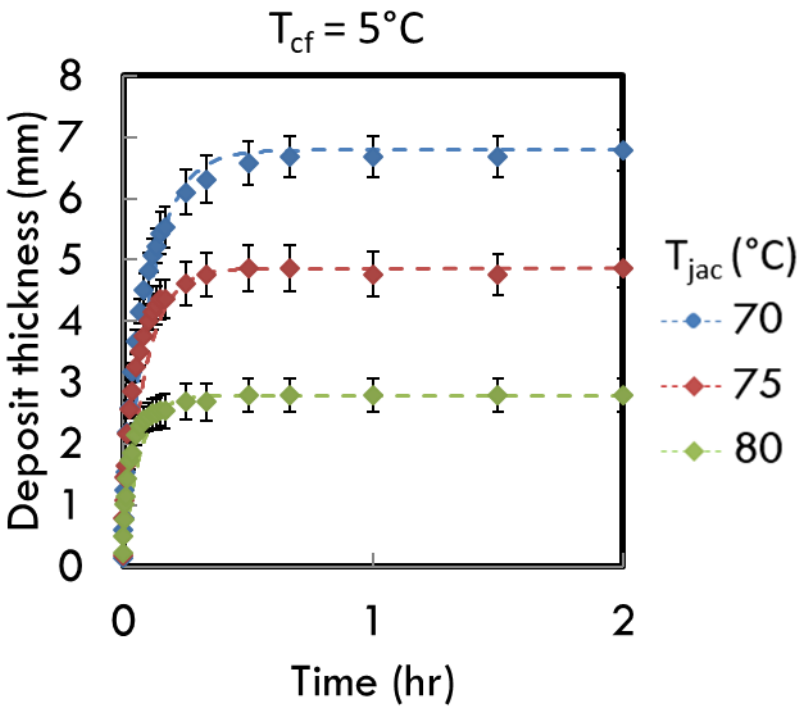

Figure 3-2: Pure C28 deposition thickness versus time at various T_{jac} while keeping T_{cf} at 5°C.

For T_{jac} = 80°C, the final thickness is attained within 15 minutes, while for T_{jac} = 75°C, growth to final thickness requires 40 minutes. For 70°C, one hour is required to achieve the final

thickness. A higher T_{jac} generates a greater heat flow from the heating water in the jacket to the oil in the reservoir, resulting a lower deposit thickness. The temperature of the liquid phase, T_b, was also measured as a function of time, with $T_{cf} < Tb < T_{jac}$ at all times. While varying with time, it was found that T_b is uniform spatially. Figure 3-3 shows the time evolution of T_b for different T_{jac} values while keeping the cold finger temperature, T_{cf}, fixed at 5°C.

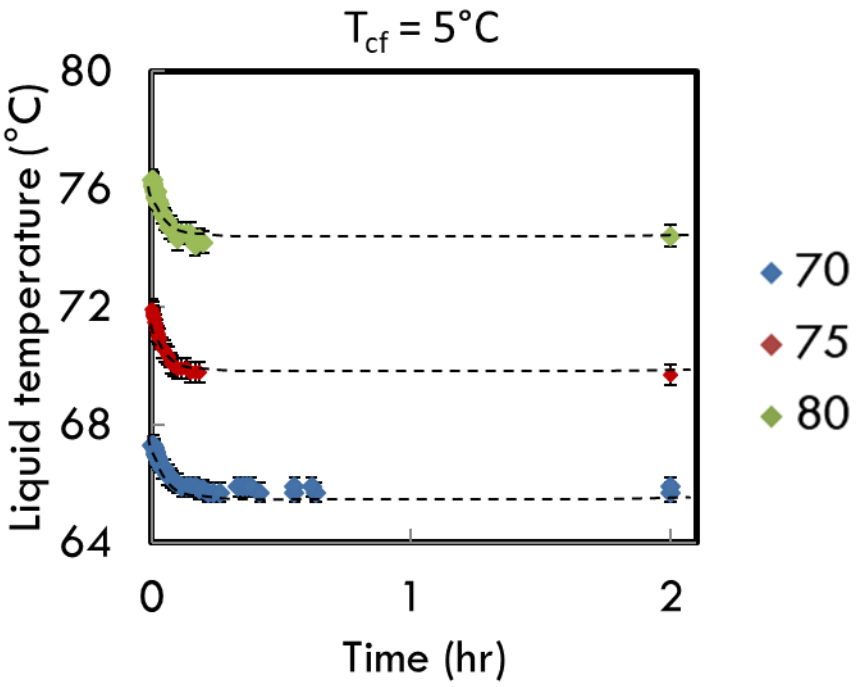

Figure 3-3: Liquid n-C28 temperature, Tb measured during deposition. Shown here are experiments at different T_{jac} while keeping T_{cf} at 5°C.

In all cases the liquid temperature, T_b, decreases then plateaus. The time taken for T_b to reach the steady state value corresponds well to the time taken for the deposit to attain its final thickness. This behavior suggests that the same heat transfer process is driving the changes in the liquid phase temperature, T_b and the deposit thickness.

3.3 Binary n-C28/n-C12 Deposition

Figure 3-4 shows the deposit thickness as a function of time on a semi-log scale for pure n-C28 deposition. The simplest system in which mass transfer effects are important for wax deposition is a binary mixture of one wax component and one solvent component, where the solvent never changes phase within the temperatures of interest. For this part of the study, deposition experiments were performed using a mixture of 10wt% n-C28 and 90wt% n-C12. Figure 3-4 shows the effect of T_{cf} on the deposition history when T_{jac} is kept at 33°C.

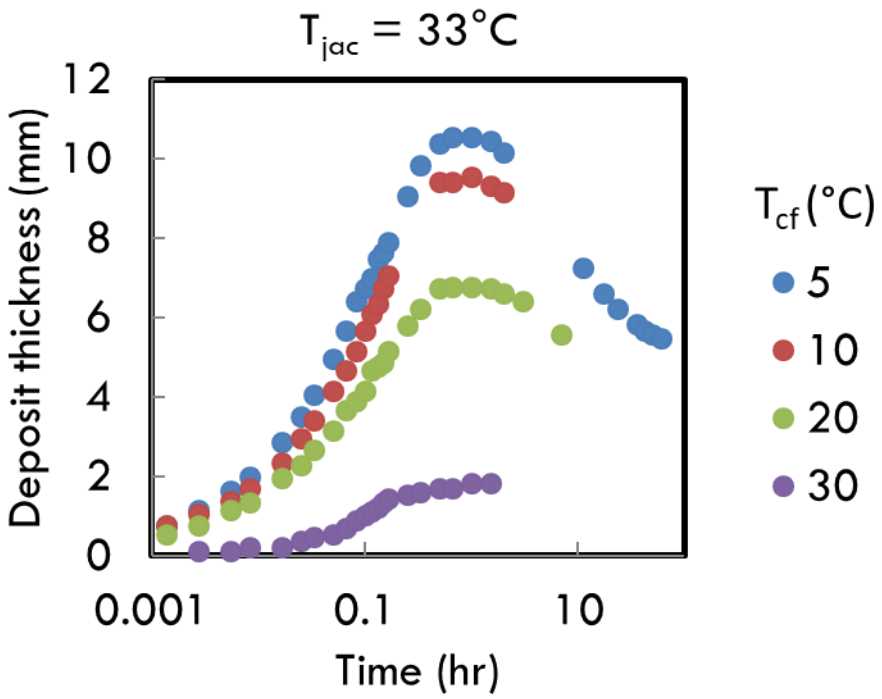

Figure 3-4: Deposition thickness versus time at various T_{cf} while keeping T_{jac} at 33°C. In this and subsequent figures, the starting mixture contains 10wt% n-C28 and 90wt% n-C12.

Except for the case when T_{cf} = 30°C, the deposit thickness increases and then decreases over time. This non-monotonic trend indicates that there are two competing phenomena, one driving the deposit thickness to increase, and another driving a decrease in thickness. Note that at any fixed time, as the cold finger temperature, T_{cf}, decreases, the deposit thickness increases, similar to the trend seen with pure n-C28 deposition.

Figure 3-5 shows the effect of T_{jac} on the deposition thickness trajectory when T_{cf} is kept at 5°C.

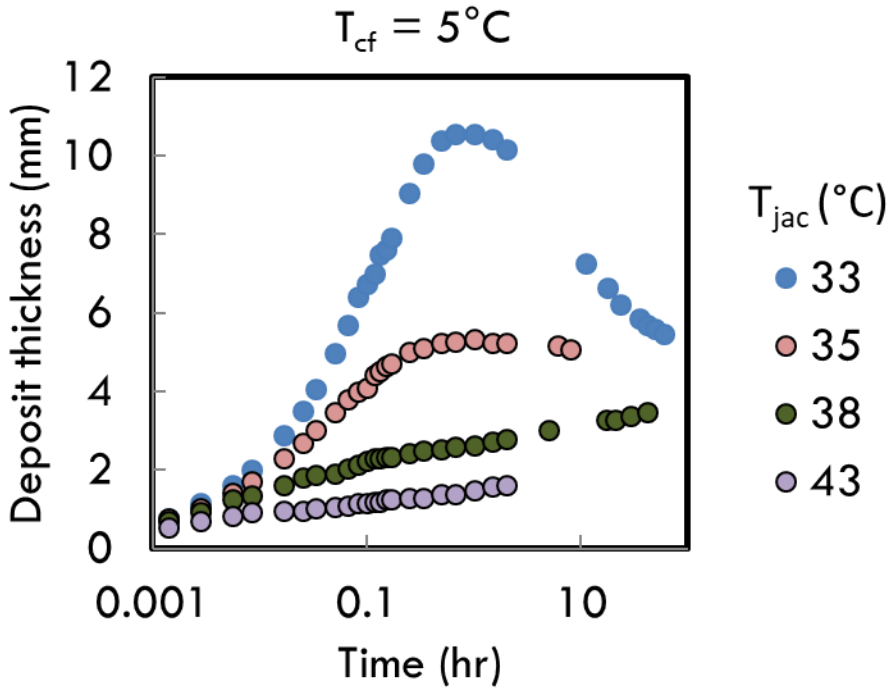

Figure 3-5: Deposition time dependencies at various T_{jac} while keeping T_{cf} at 5°C.

For T_{jac} = 33°C, the deposit thickness increases and then decreases significantly, while for T_{jac} = 35°C, the final decrease is slight. For higher jacket temperatures T_{jac} = 38°C and 43°C, the deposit thickness increases monotonically. At a fixed time, as T_{jac} decreases, the deposit thickness increases monotonically, similar to the trend seen with pure n-C28 deposition.

The composition of the gel was analyzed using HTGC. The gel compositions for T_{jac} = 33°C and T_{jac} = 35°C are shown in Figures 3-6 and 3-7 respectively. In both cases, the concentration of n-C12, which starts out at 90wt%, decreases over time, while the concentration of n-C28, which starts out at 10wt%, increases over time. These results imply that solvent n-C12 is forced out of the gel to make room for n-C28, which diffuses into the gel from the surrounding oil. The inward diffusion of n-C28, in turn, is driven by a concentration gradient of n-C28 in the

oil phase produced by its continuous precipitation within the gel[5,6,37,38]. We note that the concentrations plotted in Figures 3-6 and 3-7 correspond to the concentration of n-C28 and n-C12 in terms of wt% from the total deposit, regardless of whether they are soluble or precipitated.

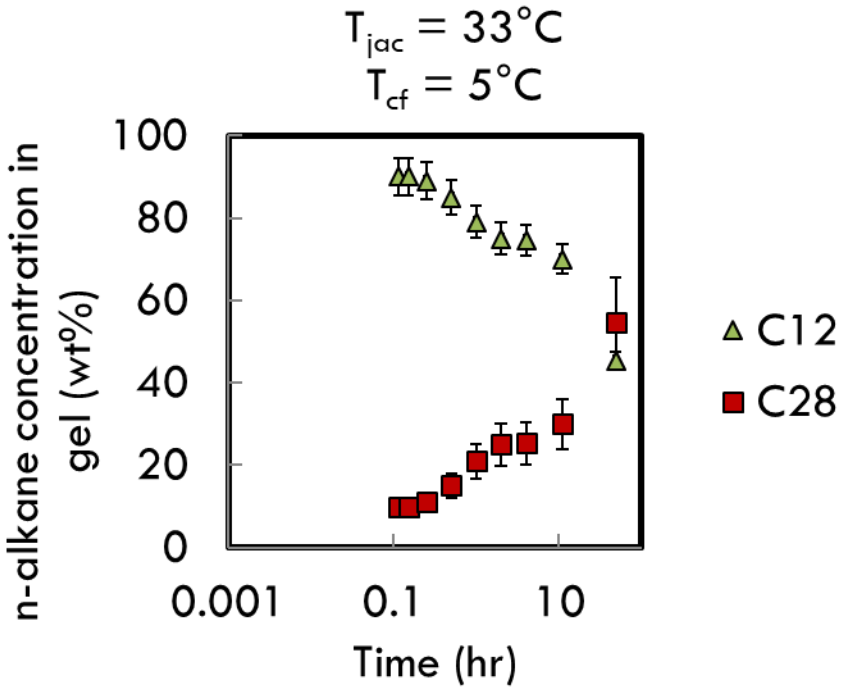

Figure 3-6: The concentrations of n-C28 and n-C12 in the gel resolved with respect to time for T_{jac} at 33°C while keeping T_{cf} at 5°C.

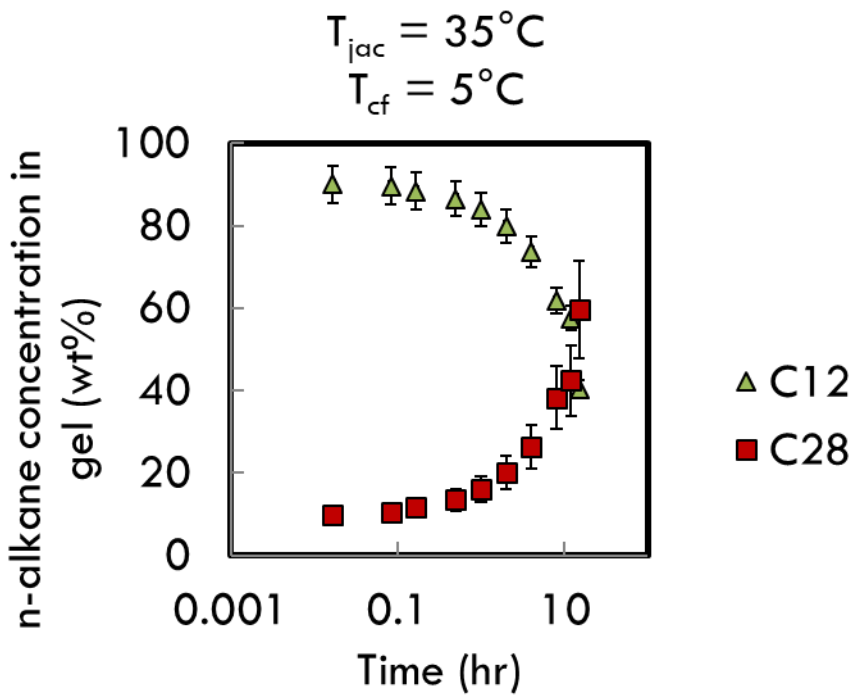

Figure 3-7: The concentrations of n-C28 and n-C12 in the gel resolved with respect to time for Tjac at 35°C while keeping Tcf at 5°C.

In both cases, the n-C28 concentration in the gel remains at nearly the same concentration as that in the oil at 10wt% during the first 0.33 hours (or 20 min) of deposit growth. This observation suggests that, as the oil-wax mixture near the cold finger cools, and the Wax Appearance Temperature (WAT) isotherm moves outwards, the wax behind this isotherm precipitates and forms a gel that simply encompasses the n-C28 and n-C12 present in the oil bulk with little diffusion of n-C28 across this front. However, to confirm the occurrence of this phenomenon, quantitative heat and mass transport analyses must be performed.

Knowing the gel composition, the oil composition can be back calculated because the total masses of n-C28 and n-C12 in the reservoir are known. The C28 concentration in the oil, C_b, was calculated using Equation 3-1:

$$C_b(t) = \frac{m_{c28}(t=0) - m_{c28,gel}(t)}{V_{reservoir} - V_{gel}(t)} \quad (3\text{-}1)$$

where m_{C28} (t=0) is the total mass of n-C28 initially, m_{C28},gel (t) is the mass of n-C28 in the deposit/gel at time t, $V_{reservoir}$ is the volume of the initial mixture, and V_{gel}(t) is the deposit volume at time t. The time resolved n-C28 concentrations in the oil calculated for jacket temperatures of T_{jac} = 33°C and 35°C are shown in Figure 3-8. In both cases, the n-C28 concentration decreases over time as the n-C28 gets diluted or depleted. This depletion of wax is significant due to the finite size of the reservoir containing the oil.

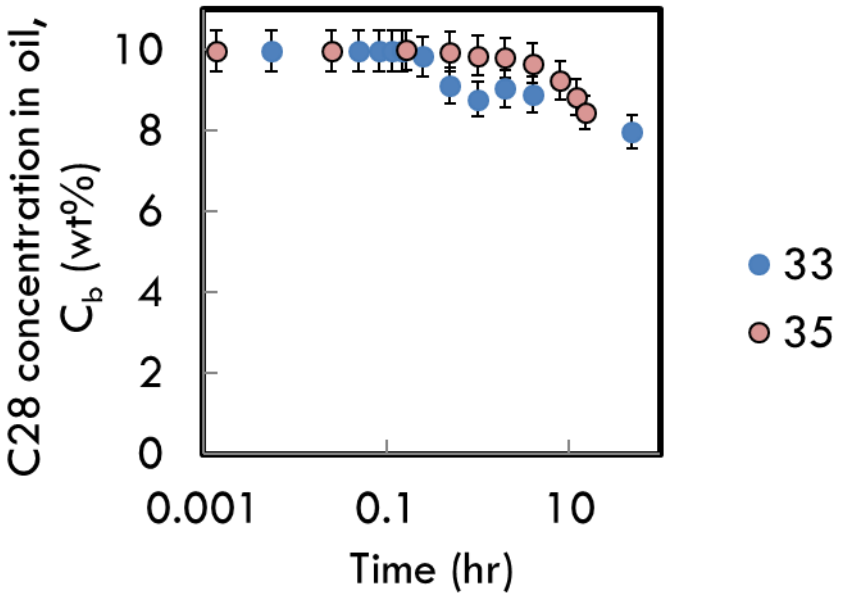

Figure 3-8: n-C28 concentration in the oil back-calculated based on the measured gel composition using Equation 3-1.

This decrease in n-C28 concentration in the oil implies that the WAT of the oil is also decreasing with time. To obtain the WAT of the oil, one can use the solubility curve for the binary mixture of n-C28 and n-C12 to back-calculate the WAT that corresponds to each concentration. The WATs obtained upon performing this calculation on the data shown in Figure 3-8 are plotted in Figure 3-9. One observes that the WAT decreases as much as 2°C.

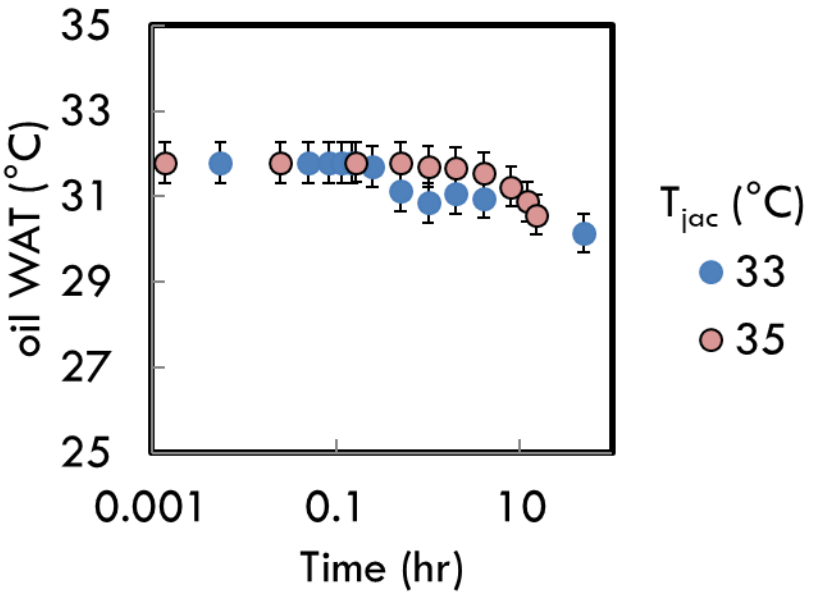

Figure 3-9: WAT of the oil phase back-calculated based on the oil composition.

As mentioned previously, the decrease in deposit thickness over time is expected to be the result of the decreasing WAT in the oil phase over time. To further confirm this effect, an experiment was performed at T_{jac} and T_{cf} of 33°C and 5°C where the oil WAT is kept constant by adding fresh wax to the oil phase at every hour for the first ten hours of deposition, then at every six hours after that. The mass of wax needed at the times chosen were based on the prediction made by the heat and mass transfer model described in Chapter 4. The deposit thickness observed over time in this experiment is compared in Figure 3-10 to that when no new wax is introduced at later times.

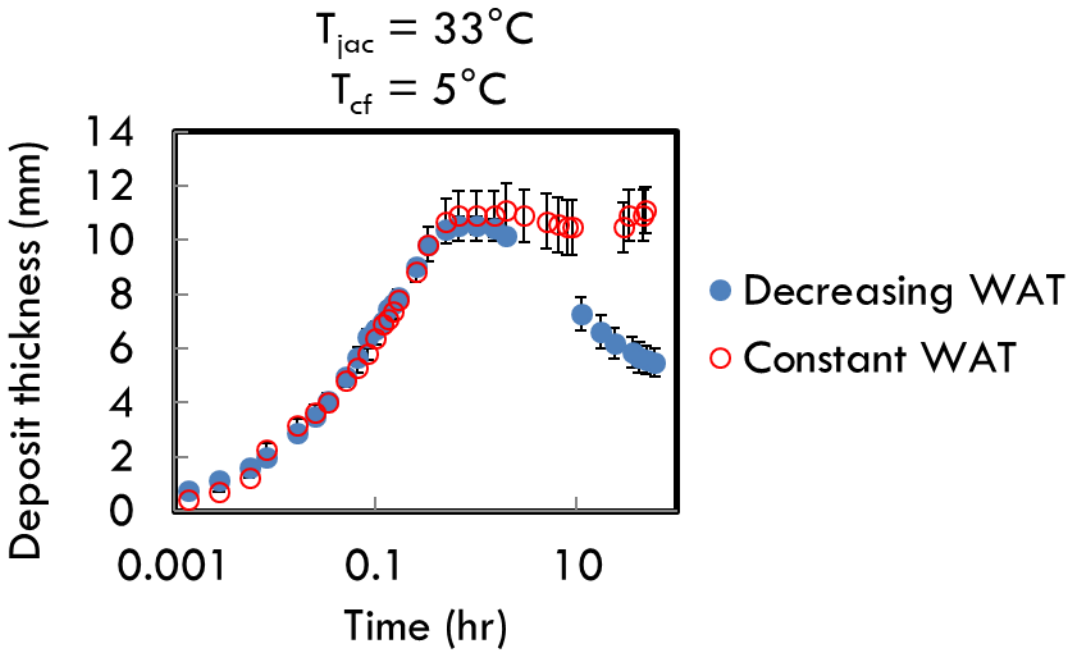

Figure 3-10: Deposit thickness trajectories when oil WAT is maintained by periodic addition of wax to the oil and when oil WAT is allowed to decrease.

When fresh wax is added to maintain the oil WAT, the deposit thickness remains virtually unchanged. This result confirms that the decreasing thickness seen is due to the decreasing WAT of the oil phase.

3.4 n-C28/Mineral Oil and n-C36/Mineral Oil Deposition

In this experiment, T_{jac} and T_{cf} were set to 45°C and 5°C respectively and the stirring rate was kept at 135 RPM. A larger 1L beaker is used in place of the 250mL jacketed beaker to minimize depletion of wax in the reservoir during experiment. Other conditions of the experiment were identical to the previous experiments. Figure 3-11 shows the results of the test.

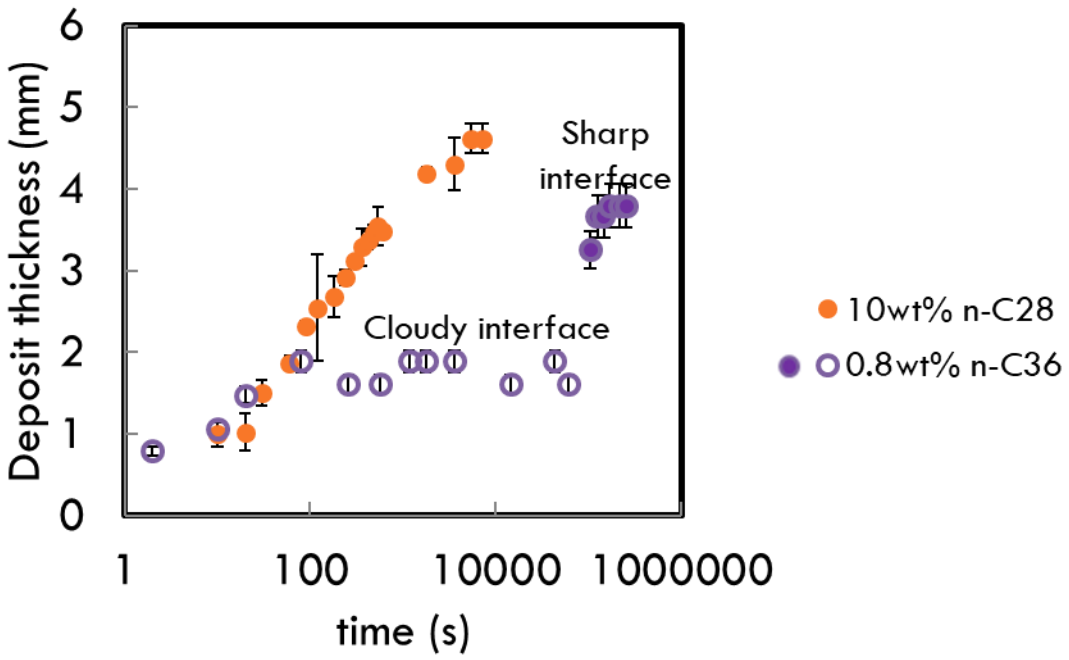

Figure 3-11: Deposit thickness time trajectory for n-C28/mineral oil and n-C36/mineral oil mixtures.

The n-C28/mineral oil mixture acts similarly to the n-C28/nC12 model oil in that there is a well-defined interface that grows monotonically until reaching a maximum thickness. The maximum thickness of 4.5mm was attained at 2.5hrs, slightly longer than the time the n-C28/n-C12 mixture took to reach its maximum thickness due to the higher viscosity of mineral oil compared to n-C12.

It can be seen that the n-C36/mineral oil mixture does not behave like the other model oils tested. Early on ($t < 18$hrs), there was a frequent deposit breakage which resulted in the non-monotonic behavior in the deposit thickness trajectory. The dot symbols in Figure 3-11 are used to signify that the interface is cloudy and slushy, unlike the clear well-defined interface seen in previous experiments. To further demonstrate what was happening, Figure 3-12 shows the snapshots of the cold finger at different times.

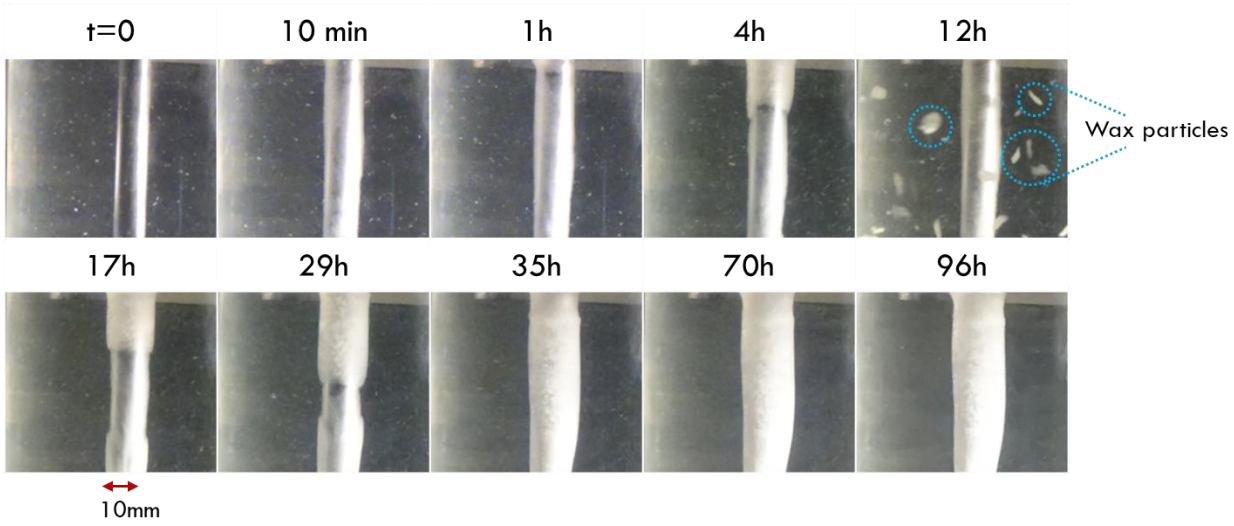

Figure 3-12: Competition between formation and breakage of solid during n-C36/mineral oil deposition.

At times less than 4 hr, any gel layer is thin and not uniformly visible. During these times, we observed that the precipitated waxes were still flowing around the cold finger and back into the oil due to there being insufficient yield stress to withstand the shear. Starting around 4 hr, a gel layer clearly started to form as shown in Figure 3-12. Interestingly, the gel appeared to grow from the ends of the cold finger and not uniformly, indicating a mass-diffusion-limited process. Furthermore, the time taken to observe significant growth is on the orders of hours, far longer that the time taken for heat transfer to equilibrate. At around 12 hr, the deposit broke into large pieces where these pieces eventually re-dissolved into the oil. The deposit eventually grew back and no further breakage was observed.

The behavior of the n-C36/mineral oil is not entirely unexpected. With only 0.8wt% of wax (total amount, not differentiating soluble from precipitated), the mixture does not contain sufficient precipitated wax concentration to form a gel until molecular diffusion supplies enough precipitated waxes to the wall to finally form a gel that can withstand the shear force.

The deposit was also sampled for its composition. From a High Temperature Gas Chromatography (HTGC) test, the n-C36/mineral oil deposit contained 13wt% n-C36 just after the series of breakage and formation ended at t = 20 hrs. This is a significant increase from 0.8wt% n-C36 in the starting mixture. The n-C28/mineral oil mixture however only contained 12wt% n-C28 at 12 hrs, a 2wt% increase from the starting mixture.

Table 3-1: Total wax content in the deposit from the n-C28/mineral oil and n-C36/mineral oil experiments.

Time when deposit was collected	Experimental total n-C36 concentration of deposit (wt%)
24 hr	4.8
96 hr	9.8

3.5 Septenary Mixture Deposition

Deposition experiments using the septenary, i.e. seven-component-wax model oil were performed at various T_{jac} and T_{cf} while keeping the stirring rate at 100 RPM. The results for the deposit thickness as a function of time are shown in Figure 3-13.

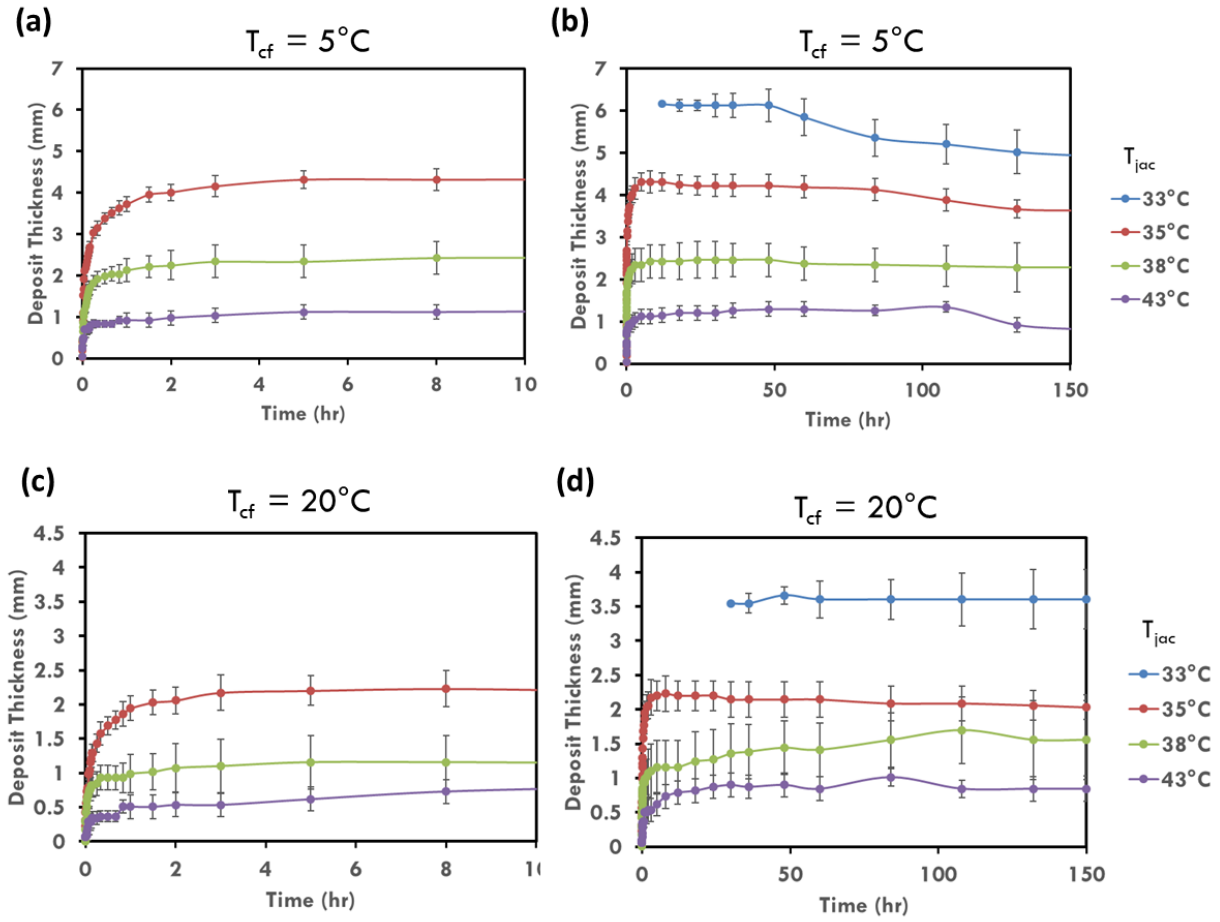

Figure 3-13: The experimental deposit thickness from septenary model oil deposition for (a) the first 10 hrs at different T_{jac}, keeping T_{cf} at 5°C, (b) the first 150 hrs at different T_{jac}, keeping T_{cf} at 5°C, (c) the first 10 hrs at different T_{jac}, keeping T_{cf} at 20°C, and (d) the first 150 hrs at different T_{jac}, keeping T_{cf} at 20°C.

The trends with respect to changing T_{jac} and T_{cf} are consistent with the one would expect from the heat transfer and solubility properties of the model oil. The time needed to reach a steady state deposit thickness is also longer than the binary model oil even though the viscosity of both oils are very similar due to n-C12 being the main constituent. In the binary model oil experiments, the thickness reaches steady state in 30 minutes, whereas here it took anywhere from 2 hrs to few tens of hours to reach steady state thickness. This could be because at the later stage of growth nearing the steady state mass transfer is the controlling mechanism, unlike the binary model oil that was seen to be predominantly heat transfer controlled.

It is also worth noting that at T_{jac} = 33°C, the wax solution was cloudy from the beginning of the experiment up to 10-20 hrs after deposition started. This was because the bulk oil temperature, T_b decreases to slightly below the WAT of the initial oil leading to precipitation in the bulk oil. The deposit thickness was thus unable to be resolved until the solution became clear again. The solution became clear after a while once the precipitated wax in the bulk oil has completely re-dissolved to replace soluble waxes in the bulk oil that have been depleted due to mass transfer into the deposit.

It can be seen that similar to the binary mixture of n-C28 and n-C12, a deposit shrinkage can be seen occurring for the thicker deposit at T_{jac} = 33°C and T_{cf} = 5°C, albeit at a much slower rate when compared to the n-C28/n-C12 mixture deposition despite the very similar viscosity of both mixtures. This is likely because of the lower driving force for molecular diffusion into the deposit leading to a slower mass transfer rate (The total initial wax concentration is 10wt%, the same as the n-C28/nC-12 model oil, but each individual wax has a lower initial concentration). This slower rate of mass transfer as a result of having a lower concentration driving force can also be seen in the deposit composition time evolution, as shown in Figure 3-14 and Figure 3-15.

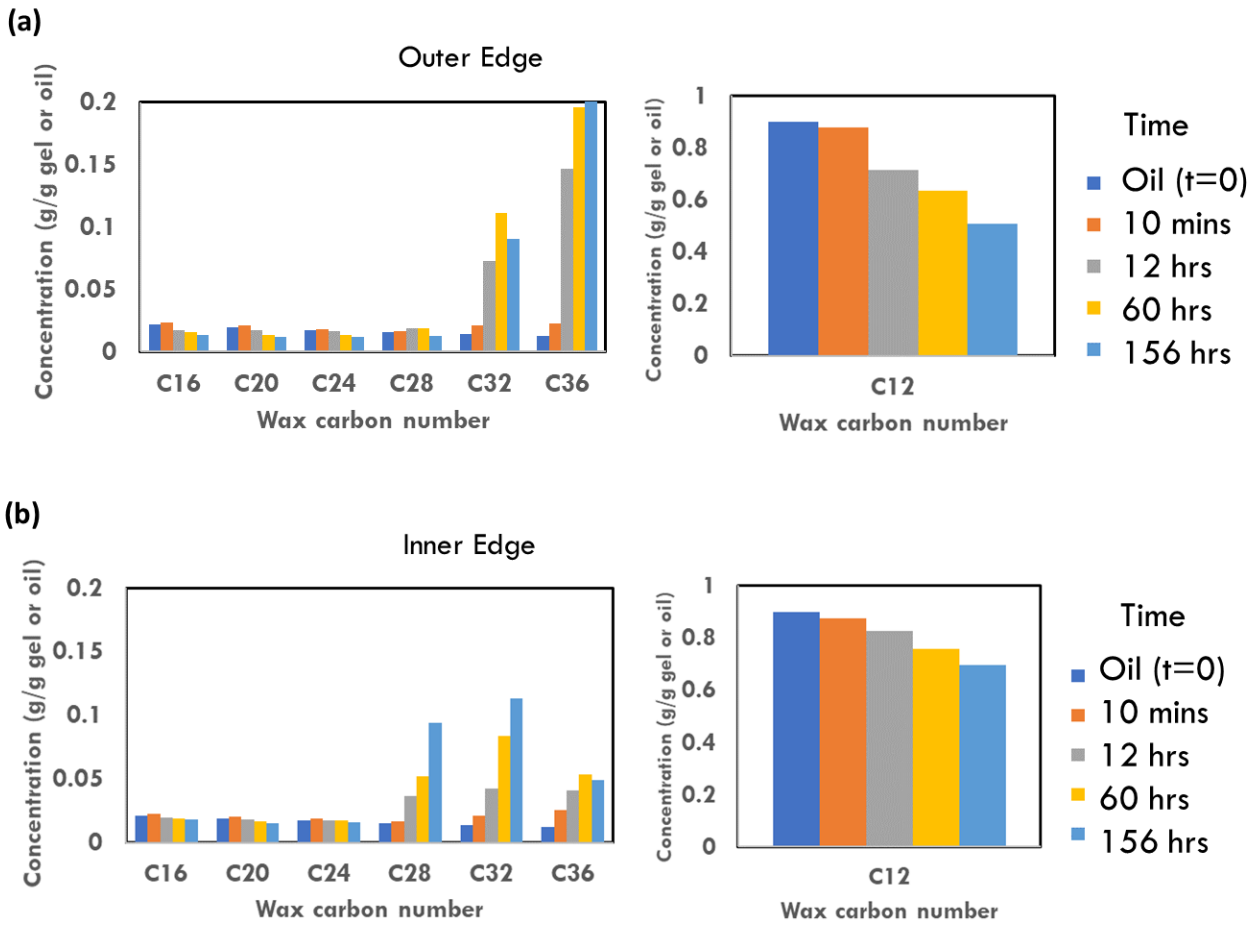

Figure 3-14: Composition of gel (a) in the outer edge, and (b) in the inner edge for the septenary model oil deposition at T_{jac} and T_{cf} of 35°C and 5°C respectively. Composition of the model is shown in the darker shade of blue for comparison.

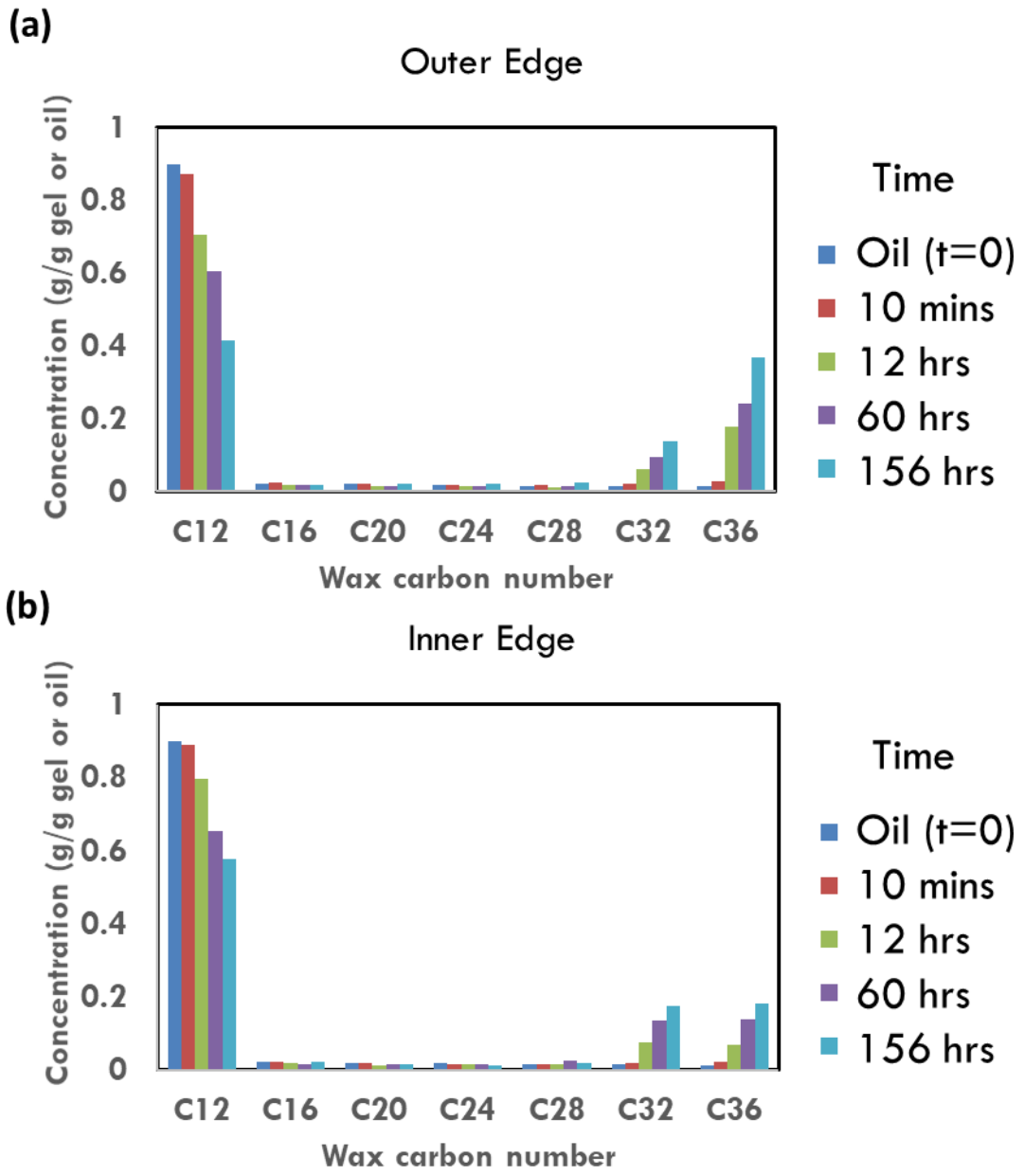

Figure 3-15: Composition of gel (a) in the outer edge, and (b) in the inner edge for the septenary model oil deposition at T_{jac} and T_{cf} of 35°C and 20°C respectively. Composition of the model is shown in the darker shade of blue for comparison.

Both Figure 3-14 and Figure 3-15 show that heavier waxes diffuse into the gel and precipitate, enriching the gel and making it harder, while lighter wax molecules are expelled out of the gel. This trend is similar to other studies that used crude oils or commercial wax model oils[5,6,37–39], demonstrating that simple multicomponent model oils can capture the behavior of

more realistic oils. From the results in Figure 3-14, it can be seen that only n-C32 and n-C36 enrich the entire deposit over time, whereas n-C28 can be seen to only enrich the deposit near the inner edge of the deposit closer to the surface, while lighter waxes were either unchanged or seen leaving the deposit. The likely reason for this is that there is a difference in the precipitation driving force which affects the molecular diffusion driving force. A higher precipitation rate would induce a higher mass transfer rate. n-C36 and n-C32 start precipitating at a higher temperature closer to the WAT than the other waxes, while n-C28 only starts precipitating at a lower temperature, and the other waxes do not precipitate in the temperature range 5°C < T < 35°C, leading to those trends seen in Figure 3-14. We can further seen this behavior by examining the deposit composition at T_{cf} = 20°C, where the temperature profile in the deposit is less steep. Here, n-C28 can be seen to never enrich the deposit, implying that n-C28 does not precipitate above 20°C.

The deposition of the septenary model oil at different oil stirring rate wax also studied and the results of deposit thickness as a function of time are shown in Figure 3-16. Deposit thickness decreases as stirring rate is increased. There are two factors that could potentially explain this behavior. The first reason is that increasing stirring rate enhances the rate of heat transfer from the oil into the cold finger, resulting a thinner insulation layer by the deposit at steady state. The second potential factor is that the higher stirring rate increases the shear stress exerted on the wall, forcing the gel to form at a higher concentration of precipitated wax to withstand the shear stress. Because to get enriched in the composition takes time due to a finite mass transfer rate, the gel growth rate decreases. The direction to take to uncover which of these two are responsible for this observation, a comprehensive modeling approach must be taken.

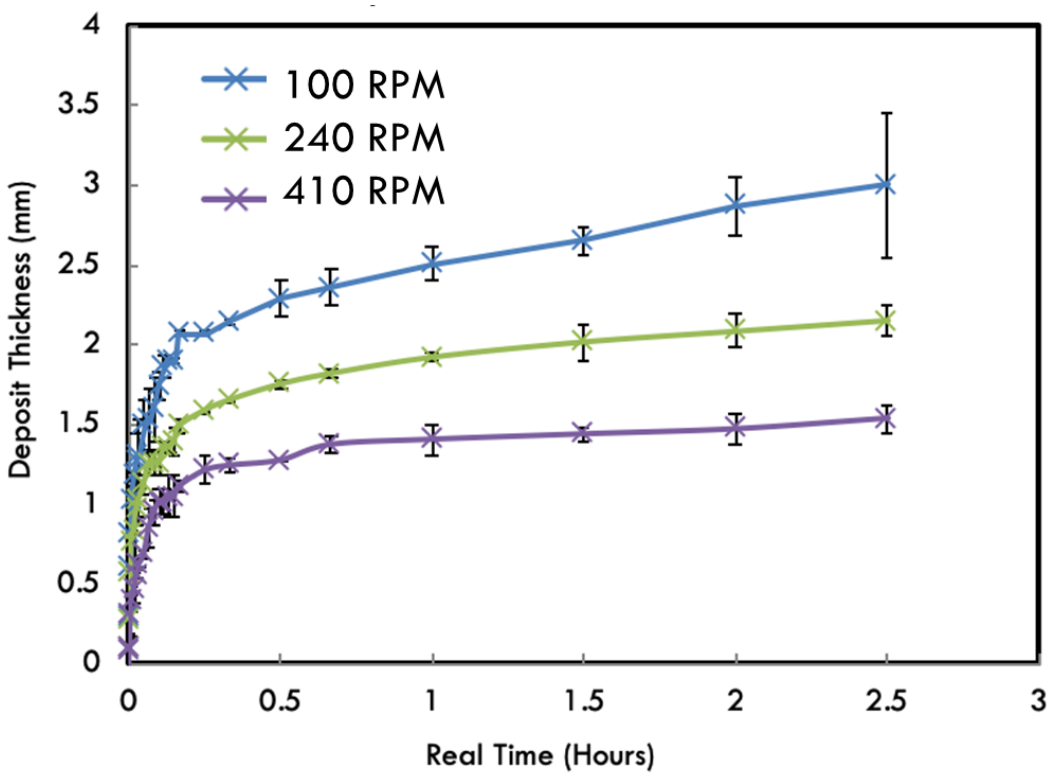

Figure 3-16: The experimental deposit thickness from septenary model oil deposition for the first 3 hrs at different stirring rates keeping T_{jac} and T_{cf} at 35°C and 20°C.

3.6 Commercial Wax Mixture Deposition

The mixture of commercial waxes prepared contains more than 15 wax components. Information on the oil composition and properties can be found in Chapter 2. Mixtures of multicomponent waxes such as this model oil are expected to behave like a weak gel at temperatures below the WAT due to the low precipitated wax concentration, as well as the smaller size of crystals when compared to pure alkanes. As a result, the deposition thickness and deposition rate should be smaller when a higher shear stress is imposed on the gel due to a higher precipitated wax concentration needed to withstand the higher stress. Shear stress can be increased by increasing the flow rate. In a cold finger apparatus, this is equivalent to increasing the stirring rate. A series of deposition experiments was performed at different stirring rates to

investigate the effects of stirring rate on deposition and the results are shown in Figure 3-17 and Figure 3-18. In these experiments, the T_{jac} and T_{cf} were kept at 35°C and 5°C respectively.

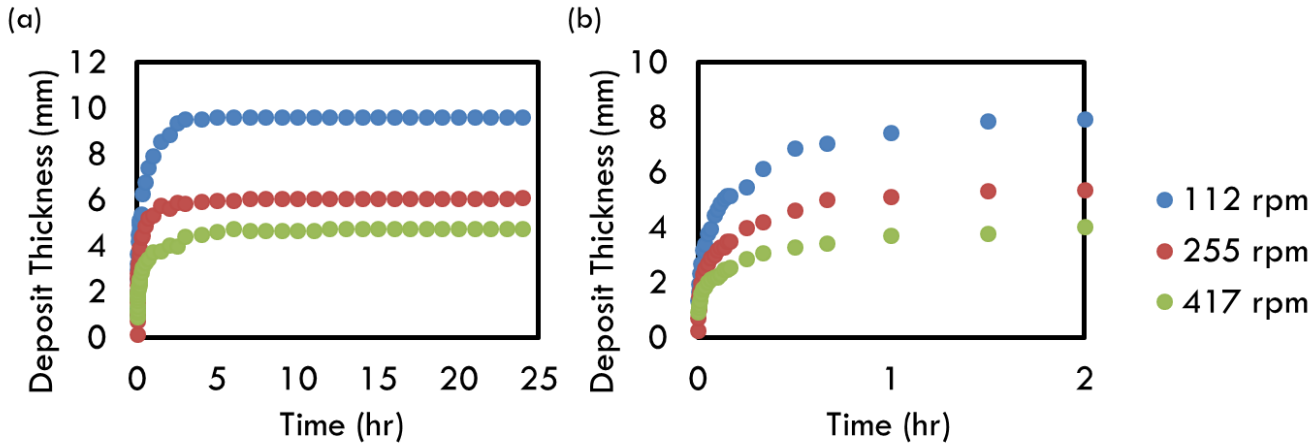

Figure 3-17: Experimental deposit thickness as a function of time for a commercial wax mixture at three levels of stirring rates. (a) Deposit thickness for the first 25 hrs. (b) Deposit thickness for the first 2 hrs).

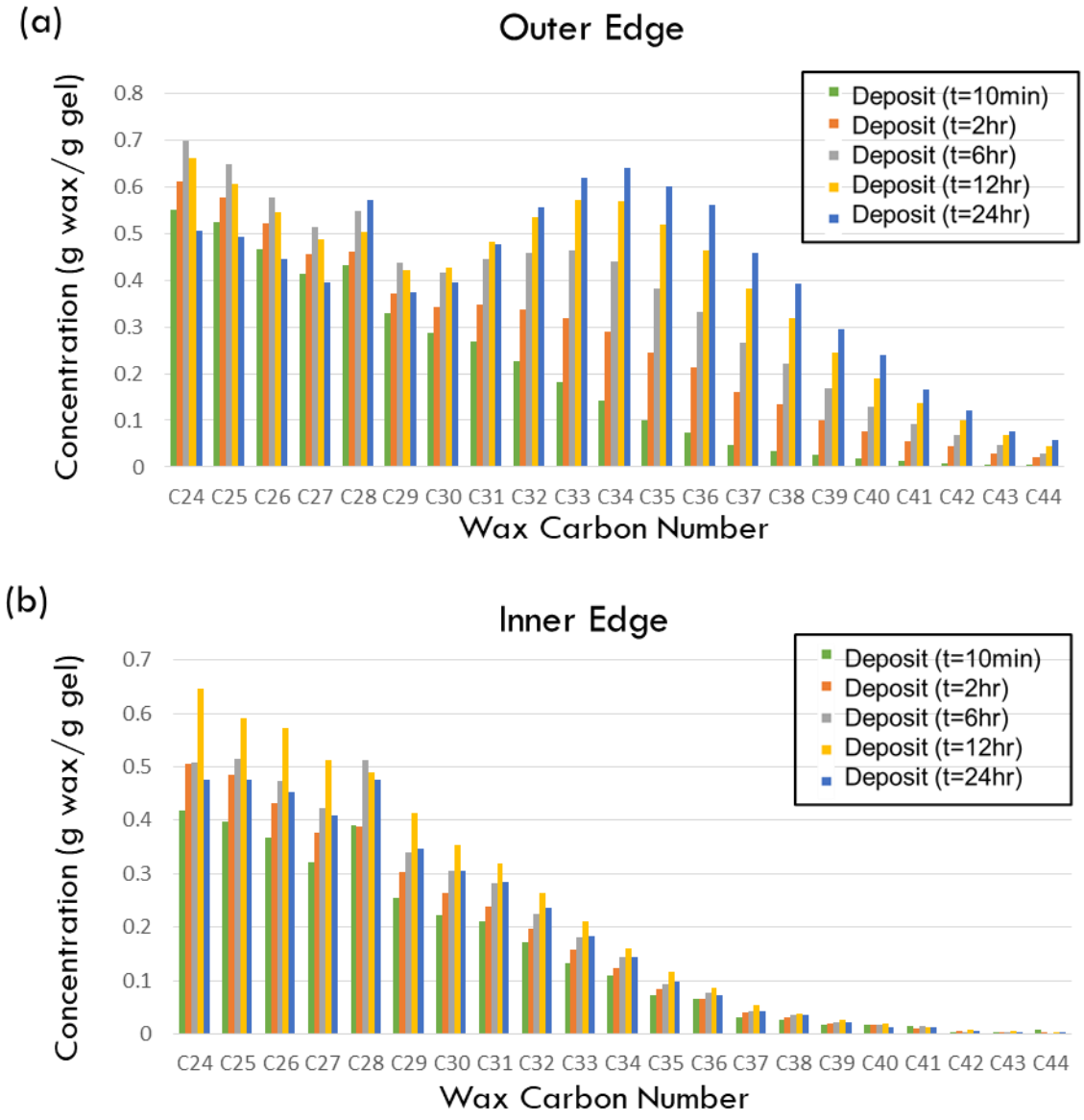

Figure 3-18: Concentration of C24 to C44 waxes in the gel a function of time at (a) the gel outer edge, and (b) the gel inner edge, for a commercial wax mixture at the highest stirring rate of 417 RPM.

Deposit thickness decreases with increasing stirring rate as can be seen in Figure 3-17. Note that this decrease in deposit thickness can be explained by either the effect due to shear stress as discussed earlier, or due to an increase in heat and mass transfer rates induced by the faster stirring, or a combination of both. Figure 3-19 shows how significant the overall heat transfer coefficient of the jacketed beaker, U_{jac} and the wax mass transfer coefficient, k_c are

affected by the stir bar revolution rate. To identify either shear stress effects or increasing heat and mass transfer rates are dominating, a computational study must be carried out with a comprehensive model that resolves the multicomponent mass transfer. The time taken to reach a plateau gel thickness is longer for this commercial wax model oil when compared to the binary mixture tested earlier (5 hrs vs. 30 mins). This is a result of a slower heat and transfer rates in the oil due to its higher viscosity than in the binary mixture (see Figure 3-19). One interesting feature is that over the course of 24 hrs, no deposit shrinkage like that seen with the binary mixture was observed. The shrinkage is negligible in this time frame because either the increased viscosity or the low wax content in the oil slows down the deposit aging significantly.

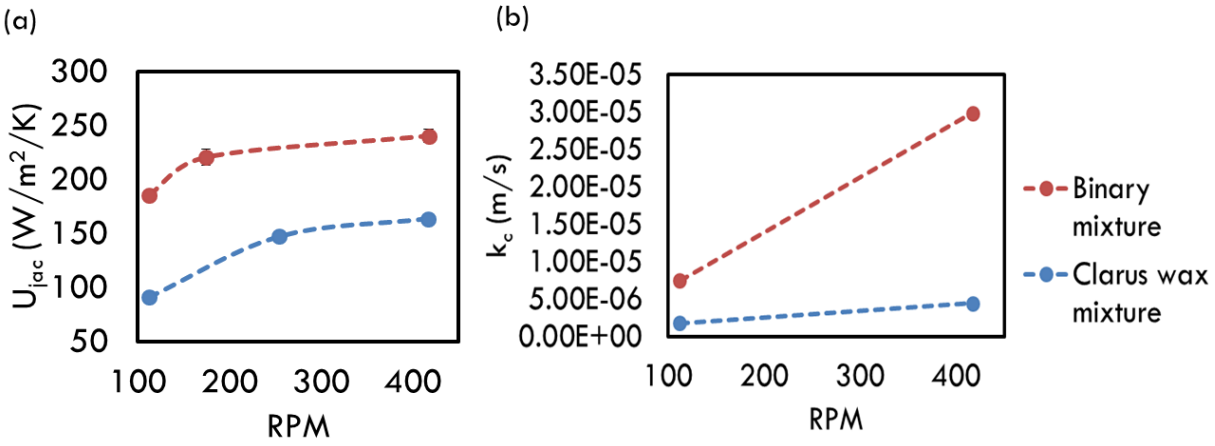

Figure 3-19: Overall heat transfer coefficient and mass transfer coefficient increase with stirring rate.

Figure 3-18 shows how the outer and inner edges of the gel evolve with time at the highest stirring of 417 RPM. It can be seen that heavier waxes enrich the gel at a faster rate near the gel-oil interface compared to the edge next to the cold surface. On the other hand, lighter waxes has the opposite trend in that they enrich the gel at a faster rate closer to the cold surface than at the gel-oil interface. There also exists an optimal wax carbon number whose rate of

enrichment is highest, giving rise to the normal distribution seen in the outer edge composition as a function of time.

The trends observed in Figure 3-18 can be explained by the interplay between precipitation driving force and the molecular diffusion driving force for each individual wax. Heavier waxes start to precipitate at a higher temperature than lighter waxes, and this in turns leads to a higher precipitation driving force at a higher temperature for the heavier molecules. This characteristic gives rise to the trend that heavier waxes only enrich the outer edge because these wax molecules unable to diffuse far into the gel before precipitation occurs where the outer edge is at a higher temperature than the inside. Lighter waxes on the other hand can diffuse further into the deposit before precipitation. While precipitation rate increases the heavier the wax is, the driving force for molecular diffusion to transport the wax molecules from the bulk oil into the gel decreases with heavier waxes. This is because the oil starts out having less heavy waxes than light waxes. This slower diffusion rate competes with the faster precipitation rate, leading the optimal wax carbon number seen in Figure 3-18.

To compare the composition of gel as a function of time at different stirring rates, we compared the concentration of C44 in the gel as shown in Figure 3-20. No data is shown for the gel outer edge C44 concentration for the lowest stirring rate of 112 RPM due to the outer edge sloughing off from the cold finger during any attempt to scrape off the gel. Therefore, only the inner edge of the gel was successfully sampled for the 112 RPM experiment. This sloughing off demonstrates that the gel formed at the lowest stirring rate is weak and is easily subjected to shear, showing the potential for the significance of shear on gel formation. The rate of enrichment of C44 increases with stirring rate as shown in Figure 3-20. However, similar to the gel thickness trend, to identify whether higher heat and mass transfer rates alone can explain this

or if shear stress does have an important role to play can only be ascertained by performing a comprehensive modeling.

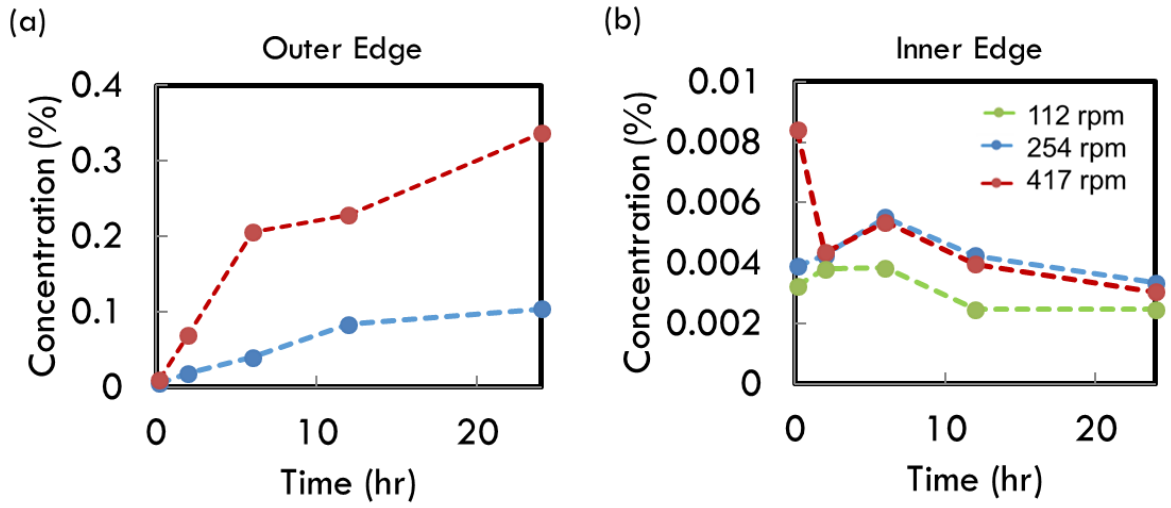

Figure 3-20: Concentration of C44 wax (a) in the gel outer edge, and (b) the gel inner edge at different stirring rates. The lines connecting the points serve as a guide to the trend when time increases.

Chapter 4 Heat and Mass Transfer Model for Wax Deposition on Cold Finger

Wax deposition has been studied at lab scale and two theories have been developed based on experimental evidence. One theory suggests that the growth of wax gel/deposit is dictated by the rate at which soluble wax molecules get transported to the gel-oil interface. This mechanism is characterized by a slow growth of the gel thickness in which the heat transfer becomes pseudo-steady-state, and as a result the gel-oil interface starts out below the Wax Appearance Temperature (WAT), and then rises as the gel grows outward[5,7]. If the gel-oil interface temperature reaches the WAT, which can occur if the oil temperature in the bulk oil is above the WAT, the gel thickness stops growing. However, even if the gel front has stopped moving, molecular diffusion carrying wax molecules from the oil into the gel can continue to take place, leading to the enrichment of precipitated wax over time in the gel for as long as the molecular-diffusion driving force exists. Numerous observations of gel thickness and gel composition as a function of time have supported this mechanism[5,6,39].

The second theory suggests that the gel growth rate is explained simply by a transient heat transfer process[21,27,29,30,32,36,40–42]. This approach equates the migration of the gel-oil interface from a cold finger or from the inner surface of a pipe in a flow loop to the migration of the WAT isotherm (i.e. the gel-oil interface temperature is always at the WAT). This model thus assumes that fluid solidifies as soon as its temperature drops below the solubility temperature at which wax begins to precipitate, such that an arbitrarily small amount of precipitated crystal is sufficient to form a gel and to stop oil from flowing. This approach is able to describe the growth rate of a deposit formed from a binary n-alkane mixture[43] as well as a multicomponent wax

mixture with a sharp bimodal normal distribution of wax carbon numbers[32] because the crystals that form are relatively large and that the solubility curve is steep for these systems. The composition of the deposit was also found to be nearly identical to the oil, at least very early in the deposition, when the gel is still growing. However, this approach is expected to fail to explain deposition from mixtures with a broader and a non-normal carbon number distribution such those found in crude oils where a higher precipitated wax concentration is required to form a gel. Furthermore, when mass transfer is neglected, as assumed by Mehrotra et al., the aging of the deposit, which causes a deposit's hardness to increase with time and sometimes causes the deposit-oil interface location to recede[43], cannot be accounted for.

Both mechanisms predict very distinct gel growth rates; thus a fair question would be: under what circumstances should one model be used over the other? In this work, we would like to address this question by 1) devising a model that includes transient heat transfer and transient mass transfer that are coupled, and 2) examining circumstances under which this comprehensive model reduces to the mass-transfer-controlled or heat-transfer-controlled mechanisms discussed above. This new model can help resolve the conditions under which neglect of various phenomena, such as mass-transfer limitations, pseudo-steady-state approximations, instantaneous crystallization kinetics, and effects of yield stress, might be justified.

In this chapter, two models for the wax deposition in the cold finger are presented. The first model is for pure wax (e.g. n-C28) deposition and second model is for the single-component wax in a solvent (e.g. binary mixture of 10wt% n-C28 in 90wt% n-C12). A list of nomenclatures used is provided in at the end of this Chapter.

4.1 Pure n-C28 Deposition Model

A solid n-C28 deposit will form when the temperature drops below its solidification temperature, T_m. The rate at which liquid n-C28 transforms into solid n-C28 is controlled by the mismatch between the heat flow being conducted away into the cold finger and the heat flow being convected to the solid-liquid interface. Mathematically, this energy balance can be written as

$$\rho \Delta H \frac{d\delta}{dt} = k \frac{\partial T}{\partial r}\Big|_i - h_i(\mathrm{T_b} - \mathrm{T_i}) \tag{4-1}$$

where

ρ is the density of the deposit (kg/m3),

ΔH is the specific latent heat of n-C28 crystallization (J/kg),

δ is the deposit thickness (m),

$\frac{d\delta}{dt}$ is the rate of deposit growth (m/s),

k is the thermal conductivity of n-C28 (W/m/°C),

$\frac{dT}{dr}$ is the temperature gradient at the solid-liquid interface (°C/m),

hi is a heat transfer coefficient (W/m2/°C),

and T_i is the solid-liquid interface temperature (°C).

It is assumed that $T_i = T_m$ at all times. In addition to Equation (4-1) two other transient energy balances are solved, one for the deposit and the other for the liquid. In the deposit, the temperature profile is resolved radially and temporally by solving the energy balance:

$$\rho c_p \frac{\partial T}{\partial t} = k \frac{1}{r} \frac{\partial}{\partial r}\left(r \frac{\partial T}{\partial r}\right) \tag{4-2}$$

where c_p is the specific heat capacity of n-C28 (J/kg/°C).

The boundary conditions applied to Equation (4-2) are shown as follows:

$$\begin{cases} T = T_{cf,m} \text{ at } r = r_{cf} \\ T = T_m \text{ at } r = r_{cf} + \delta \end{cases} \quad (4\text{-}3)$$

where $T_{cf,m}$ is the temperature measured at the cold finger surface (°C), and r_{cf} is the radius of the stainless steel cold finger (m).

In the liquid, although the temperature is uniform spatially, it changes with time and this is taken into account using the following energy balance:

$$\hat{c}_p \frac{d}{dt}\left(m_{liq} T_b\right) = U_{jac} A_{jac}\left(T_{jac,m} - T_b\right) - h_i A_i (T_b - T_i) \quad (4\text{-}4)$$

where m_{liq} is the mass of liquid n-C28 (kg),

$T_{jac,m}$ is the measured temperature of the jacket (°C),

T_b is the liquid phase temperature (°C),

U_{jac} is the heat transfer coefficient for the heat transfer between the jacket and oil ($W/m^2/°C$),

A_{jac} is the jacketed beaker surface area (m^2),

h_i is the heat transfer coefficient for the heat transfer between the oil and the deposit ($W/m^2/°C$), and A_i is the deposit-oil interfacial area (m^2).

Solving Equation (4-4) requires knowing the heat transfer coefficients, h_{jac} and h_i. These parameters were obtained experimentally by measuring the heat flow rate through the apparatus and applying a steady-state energy balance. For instance, in the case of h_i, first, the heat flow rate through the cold finger was calculated using the inlet and outlet temperatures of the cooling water flowing through the cold finger and the cooling water flow rate, all of which were measured. Next, using this heat flow rate, the average between the temperatures of the inlet and of the outlet of the cold finger and the liquid phase temperature, T_b, the heat transfer coefficient hi was calculated. To get the heat transfer coefficient h_{jac}, the same steps were applied on the

heating water jacket. It should be noted these measurements were performed in the absent of any deposition, i.e. $T > T_m$.

4.2 Theoretical vs. Experimental Deposit Thickness – Pure n-C28 Deposition

The experimental transient deposition thicknesses given in Figures 3-1 and 3-2 are now predicted by the model discussed in Chapter 4.1, yielding the comparisons shown in Figure 4-1. Table 4-1 lists the parameters used in the model predictions.

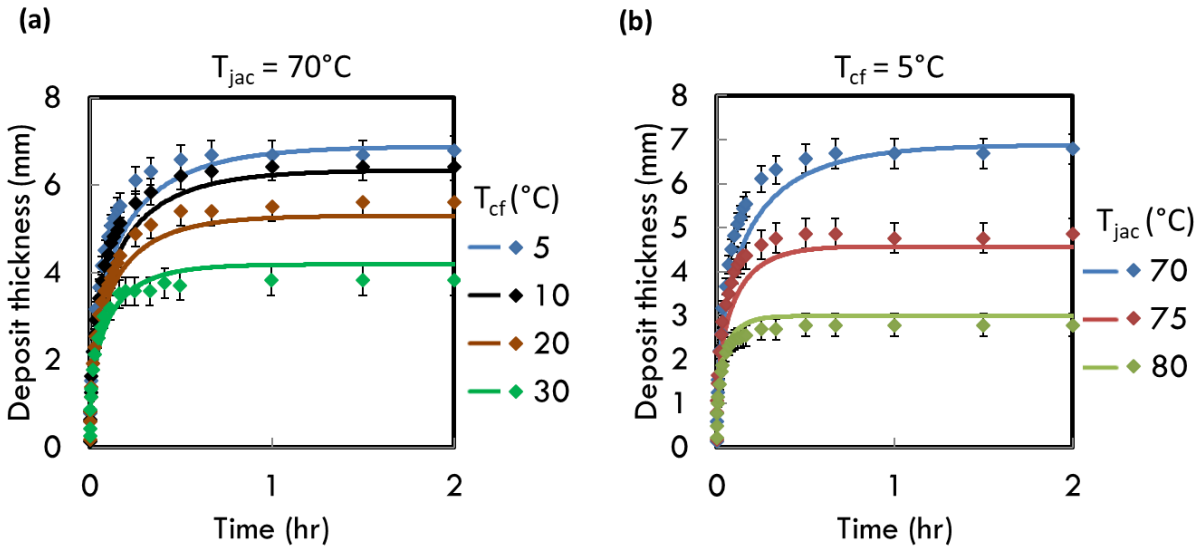

Figure 4-1: Theoretical (curves) vs. experimental (symbols) deposit thickness evolution of pure n-C28 at (a) various T_{cf} at fixed T_{jac} = 70°C, and (b) various T_{jac} at fixed T_{cf} = 5°C.

Table 4-1: Parameters used in the simulations that generate the curves in Figures 4-1 and 4-2.

Parameter						
T_{jac} (°C)	70	70	70	70	75	80
T_{cf} (°C)	5	10	20	30	5	5
$T_{jac,m}$ (°C)	67.5	67.5	67.5	67.5	72	78
$T_{cf,m}$ (°C)	5.8	10.7	20	30	5.8	5.8

ρ (kg/m^3)	800
c_p (J/kg/°C)	2370
ΔH (J/kg)	253,000
k (W/m/°C)	0.16
h_{jac} (W/m^2/°C)	100
h_i (W/m^2/°C)	150
A_{jac} (m^2)	0.0176
r_{cf} (m)	0.005

There is excellent agreement between the theory and the experiments. The theoretical and experimental liquid wax temperatures are also compared in Figure 4-2.

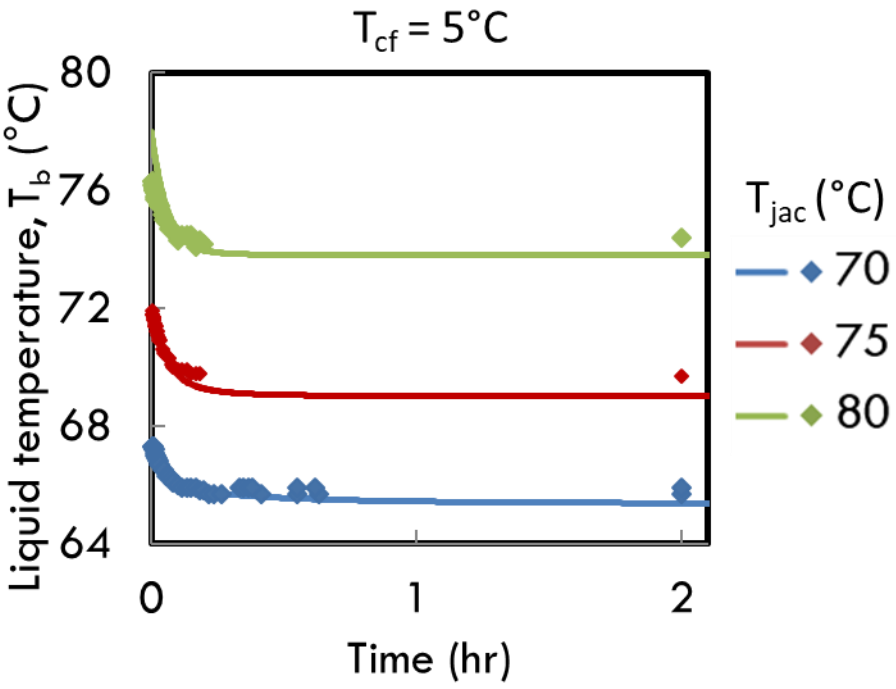

Figure 4-2: Theoretical (curves) vs. experimental (symbols) evolution of pure n-C28 liquid phase temperature, T_b, at various T_{jac} with fixed T_{cf} = 5°C.

The decrease and subsequent plateau of the liquid temperatures are well captured by the model. Based on the success of these predictions, we conclude that the interface temperature is indeed always at the solidification/melting point of n-C28. The results also show that the liquid

phase can be modeled as having a uniform temperature due to adequate mixing despite the complex flow profile inside the cold finger apparatus. Heat transfer coefficients have been shown to be accurate in predicting the heat transfer behavior. The excellent agreement between the theory and the experiments for the single-component pure n-C28 liquid provide assurance that these assumptions can be applied to heat transfer modeling in binary and multicomponent mixtures.

4.3 Pseudo Single Component Deposition Model with No Yield Stress

When the temperature of a wax-containing oil reaches the WAT, the first wax crystals will form. As temperature decreases further, more crystals will form, because wax solubility is lower at lower temperature. For our model, it is assumed that the gel-oil interface temperature is always at the thermodynamic WAT of the oil, i.e. $T_i = WAT(C_b)$, where C_b is the concentration of wax in the oil. This assumption has been used in other models in the literature as well[27,28,30,32,41]. This assumption implies that the first crystals that appear are sufficient to immobilize the mixture and form a gel. In our cold-finger geometry this assumption implies that the yield stress of the mixture exceeds the shear stress imposed by the stirring motion as soon as the first crystals appear. Under this assumption, Equation (4-1) can no longer be applied to calculate deposit growth rate because precipitation only occurs behind the gel-oil interface and not at the interface. Instead, the following equation is applied:

$$\left.\frac{DT}{Dt}\right|_i = 0 \qquad (4\text{-}5)$$

where $\left.\frac{DT}{Dt}\right|_i$ is the material derivative of the temperature at the deposit-oil interface with respect to time. Thus, the deposit boundary is an isotherm corresponding to the wax appearance

temperature of the wax-containing bulk oil, i.e., WAT(C_b). Equation (4-5) simply describes that in the frame of reference that is moving with the interface, the temperature at the interface is assumed to be constant. This constant interface temperature is not just any temperature, but is the Wax Appearance Temperature of the oil, WAT(C_b). The left hand side of Equation (4-5) can be related to the interface velocity, which is also the deposit growth rate, $\frac{d\delta}{dt}$:

$$\left.\frac{\partial T}{\partial t}\right|_i + \left.\frac{\partial T}{\partial r}\right|_i \frac{d\delta}{dt} = 0 \tag{4-6}$$

where $\left.\frac{\partial T}{\partial t}\right|_i$ is the rate of change of the temperature at the interface (°C/s),

and $\left.\frac{\partial T}{\partial r}\right|_i$ is the temperature gradient at the interface (°C/m).

Equation (4-6) can be rearranged to solve for $\frac{d\delta}{dt}$ as a function of the other derivatives:

$$\frac{d\delta}{dt} = -\frac{\left.\frac{\partial T}{\partial t}\right|_i}{\left.\frac{\partial T}{\partial r}\right|_i} \tag{4-7}$$

Equation (4-7) is used to calculate the rate of growth of the deposit.

To resolve the temperature profile in the deposit formed from the binary mixture of n-C28 and n-C12, Equation (4-2) needs to include an additional term to account for latent heat generated due to precipitation behind the deposit front, leading to Equation (4-8):

$$\rho c_p \frac{\partial T}{\partial t} = k \frac{1}{r} \frac{\partial}{\partial r}\left(r \frac{\partial T}{\partial r}\right) + \Delta H \frac{\partial C_p}{\partial t} \tag{4-8}$$

where ΔH is the specific latent heat of crystallization (J/kg),

and C_p is the concentration of precipitated waxes (kg/m^3).

The boundary conditions applied to Equation (4-8) are:

$$\begin{cases} T = T_{cf,m} \text{ at } r = r_{cf} \\ \left. k \frac{\partial T}{\partial r}\right|_i = h_i (T_b - T_i) \text{ at } r = r_{cf} + \delta \end{cases} \tag{4-9}$$

To capture the change in the oil temperature with time, Equation (4-4) is solved as well.

Mass transfer must be considered to account for the compositional changes in n-C12 and n-C28. To describe the mass transfer process, it is assumed that there are three components: n-C28 in the dissolved form (soluble), precipitated n-C28, and the solvent molecules of n-C12, whose concentrations are denoted as C_s, C_p, and C_{solv} respectively. A comprehensive mass balance for the soluble n-C28 in the deposit is shown below:

$$\frac{\partial C_s}{\partial t} = \frac{1}{r}\frac{\partial}{\partial r}\left(D_{eff} r \frac{\partial C_s}{\partial r}\right) - k_r\left(C_s - C_{s,eq}(T)\right) \quad (4\text{-}10)$$

where D_{eff} is the effective diffusivity of soluble n-C28 (m2/s),

k_r is the precipitation rate constant (s^{-1}),

and $C_{s,eq}$ (T) is the solubility limit of soluble n-C28 at temperature T (kg/m3).

The first term on the right side of Equation (4-10) describes the diffusion of soluble n-C28 through the porous deposit, while the second term on the right side describes the rate of precipitation. One can also construct the following mass balance for the precipitated n-C28:

$$\frac{\partial C_p}{\partial t} = k_r\left(C_s - C_{s,eq}(T)\right) \quad (4\text{-}11)$$

Equation (4-11) assumes that precipitated n-C28 cannot diffuse, but can only be generated from the precipitation of soluble n-C28. Here, it is assumed that the precipitation of n-C28 is infinitely fast (i.e. $k_r \rightarrow \infty$), so that Equation (4-10) simplifies to:

$$C_s = C_{s,eq}(T) \quad (4\text{-}12)$$

Equation (4-12) implies that any location, the soluble n-C28 concentration is always at its solubility limit.

The precipitated n-C28 concentration, i.e., the C_p profile, can be obtained from a mass balance on total wax, Equation (4-13) below:

$$\frac{\partial C_s}{\partial t} + \frac{\partial C_p}{\partial t} = \frac{1}{r}\frac{\partial}{\partial r}\left(D_{eff} r \frac{\partial C_s}{\partial r}\right) \quad (4\text{-}13)$$

Equation (4-13) is derived by simply adding together Equations (4-10) and (4-11). We solve Equation (4-13) instead of Equation (4-11) to get precipitated n-C28 concentration, C_p, because we have taken the limit $k_r \to \infty$, and $C_s - C_{s,eq}(T) \to 0$.

Similar to the temperature profile in the oil phase, the n-C28 concentration in the liquid, C_b is also assumed to be uniform, corresponding to well-mixed liquid. Additionally, any mass transfer limitation at the interface between the liquid and the deposit is neglected. Consequently, a simple overall n-C28 mass balance can be used to calculate C_b at any time:

$$m_{total\,C28} = C_b V_{liquid} + 2\pi L_{cf} \int_{r_{cf}}^{r_{cf}+\delta} (C_s + C_p) r\, dr \quad (4\text{-}14)$$

where $m_{total\,C28}$ is the total mass of n-C28 present in the system (kg),

V_{liquid} is the volume of oil in the reservoir (m^3),

L_{cf} is the length of the deposit along the cold finger axis (m),

C_s is the soluble n-C28 concentration at a radial location r in the deposit (kg/m^3),

and C_p is the precipitated n-C28 concentration at a radial location r in the deposit (kg/m^3).

In the deposit, the interlocking network of solid wax crystals forms a porous medium. As a result, molecules take a tortuous diffusion pathway, thus decreasing the diffusivity of the molecules relative to that in precipitate-free oil. In single-phase liquid n-alkane mixtures, the diffusivity of soluble wax has been successfully described by the Hayduk-Minhas equation[44]:

$$D_{w/o}(T) = 13.3(10^{-12})(T + 273.15)^{1.47} \mu(T)^{\left(\frac{10.2}{V_A} - 0.791\right)} V_A^{-0.71} \quad (4\text{-}15)$$

where $D_{w/o}(T)$ is the diffusivity of soluble n-C28 in a single phase n-alkane mixture (m_2/s), $\mu(T)$ is the oil viscosity in the absence of any solid (mPa s), and V_A is the molar volume of n-C28 (cm^3/mol). V_A is assumed to be 507 cm3/mol. Under the experimental conditions, the value

of $D_{w/o}$ calculated using Equation 4-15 typically lies between 10^{-10} and 10^{-9} m^2/s, consistent with $D^{w/o}$ measurements made by Hayduk and Minhas[44].

The oil viscosity in the absence of any solid, $\mu(T)$, is defined in terms of an Arrhenius function, as shown in Equation 4-16 below. Equation 4-16 was obtained by fitting the Arrhenius function to the values of n-C12 viscosity at various temperatures measured via rheometry.

$$\mu(T) = 1.6\left(10^{-2}\right)\exp\left(\frac{1334}{T+273.15}\right) \tag{4-16}$$

In the deposit, the effective diffusivity, D_{eff}, is less well studied, and for it we use an empirical correlation[45]:

$$D_{eff}(T, C_p) = \frac{D_{w/o}\,(T)}{1+\frac{\alpha^2\left(\frac{C_p}{\rho}\right)^2}{1-\frac{C_p}{\rho}}} \tag{4-17}$$

where α is a dimensionless parameter identified as the wax crystal aspect ratio, and ρ is the density of the deposit (kg/m^3). The term $\frac{C_p}{\rho}$ is also known as the solid volume fraction.

4.4 Theoretical (No Yield Stress) vs. Experimental Deposit Thickness – Binary n-C28/nC12 Deposition

The deposition evolutions in Figures 3-4 and 3-5 are now predicted by the model discussed in Section 4.3 with results given in Figure 4-3. The parameters used in these simulations are listed in Table 4-2. Figure 16a shows that, while the model slightly overpredicts the deposit thickness during the initial growth at t < 1 hr, it captures the trends. The assumption that the interface is always at the WAT of the oil appears to be responsible for the overprediction. The interface temperature is likely to lie below the WAT of the bulk oil.

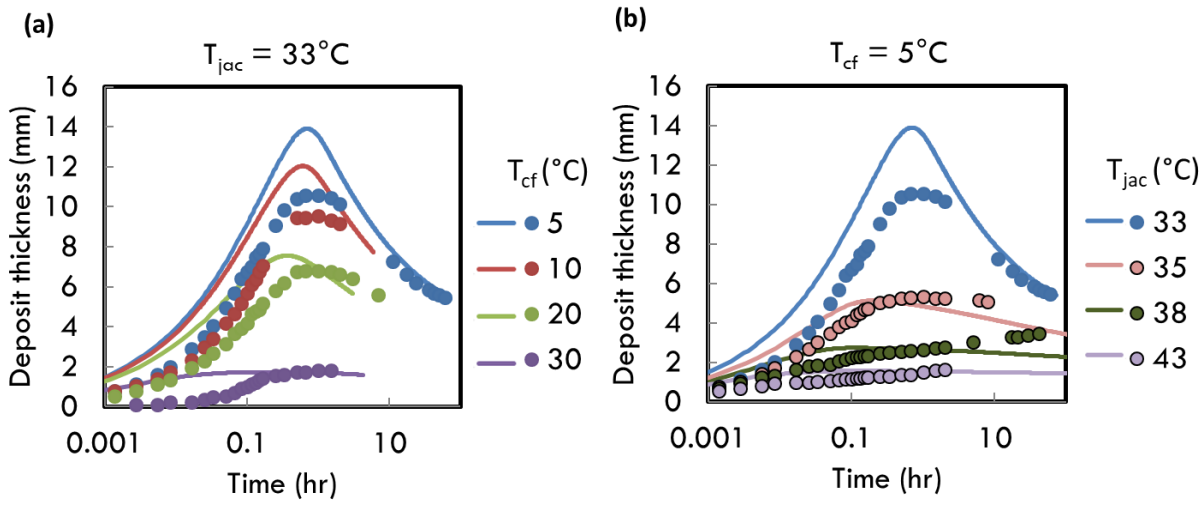

Figure 4-3: Theoretical (curves) vs. experimental (symbols) deposit thickness trajectories at (a) various T_{cf} with fixed T_{jac} = 33°C, and (b) various T_{jac} with fixed T_{cf} = 5°C. The starting mixture contains 10wt% n-C28 and 90wt% n-C12.

Table 4-2: Parameters used in the simulations that generate the curves in Figures 4-3 and 4-4.

Parameter							
T_{jac} (°C)	33	33	33	33	35	38	43
T_{cf} (°C)	5	10	20	30	5	5	5
$T_{jac,m}$ (°C)	33	33	33	33	35	38	43
$T_{cf,m}$ (°C)	5.8	10.7	20	30	5.8	5.8	5.8
ρ (kg/m^3)	790						
c_p (J/kg/°C)	2100						
ΔH (J/kg)	253,000						
k (W/m/°C)	0.16						
h_{jac} (W/m^2/°C)	250						
h_i (W/m^2/°C)	250						
A_{jac} (m^2)	0.0176						
r_{cf} (m)	0.005						
$m_{total\ C28}$ (kg)	0.018						
L (m)	0.06						
α	10						

The transition to a decrease in deposit thickness at later times is captured by the model in Figure 4-3 by taking into account the decreasing oil WAT. The WAT of the bulk oil decreases over time due to depletion of wax which is caused by the molecular diffusion in the deposit that continuously takes away wax from the reservoir. As the WAT in the oil phase decreases, the precipitated wax near the interface dissolves to maintain the equilibrium soluble wax concentration at the temperature of the interface. This event causes the interface to retreat back to a location whose temperature matches the reduced WAT of the bulk oil. This process can continue so long as waxes can diffuse into the deposit and as long as the bulk oil continues to decrease in wax content. The rate at which the deposit recedes therefore depends strongly on the rate of diffusion inside the deposit. In the model predictions, the parameter α in Equation (4-17) has been set to 10 to give the trajectories shown by the curves in Figure 4-3. This value of α is within the range found in the literature[5,6]. Eventually, at very long time, the deposit would become almost 100% precipitated wax, which would inhibit further diffusion of soluble wax into the deposit, and the retreat of the interface would then cease. This process is likely an important mechanism for the densification and hardening of waxy deposits in pipelines, making wax removal more difficult as densification progresses.

The deposition thickness trajectories in Figures 3-6 and 3-7 are now predicted by the model in Section 4.3, and the results are shown in Figure 4-4. Recall that the effective diffusivity of wax in the deposit significantly affects the rate of increase in the deposit total wax content. The one unknown parameter in the effective diffusivity correlation used in Equation (4-17) is α, which is assigned the value of 10 to generate the curves shown in Figures 4-3 and 4-4.

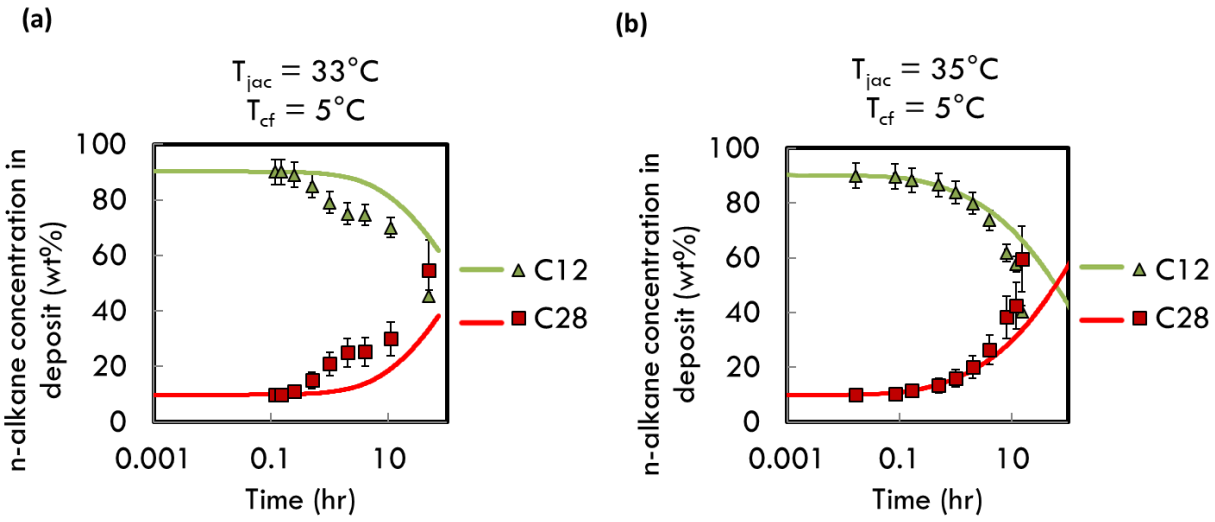

Figure 4-4: Theoretical (curves) vs. experimental (symbols) concentrations of n-C28 and n-C12 in the deposit at (a) T_{jac} = 33°C and T_{cf} = 5°C, and (b) T_{jac} = 35°C and T_{cf} = 5°C.

As can be seen from the comparison between the model predictions and the experimental measurements presented in Figure 4-3, the model generally overpredicts the deposition thickness of the binary system 10wt% n-C28 and 90wt% n-C12. It is suggested that the reason for this overprediction is that the interface temperature is below the WAT. This section discusses this concept further.

To demonstrate mathematically that lowering the interface temperature can solve the discrepancy between the model and the experimental deposit thickness, simulations were performed using the model, but with the interface temperature set to 1°C, 2.5°C, or 5°C lower than the WAT. The results of these simulations are shown in Figure 4-5.

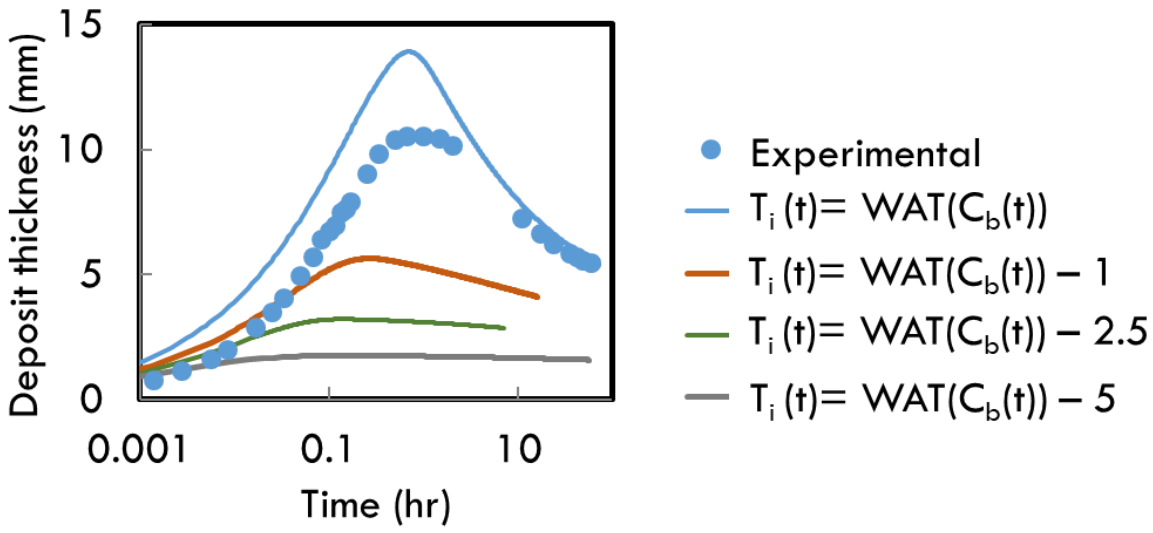

Figure 4-5: Simulations (colored curves) performed using the model presented in Section 4.3, except with the interface temperature modified.

As the interface temperature T_i decreases, so does the deposit thickness at any given time. This numerical exercise demonstrates that the interface temperature does lie below the WAT. Notice that the thicker the deposit, the more sensitive the deposit thickness is to the interface temperature, i.e. there is a dramatic change in thickness going from T_i = WAT to T_i =(WAT – 1), but the change in thickness is less dramatic going from T_i = (WAT – 1) to T_i = (WAT – 2.5) despite the larger change in T_i. This non-linear relationship between T_i and deposit thickness is credited to the cylindrical geometry of the system.

The physical explanation that an interface temperature can become lower than the thermodynamic WAT is traced back to the non-Newtonian characteristics of waxy oil mixtures. Assuming the interface temperature lies at the WAT implies that a waxy oil mixture behaves as a solid as soon as the "first crystals" appear at the WAT. In reality, waxy oil mixtures gradually changes from behaving as a Newtonian fluid (T>WAT) to a semi solid with viscoelastic and viscoplastic properties (T<WAT) to a complete solid (T<Gelation Temperature) as temperature decreases (or as wax crystal concentration increases). Gelation temperature here alludes to the

temperature at which the oil stops flowing due to the presence of a sufficient amount of wax crystals.

While the assumption that T_i = WAT in our model may be an extreme one, it can still reasonably explain the experimentally measured deposition thickness. This is likely because the gelation temperature of the binary n-alkane system of 10wt% n-C28 and 90wt% n-C12 is be close to its WAT under the conditions tested here. Such a high gelation temperature may be attributed to two factors. One is that n-C28 crystals in the binary mixture are on average larger, and thus stronger, than wax crystals formed from a polydispersed mixture made up of thousands of different molecules. The second factor is that the shear stress generated by the flow in this cold finger apparatus is not sufficiently strong to overcome the structural rigidity of the n-C28 crystals. Both factors contribute to the situation where the yield stress is greater than the shear stress imposed on the mixture.

In the situation where the oil yield stress is greater than the imposed shear stress, the rate-limiting step to the deposit growth is the transient heat transfer. Such a process may also be called a gelation process. A model from previous studies[14,15] also proposes a gelation process, but one that requires wax crystals enrichment in the vicinity of the deposition front before gelation can occur. According to this model, an oil that cannot gel in its original composition may still form a deposit eventually because wax crystals can accumulate in the vicinity of the deposition front due to molecular diffusion of soluble waxes to this location. In this situation, the deposit growth is slow and its rate is dictated by the molecular diffusion of soluble waxes. In the current study however, gelation can occur, at least initially, without any need for wax enrichment (recall that the composition of the deposit remains almost identical to that of the oil at very early times).

4.5 Pseudo Single Component Deposition Model with Yield Stress

Our model assumes the existence of thin heat transfer and mass transfer boundary layers at the deposit-oil interface across which temperature and wax concentration jump from uniform values in the stirred oil to surface values at the leading edge of the deposit. Our measurements of temperature and wax concentration far from the inner and outer surfaces of the stirred oil are in agreement with this assumption. This behavior is expected due to mixing induced by the agitation of the magnetic stir bar.

Across the heat and mass transfer boundary layers, the temperature and wax concentration change abruptly from the oil side to the deposit side. The steep temperature and wax concentration profiles inside the boundary layer are not resolved in our model. Instead, we compute the overall energy and mass exchanged at this interface and assume there is no accumulation of energy nor mass within that layer[46]. As shown in Figure 4-6, a thin control volume that encases the boundary layer is taken to be moving with front of the deposit towards the right at a speed $\frac{d\delta}{dt}$, where δ is the deposit thickness and t is time. Any energy or mass that enters this control volume through the oil side (right) leaves the control volume through the deposit side (left), and vice versa. Next, the mass and energy balances across this thin volume will be derived.

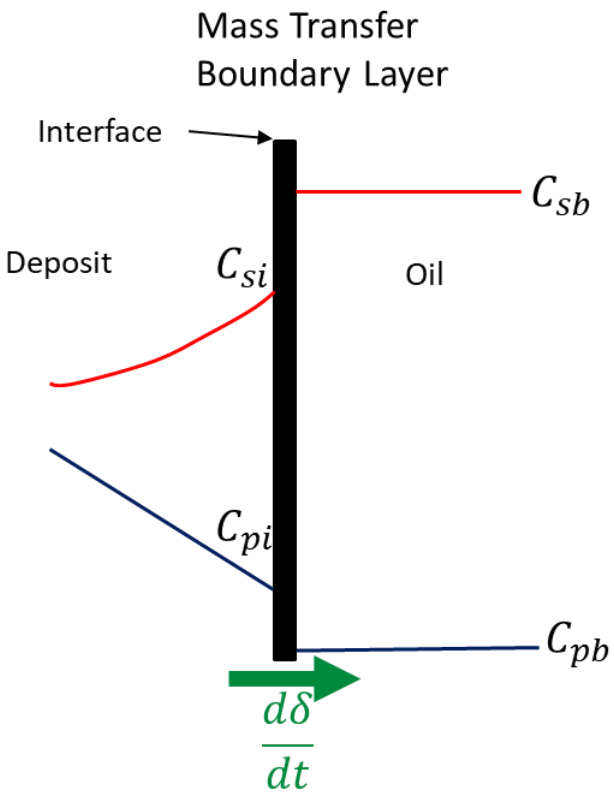

Figure 4-6: The mass transfer boundary layer. The thin "black box" signifies that the dissolved wax and solid wax concentration profiles within the boundary layer are not resolved.

Across this mass transfer boundary layer the dissolved, or soluble, wax concentration C_s jumps from that in the bulk oil, C_{sb}, which is to the right of the control volume, to the dissolved wax concentration just behind (i.e., to the left of) the interface, C_{si}. The flux of wax is given by the product of the difference of these concentrations, i.e. the driving force, times the mass transfer coefficient k_c. On the left side there is a flux of dissolved wax diffusing further into the deposit according to Fick's Law. As the control volume moves into the oil domain, it sweeps in mass from the right, and leaves behind mass on its left side. As a result, there is a mass flux on the right side of the interface equal to $C_{sb}\frac{d\delta}{dt}$ while on the left hand side it is $\left(C_{pi}+C_{si}\right)\frac{d\delta}{dt}$, where C_{pi} is the solid (or precipitated) wax concentration C_p at the interface. If the oil temperature is below its Wax Appearance Temperature (WAT), there will also be precipitated waxes present in the oil with concentration C_{pb}. In this situation, an additional apparent flux,

$C_{pb}\frac{d\delta}{dt}$ will appear on the right hand side of the moving boundary. In our experiments reported here, the oil temperature is always above WAT, so that C_{pb} is zero. The interfacial wax mass balance can be then summarized as follows:

$$D_{eff}\frac{\partial C_s}{\partial r}+\left(C_{pi}+C_{si}\right)\frac{d\delta}{dt}=k_c(C_{sb}-C_{si})+\left(C_{sb}+C_{pb}\right)\frac{d\delta}{dt} \tag{4-18}$$

where D_{eff} is the effective diffusivity of soluble wax inside the gel/deposit near the interface. A similar equation can be derived for the interfacial energy balance equation, using the same control volume moving at the same speed $\frac{d\delta}{dt}$ as the mass-transfer control volume. The temperatures on left and right side of the interface are shown in Figure 4-7.

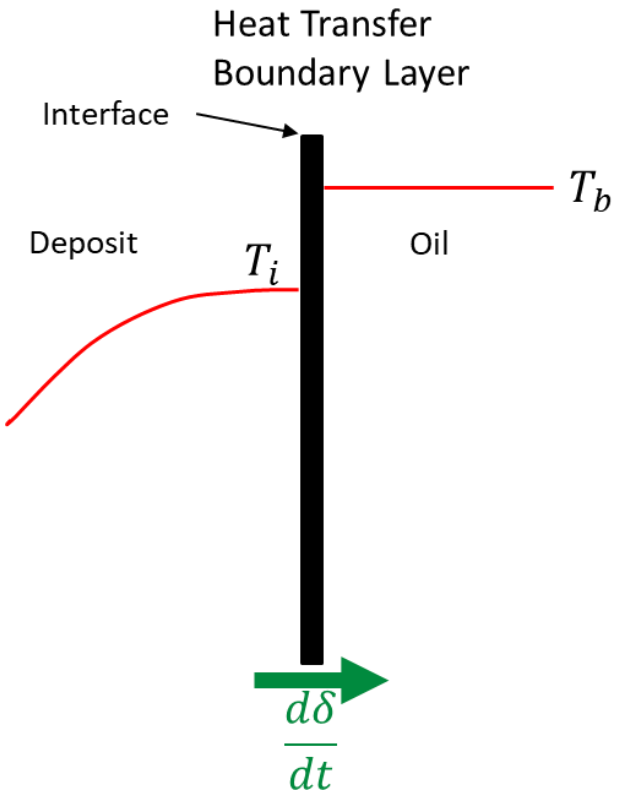

Figure 4-7: The heat transfer boundary layer.

On the right side of the interface, there is a heat transfer boundary layer across which the temperature jumps from the bulk oil temperature, T_b, to the surface temperature, T_i, the

difference being the driving force. On the left side the heat flux into the deposit is given by the Fourier's Law. Similar to the jump in wax concentration across the interface, there should also be a jump in sensible heat content from $\rho\hat{c}_p T_b$ to $\rho\hat{c}_p T_i$, assuming, as is reasonable, that ρ and $\hat{c}_p$ of the oil and of the deposit are very similar. Therefore, an additional term therefore appears on either side of the heat balance equation that takes into account this difference in sensible heat across the interface. Similar terms on either side account for the latent heat ΔH released during the formation of solid waxes. The interfacial energy balance can be summarized as follows:

$$k\frac{\partial T}{\partial r} + \rho\hat{c}_p T_i \frac{d\delta}{dt} - C_{pi}\Delta H\frac{d\delta}{dt} = h_i(T_b - T_i) + \rho\hat{c}_p T_b \frac{d\delta}{dt} - C_{pb}\Delta H\frac{d\delta}{dt} \tag{4-19}$$

where k is the gel/deposit thermal conductivity, and ΔH the specific latent heat of crystallization.

Next, the heat and mass balance equations to be solved in the deposit and oil domains are derived. Because of the uniformity of the deposit along the cold finger axis (see Figure 2-5), energy and mass transfers in the axial and tangential directions can be neglected. The energy balance in the deposit domain is given by the time-dependent, axisymmetric energy balance:

$$\rho\hat{c}_p\frac{\partial T}{\partial t} = k\frac{1}{r}\frac{\partial}{\partial r}\left(r\frac{\partial T}{\partial r}\right) + \Delta H\frac{\partial C_p}{\partial t} \tag{4-20}$$

On the right side of Equation (4-20), the first term represents heat conduction, while the second term represents latent heat release due to precipitation (or latent heat absorption in the case of a dissolution). The second term is present because further precipitation inside a deposit occurs during deposit aging.

The flux boundary conditions necessary to solve Equation (4-20) are:

$$B.C.'s\begin{cases} h_{cf}(T - T_{cf}) = k\dfrac{\partial T}{\partial r} \quad at \quad r = r_{cf} \\ k\dfrac{\partial T}{\partial r} + \rho\hat{c}_p T_i\dfrac{d\delta}{dt} = h_i(T_b - T) + \rho\hat{c}_p T_b\dfrac{d\delta}{dt} + (C_{pi} - C_{pb})\Delta H\dfrac{d\delta}{dt} \quad at \quad r = r_{cf} + \delta \end{cases} \tag{4-21}$$

At the boundary between the cold finger's wall and the inner edge of the deposit ($r = r_{cf,out}$), the temperature drop across the stainless steel tube wall has been neglected in Equation (4-21). This omission is reasonable because the thermal conductivity of stainless steel is two orders of magnitude greater than the thermal conductivity of n-alkanes, and the stainless steel tube wall is quite thin (~ 1 mm), leading to negligible resistance to heat transfer through the wall. At the moving interface ($r = r_{cf,out} + \delta$), Equation (4-19) is used as the boundary condition.

In the stirred solution domain, we assume the temperature to be spatially uniform, which we validated experimentally. The transient energy balance is:

$$\hat{c}_p \frac{d}{dt}\left(m_{liq} T_b\right) = U_{jac} A_{jac}\left(T_{jac} - T_b\right) - h_i A_i (T_b - T) \tag{4-22}$$

where m_{liq} is the mass of stirred solution.

By simultaneously solving Equations (4-20) and (4-22), radial and temporal variations of temperature in the deposit are resolved, as well as the temporal variation in the stirred solution temperature.

For the mass balance equations, it is assumed that all constituents in the mixture can be lumped into one of three categories: dissolved waxes, precipitated waxes and solvent. The mass balance for the dissolved waxes in the deposit is derived in an analogous manner to the energy balance inside the deposit:

$$\frac{\partial C_s}{\partial t} = \frac{1}{r}\frac{\partial}{\partial r}\left(r D_{eff} \frac{\partial C_s}{\partial r}\right) - k_r\left(C_s - C_{s,eq}[T]\right) \tag{4-23}$$

where k_r is the precipitation/dissolution rate constant and $C_{s,eq}$ is the solubility limit of waxes at a given temperature.

The first term on the right hand side describes the diffusion of dissolved wax, while the second term describes the rate by which dissolved waxes precipitate. The precipitation process is

modelled as a reversible first order reaction with driving force given by the difference between the local concentration and the solubility limit. Note that Equation **(4-12**) also accounts for dissolution in situations where the local concentration is below the solubility limit. The relevant boundary conditions are: 1) no penetration at the cold finger outer wall and 2): a flux boundary condition at the deposit-oil interface:

$$B.C.'s \begin{cases} D_{eff}\dfrac{\partial C_s}{\partial r} = 0 \;\; at \;\; r = r_{cf} \\ D_{eff}\dfrac{\partial C_s}{\partial r} + \left(C_{si} + C_{pi}\right)\dfrac{d\delta}{dt} = k_c(C_{sb} - C_{si}) + \left(C_{sb} + C_{pb}\right)\dfrac{d\delta}{dt} \quad at \;\; r = r_{cf} + \delta \end{cases} \tag{4-24}$$

Similar to the temperature, the dissolved wax concentration in the stirred solution is also assumed to be uniform throughout the liquid mixture.

We also need to solve for the mass balance of precipitated waxes in the deposit. It is assumed that precipitated waxes are immobilized when they form in the deposit and do not diffuse. The precipitated waxes are assumed to be a continuum rather than as discrete particles, where their formation (and dissolution) can be described as follows:

$$\frac{\partial C_p}{\partial t} = k_r\left(C_s - C_{s,eq}[T]\right) \tag{4-25}$$

Unfortunately, solving Equation (4-25) can be numerically expensive because when kr is relatively large, a very small time step size is required to ensure stability and convergence of the numerical solution. To avoid this problem, we instead compute the precipitate wax concentration C_p by solving the total wax mass balance, which is derived by simply adding Equation (4-23) to Equation (4-25), yielding

$$\frac{\partial C_p}{\partial t} + \frac{\partial C_s}{\partial t} = \frac{1}{r}\frac{\partial}{\partial r}\left(rD_{eff}\frac{\partial C_s}{\partial r}\right) \tag{4-26}$$

The rate of wax deposition still appears in Equation (4-23) where it can influence the solution to the mass balance.

In the deposit, the precipitated waxes form an interlocking network of solid wax crystals, resulting in a more tortuous pathway for wax molecules in the liquid phase that are diffusing further into the deposit. This increased tortuosity leads to a decrease in the effective diffusivity of the molecules relative to that in a precipitate-free oil. In solid-free oils, the diffusivity of dissolved wax is captured well by the Hayduk-Minhas equation[44]:

$$D_{w/o} = 13.3(10^{-12})(T + 273.15)^{1.47}\mu^{\left(\frac{10.2}{V_A} - 0.791\right)}V_A^{-0.71} \tag{4-27}$$

where μ is the precipitate-free oil viscosity, and V_A is the molar volume of the wax molecule. For our n-C28/n-C12 model oil, we use Equation (4-28) to describe μ, which was obtained by fitting n-C12 experimental viscosities at different temperatures.

$$\mu = 1.6 \times 10^{-2} \exp\left(\frac{1334}{T + 273.15}\right) \tag{4-28}$$

In the deposit, we use an empirical correlation from Cussler[45] to describe the effective diffusivity of wax molecules, D_{eff}, which takes into account the local solid wax content:

$$D_{eff} = \frac{D_{w/o}\,(T)}{1 + \frac{K_\alpha^2 \left(\frac{C_p}{\rho}\right)^2}{1 - \frac{C_p}{\rho}}} \tag{4-29}$$

Here, K_α is a dimensionless parameter identified as the wax crystal aspect ratio, and C_p again is the mass concentration of precipitated wax, so that $\frac{C_p}{\rho}$ is the volume fraction of precipitated solid. D_{eff} varies both spatially and temporally not only because of temperature changes but also because $\frac{C_p}{\rho}$ increases with time during deposit aging, leading to a gradual decrease in D_{eff}. When no precipitated wax is present, D_{eff} is on the order of 10^{-10} m^2/s, but it can decrease by multiple orders of magnitude as $\frac{C_p}{\rho}$ rises.

In the stirred solution, a simple overall wax mass balance can be used to calculate the remaining wax in the stirred solution at any time, t:

$$m_{total\,wax} = (C_{sb} + C_{pb})V_{liquid} + 2\pi L_{cf} \int_{r_{cf}}^{r_{cf}+\delta} (C_s + C_p) r\, dr \tag{4-30}$$

where $m_{total\ wax}$ is the total mass of wax present in the system, i.e. deposit + solution, V_{liquid} the volume of oil in the reservoir, and L_{cf} the length of the deposit along the cold finger axis. V_{liquid} also equals $\pi r_{jac}^2 L_l - \pi\left(r_{cf,outer} + \delta\right)^2 L_{cf}$, where r_{jac} and L_l are the jacketed beaker radius and height of the liquid in the beaker respectively.

At this point we have derived all the energy and mass balances necessary for both domains. What remains is to derive the equations describing how the deposit-oil interface evolves with time in order to solve for its rate of growth $\frac{d\delta}{dt}$. At the interface, the solid wax concentration is taken to be at C_{pi} due to the assumption that C_{pi} is the solid wax concentration required to resist erosion under the flow-induced stress at the interface. In mathematical terms, this implies that the substantial derivative of C_p at the interface is zero at all times:

$$\left.\frac{\partial C_p}{\partial t}\right|_{i^-} + \frac{d\delta}{dt}\left.\frac{\partial C_p}{\partial r}\right|_{i^-} = 0 \tag{4-31}$$

where the subscript i^- indicates that the derivatives are evaluated at the interface on the deposit side. Equation (4-31) can be rearranged to express the deposit growth rate $\frac{d\delta}{dt}$ in terms of the partial derivatives:

$$\frac{d\delta}{dt} = -\frac{\left.\frac{\partial C_p}{\partial t}\right|_{i^-}}{\left.\frac{\partial C_p}{\partial r}\right|_{i^-}} \tag{4-32}$$

The finite difference method (FDM) is used to solve the system of partial differential equations. The model uses the central difference scheme for space discretization and the backward Euler scheme for integrating with respect to time[47,48]. The deposit domain is discretized into 50 nodes. The oil domain is not discretized because of the uniformity in temperature and wax concentration (due to agitation). The algorithm used to solve the deposition model described is presented in Figure 4-8.

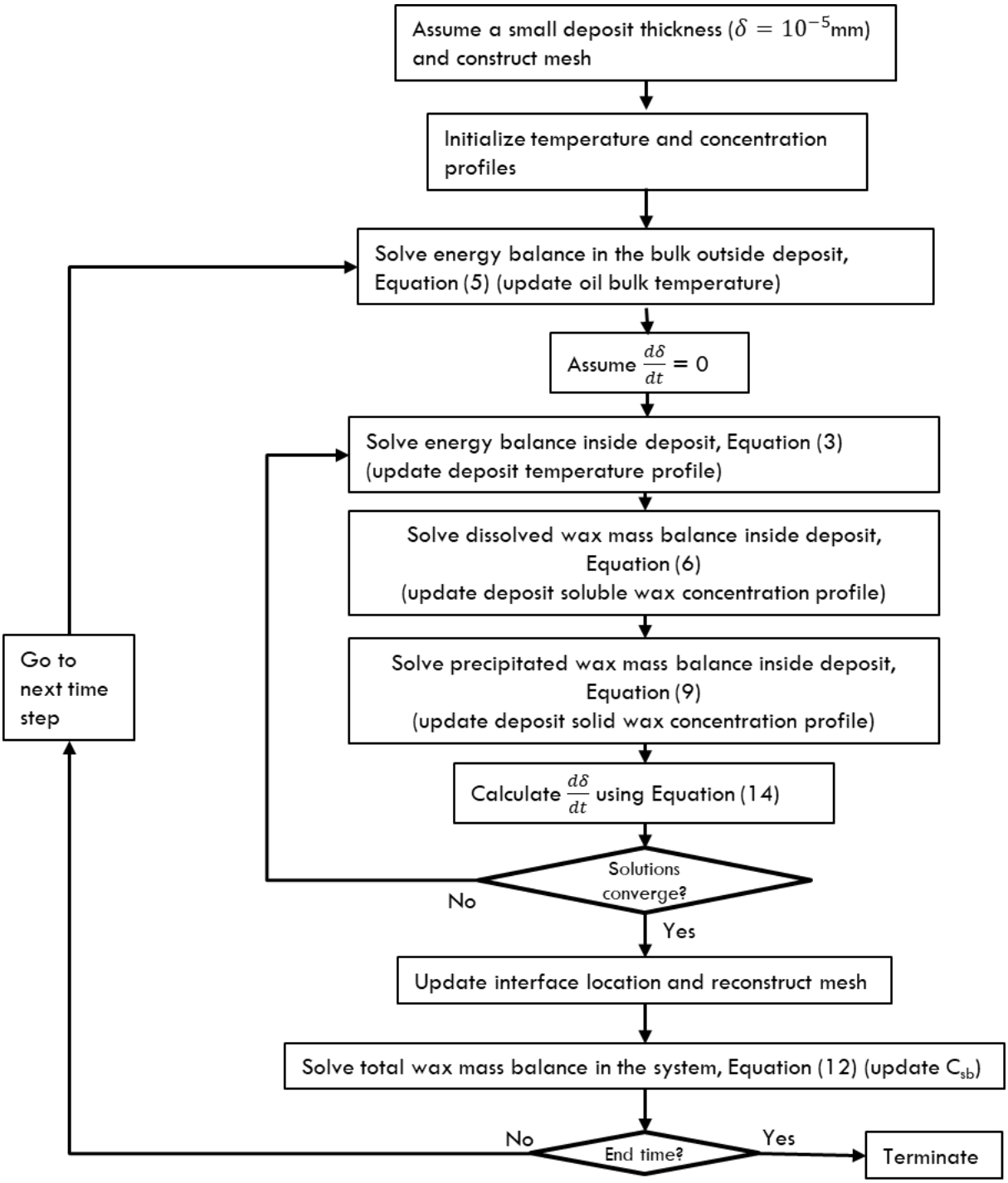

Figure 4-8: Cold Finger wax deposition model algorithm.

The deposition characteristics, such as deposition rate, deposit thickness and deposit composition will now be examined in different limits of key parameters. For all of the simulations in this section, a mixture of 10wt% n-C28 and 90wt% n-C12 was used as the fluid.

The physical properties and solubility curve of this mixture were taken as model parameters. To keep our illustrative calculations simple and easily explained, for these example calculations we set the radius of the jacketed beaker, r_{jac} containing the oil to 100m (i.e. very large) to prevent depletion of wax in the oil and to ensure that the oil temperature, T_b stays at the jacketed beaker set point temperature, T_{jac}. In our earlier work[49] on heat-transfer-controlled deposition, we used an experimental value of the jacket radius, which led to non-monotonic growth of the deposit thickness due to depletion of wax in the finite oil bath, which we avoid in these calculations by assuming a large jacket radius. The oil was assumed to be composed of 10wt% n-C28 and 90wt% n-C12. T_{jac} was set to 35°C, 3°C higher than the WAT of the oil; hence the precipitated wax concentration in the oil, C_{pb}, is zero. Other fixed parameters are presented in Table 4-3. All parameters with the exception of the jacket radius are close to the actual values taken from experiments. Later, when we compare predictions against the experimental data, we will set the jacket radius equal to its experimental value.

Table 4-3: Set of fixed parameters used in model calculations.

Parameter	
T_{jac} (°C)	35
$T_{cw,avg}$ (°C)	5
$r_{cf,outer}$ (m)	0.005
r_{jac} (m)	100
L_l (m)	0.07
L_{cf} (m)	0.06
ρ (kg/m^3)	800
$\hat{c}_p$ (J/kg/°C)	2100
ΔH (J/kg)	200,000
k (W/m/°C)	0.16
U_{jac} (W/m^2/°C)	250
h_i (W/m^2/°C)	250
h_{cf} (W/m^2/°C)	20000
V_A (cm^3/mol)	507
K_α	10
C_{sb}(kg/m^3), t = 0	80 (10wt%)
C_{pb}(kg/m^3)	0

The effects of the following parameters on deposit thickness and deposit growth rate are now examined:

1) the external mass transfer coefficient, k_c
2) the critical solid wax concentration at the interface, C_{pi}
3) the first-order precipitation rate constant, k_r

Efficient mixing induced by the rotating magnetic stir bar ensures that the wax concentration outside the deposit is uniform except for a thin layer very close to the deposit-oil interface. It is in this thin layer, also known as the mass transfer boundary layer, that the resistance to mass transfer is highest. While here we take the boundary layer to be of infinitesimal thickness, the thickness of the experimental boundary layer inversely correlates with the value of k_c; the thinner the boundary layer, the greater the magnitude of k_c. With increasing agitation rate, the boundary layer becomes thinner, and k_c correspondingly increases. A higher k_c translates into a faster rate of mass transfer of dissolved waxes to the deposit-oil interface. Figure 4-9 shows how the deposit thickness evolves with time under different time-independent k_c values. In all of these cases, k_r and C_{pi} were set to 10 s^{-1} and 10 kg/m^3 (1.25 wt%) respectively.

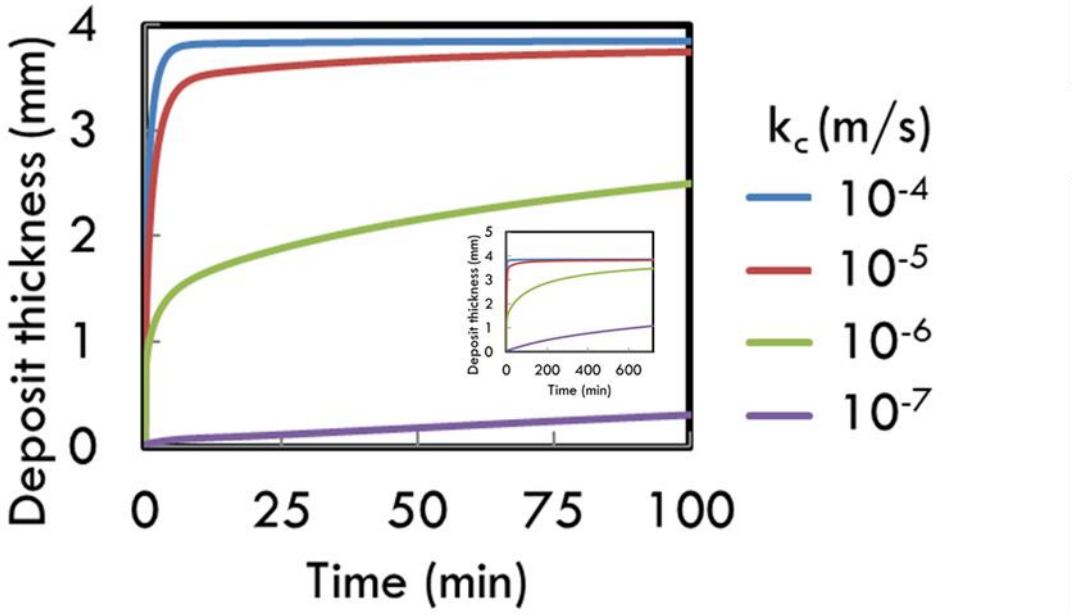

Figure 4-9: Time evolution of deposit thickness for different values of k_c, keeping $k_r = 1s^{-1}$, $C_{pi} = 10$ kg/m^3. The inset shows that the $k_c = 10^{-6}$ m/s trajectory approaches the plateau thickness of 3.8mm after 700 minutes.

Increasing k_c allows for a deposit to grow more rapidly due to higher rate of transport of dissolved waxes to the interface. As the interface moves away from the cold finger, the longer path for heat transfer into the cold finger causes the interface temperature to rise. Regardless of the value of k_c, the deposit growth eventually stops at the same deposit thickness, namely the thickness at which the interface temperature, T_i, has risen to the wax appearance temperature (WAT). The temperature profile is identical for all these example cases because heat transfer properties (thermal conductivity and heat transfer coefficients) are all fixed; thus the deposit always ceases its growth upon reaching the same deposit thickness.

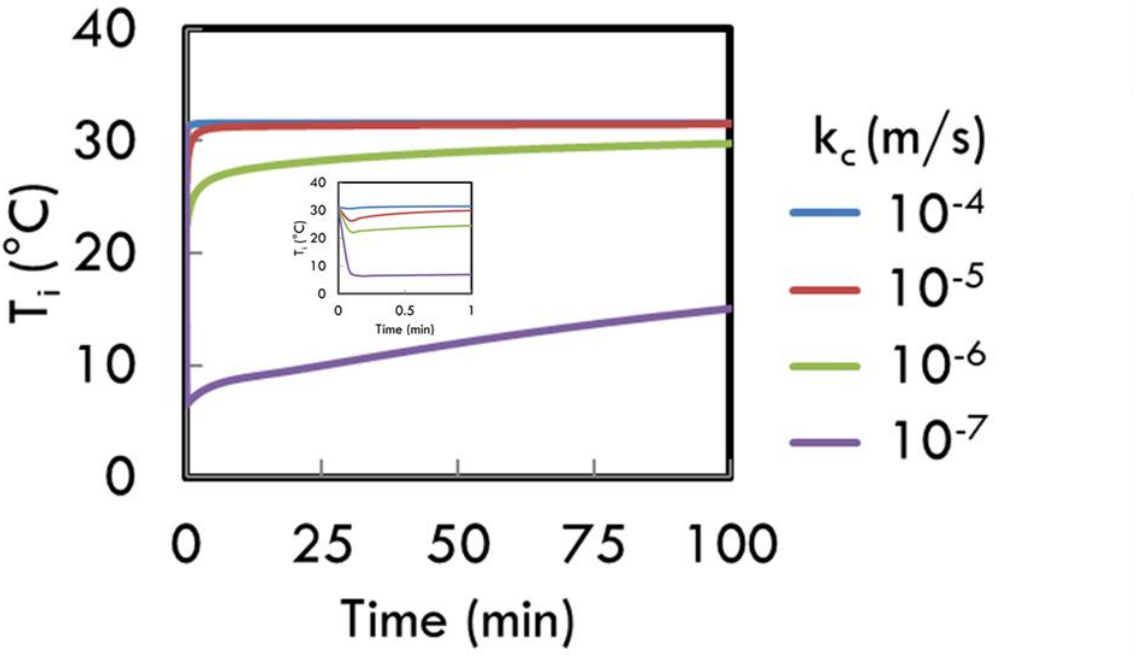

Figure 4-10: Time evolution of the temperature at the deposit-oil interface, T_i, for different values of k_c, keeping $k_r = 10s^{-1}$, $C_{pi} = 10$ kg/m^3. The insert shows the response at early times.

Figure 4-9 shows that increasing k_c from 10^{-6} to 10^{-5} m/s doubles the deposit thickness attained within 25 minutes, but increasing k_c from 10^{-5} to 10^{-4} m/s only increases deposit thickness by less than 3% over this time period. Furthermore, increasing k_c beyond 10^{-4} m/s does not yield a further increase in growth rate. This saturation in the effect of k_c implies that the rate of transport of dissolved waxes from the oil to the deposit-oil interface has ceased to be the limiting factor for the deposit growth rate and the heat transfer rate is now the limiting factor. To demonstrate this transition, Figure 4-10 shows how the interface temperature, T_i evolves with time for all these same cases. Notice T_i remains constant at the WAT when k_c is greater than 10^{-5} m/s even though **Error! Reference source not found.** shows that the deposit is still growing when t < 30 minutes. This behavior implies that the deposit-oil interface only advances as fast as sufficient heat is removed from the incoming wax to drop its temperature to the WAT, indicating that heat transfer has become the limiting factor for growth. Another interesting behavior for k_c =

10^{-6} m/s is the very sharp drop in T_i from WAT to around 23°C at time near zero, as shown by the green curve in Figure 4-10. This rapid drop occurs as the deposit thickness increases rapidly to around 1mm, as shown in Figure 4-9. This occurs because for thin deposits, the concentration gradient of soluble wax in the deposit is very steep, and hence the diffusion of soluble wax inward from the front towards the cold finger is faster than can be replaced by mass transfer from the bulk oil, leading to a drop in soluble wax concentration at the front as can be seen in Figure 4-11. A lower temperature there is then required to precipitate wax at the front. This occurs because when the deposit is still thin, the mass transfer Biot number, or ratio of mass transfer resistance in the deposit to that outside of it, is small. As the deposit thickens, the mass transfer Biot number gradually becomes larger, and so the soluble wax concentration at the front gradually grows towards that in the bulk solution as shown in Figure 4-11, and so the temperature of the front gradually increases towards the WAT, allowing the front to move further away from the cold finger, into warmer fluid while still allowing soluble wax to precipitate due to its higher concentration. For $k_c = 10^{-6}$ and 10^{-7} m/s, the growth rate is so slow that the heat transfer rate virtually becomes pseudo-steady-state as can be seen with the slowly increasing T_i towards WAT as the front advances outward.

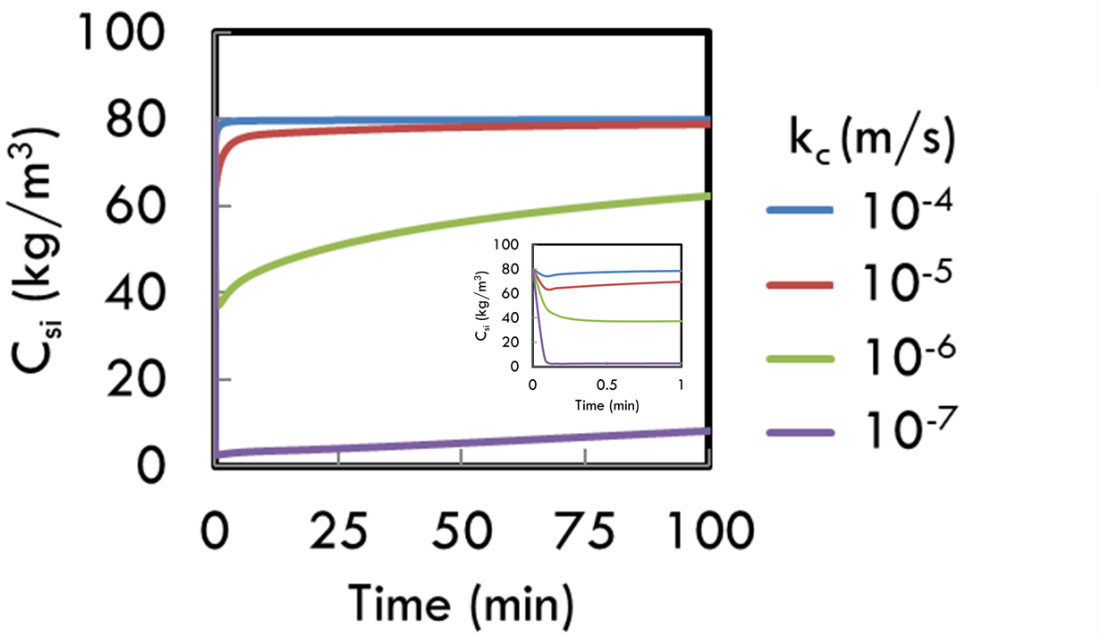

Figure 4-11: Time evolution of the dissolved wax concentration at the deposit-oil interface, C_{si} for different values of k_c, keeping $k_r = 10s^{-1}$, $C_{pi} = 10$ kg/m^3. The insert shows the early time behavior.

Similar to the interface temperature T_i, the interface dissolved wax concentration C_{si} for $k_c = 10^{-4}$ m/s remains constant even when the deposit-oil interface is advancing. This nearly constant C_{si} is equal to the oil bulk concentration, C_{sb}, proving that the mass transfer through the boundary layer to the deposit-oil interface is faster than mass diffusion into the deposit and not limiting the growth of the deposit thickness, which is instead controlled by the heat transfer rate needed to cool the growing deposit and remove the latent heat necessary to allow precipitation. The time dependence of C_{si} for $k_c = 10^{-6}$ and 10^{-7} m/s indicates, on the other hand, that external mass transfer controls the deposit growth. An initial rapid drop in temperature T_i and soluble wax concentration C_{si} at the front is then due to the very low initial mass transfer Biot number, whose gradual rise with increasing deposit thickness allows gradual recovery of T_i towards WAT and C_{si} towards the bulk value in solution.

C_{pi} corresponds to the concentration of wax crystals needed to immobilize the liquid phase. The higher the value of C_{pi}, the higher the concentration of precipitated wax crystals at the interface. For a given flux of dissolved waxes reaching the interface, a higher C_{pi} would result in the formation of a thinner and more compact depositing layer, leading to a slower growth rate of the deposit. This behavior can be shown in Figure 4-12, where C_{pi} is varied while holding k_c and k_r at 10^{-5} m/s and 10 s^{-1} respectively. Note that in the previous figures, C_{pi} was set to 10 kg/m^3, which is low enough that it has only a minor effect on deposit thickness growth.

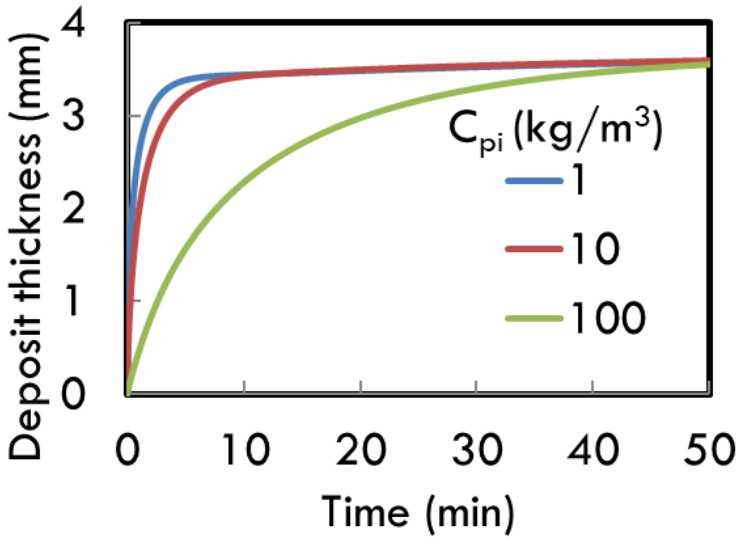

Figure 4-12: Time evolution of deposit thickness for different values of C_{pi}, keeping $k_c = 10^{-5}$ m/s, $k_r = 10s^{-1}$.

The parameter C_{pi} is a measure of the concentration of precipitated wax needed to produce a yield stress equal to the shear stress imposed at the interface by the flow. The higher the shear stress in the solution, the higher the corresponding C_{pi}. The results in Figure 4-12 are consistent with previous experimental literature, where it was found that increasing flow rate (which leads to a higher shear stress at the wall and thus a higher C_{pi}) results in a thinner deposit at a given time and a deposit that is more enriched in wax crystals.[6,13,34,50]

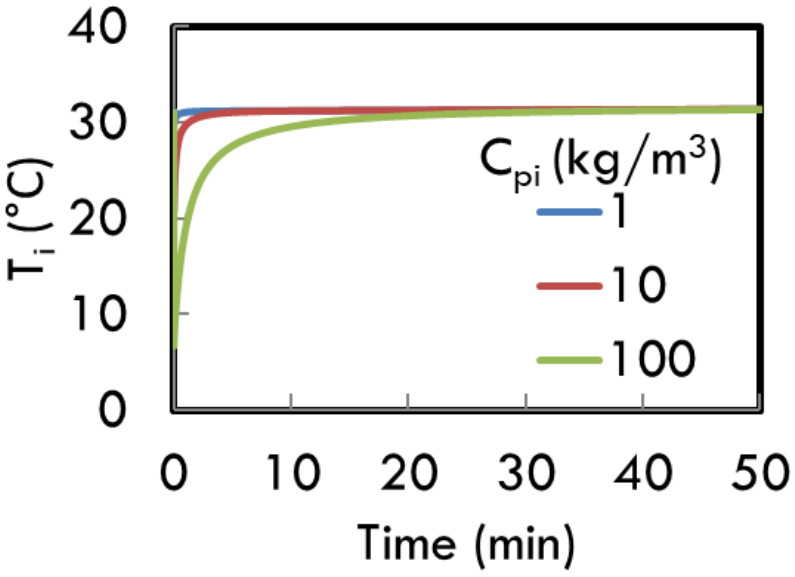

Figure 4-13: Time evolution of the temperature at the deposit-oil interface, T_i for different values of C_{pi}, keeping $k_c = 10^{-5}$ m/s, $k_r = 10s^{-1}$.

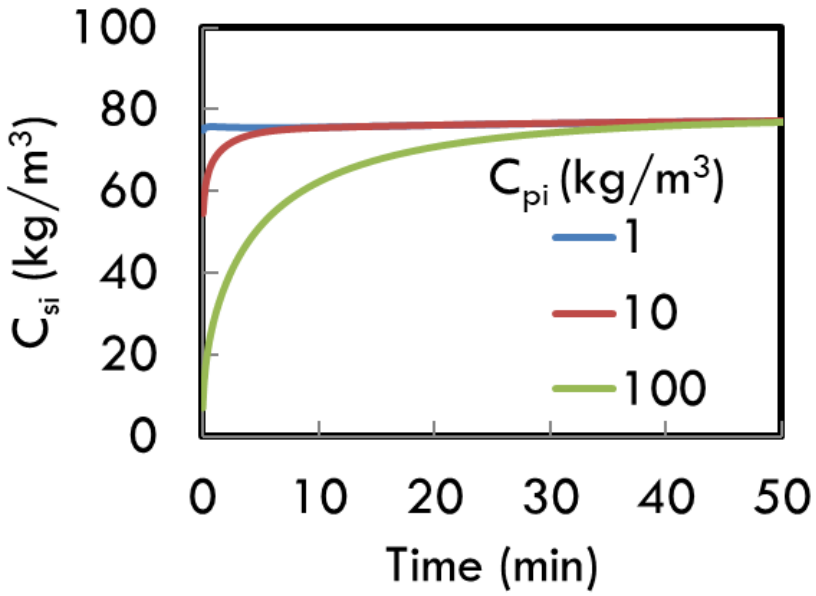

Figure 4-14: Time evolution of the dissolved wax concentration at the deposit-oil interface, C_{si} for different values of C_{pi}, keeping $k_c = 10^{-5}$ m/s, $k_r = 10s^{-1}$.

Similar to the behavior when k_c is increased, decreasing C_{pi} leads to a transition from mass-transfer-limited growth to heat-transfer-limited growth, as evident from the time evolution

of temperature and concentration of dissolved wax at the interface, shown in Figures 4-13 and 4-14.

Next, we discuss the effect of the first order precipitation rate coefficient, k_r (with units of inverse time), which controls the rate at which dissolved waxes turn into solid waxes. Figures 4-15 to 4-17 show how the deposit thickness, deposit-oil interface temperature T_i, and the interface dissolved wax concentration C_{si} are influenced by k_r.

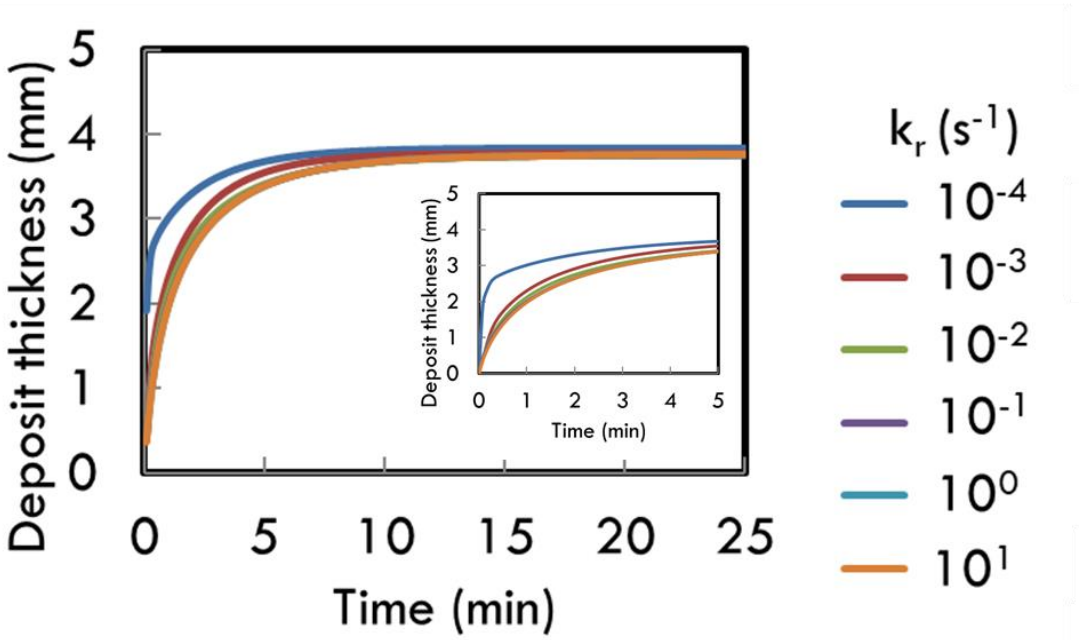

Figure 4-15: Time evolution of deposit thickness for different values of k_r, keeping $k_c = 10^{-5}$ m/s, C_{pi} = 10 kg/m^3 (1.25 wt%). Inset shows the change in deposit thickness during the first 5 minutes.

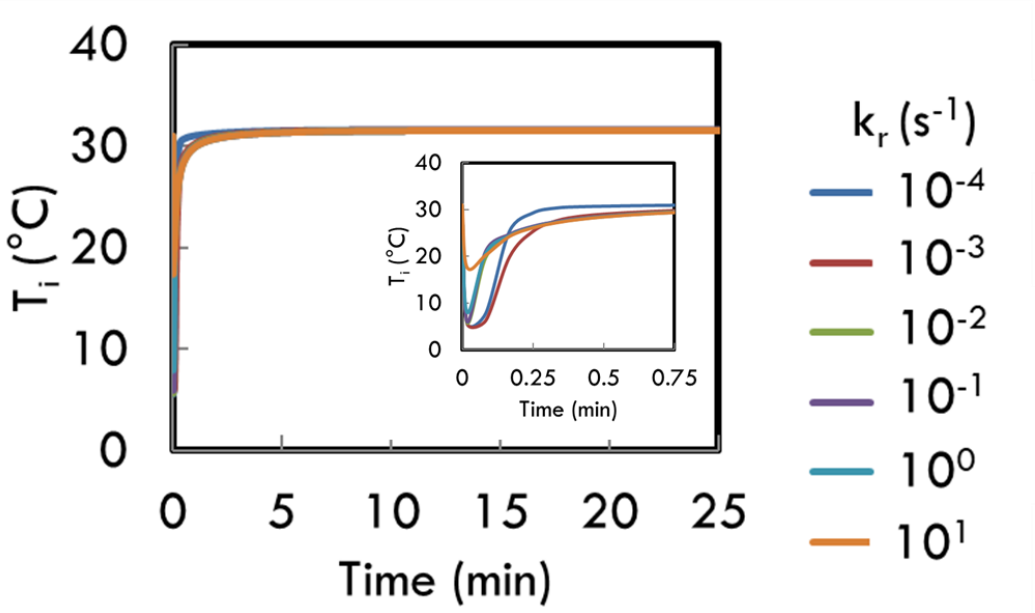

Figure 4-16: Time evolution of the temperature at the deposit-oil interface, T_i for different values of k_r, keeping $k_c = 10^{-5}$ m/s, $C_{pi} = 10$ kg/m^3 (1.25 wt%). Inset shows the change in T_i during the first two minutes.

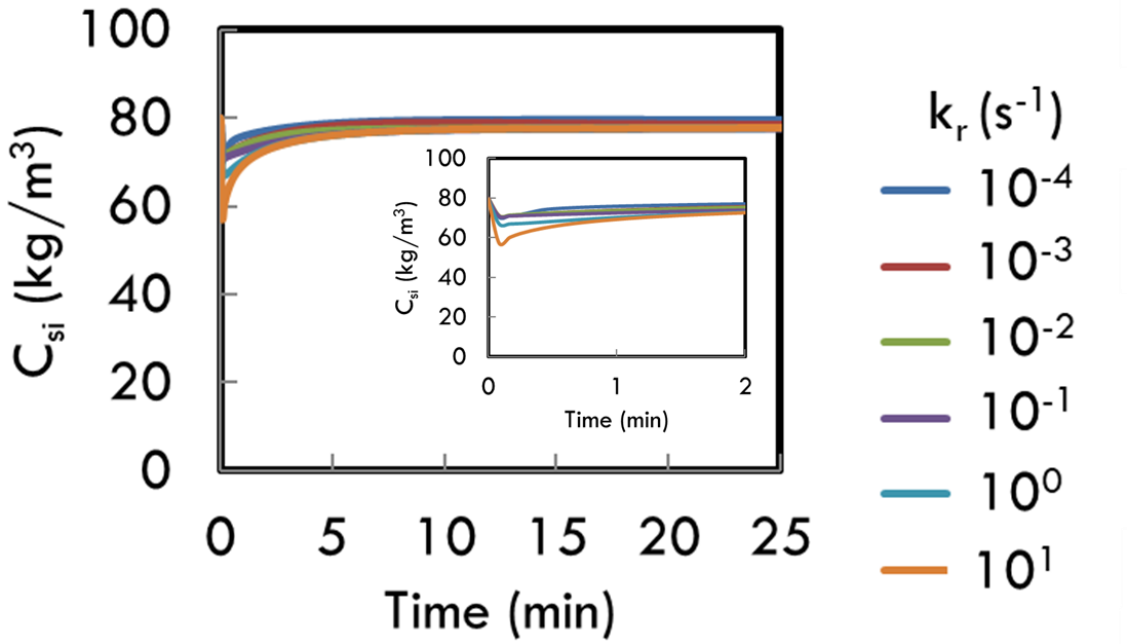

Figure 4-17: Time evolution of the dissolved wax concentration at the deposit-oil interface, C_{si} for different values of k_r, keeping $k_c = 10^{-5}$ m/s, $C_{pi} = 10$ kg/m^3 (1.25 wt%). Inset shows the change in C_{si} during the first two minutes.

Figure 4-15 shows that increasing k_r lowers the growth rate of the deposit thickness. This trend is rather surprising considering that one would think a higher rate of solid wax generation would lead to a faster advance of the deposit front. However, recall that k_r controls the rate of solid wax generation *inside* the deposit domain, not at the deposit-oil interface. A higher k_r contributes to a steeper dissolved wax concentration profile inside the deposit. This results in a higher rate of dissolved waxes diffusing further into the deposit and thus less wax available to advance the deposit-oil interface. The thinner deposit at higher k_r does not mean that less wax is deposited. In fact, the reverse is true; the higher deposition rate and thinner deposit leads to faster mass transfer to the deposit and therefore more precipitated wax, albeit concentrated into a thinner layer. This is demonstrated in Figure 4-18 where the total mass of precipitated wax in the deposit is plotted against time and deposit thickness.

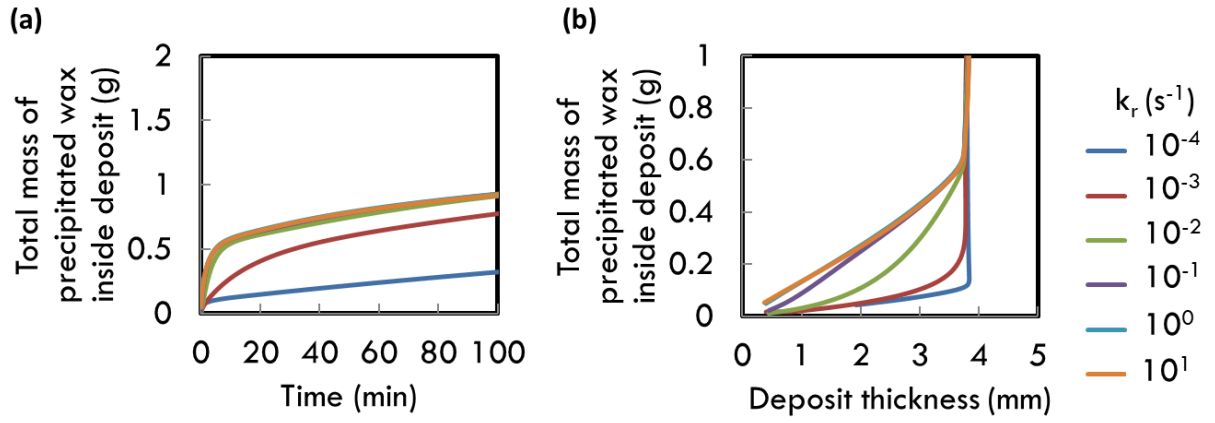

Figure 4-18: (a) Mass of precipitated wax inside the deposit vs. time, (b) Mass of precipitated wax inside the deposit vs. deposit thickness, for different kr.

The rate of precipitation also affects the rate of latent heat generation due to precipitation, as would expect, and this could alter the temperature profile. Indeed, as can be seen in the inset of Figure 4-16, at the earliest times T_i is actually higher at larger k_r despite having a thinner deposit during the early deposition. This is the result of having a greater latent heat release inside the deposit, which offsets the heat conduction to the cold finger and leads to a higher T_i.

Based on the trends shown, we conclude that increasing k_r leads to a transition from heat-transfer-controlled to mass-transfer-controlled growth (as shown by the increasing deviations of T_i and C_{si} from WAT and C_{sb} respectively). Similar to changing k_c and C_{pi}, increasing k_r beyond 1 s^{-1} does not lead to a further change in the behavior, because above this value of k_r precipitation reaches near equilibrium at every point within the sample, and the deposition rate then depends only on the mass transfer rate at the interface. The importance of the precipitation rate can be assessed through the diffusive Damköhler number $Da = \frac{k_r \delta^2}{D_{eff}}$. As the deposit thickness grows, Da grows, but for k_r = 1 s^{-1} Da greatly exceeds unity even for deposits as thin as 0.1 mm, indicating that this reaction rate is high enough to make the reaction virtually instantaneous over the whole deposition process.

In a previous work[49], it was shown that the finite volume of jacketed beaker could result in the depletion of wax in the oil over time as the deposit ages, which leads to a shrinkage of the deposit thickness, although the total mass of precipitated wax continue to increase. This feature is retained in the current model as shown in Figure 4-19 where the jacket radius was set to the experimental value of 32.5 mm. The rest of the parameters were taken from Table 4-3.

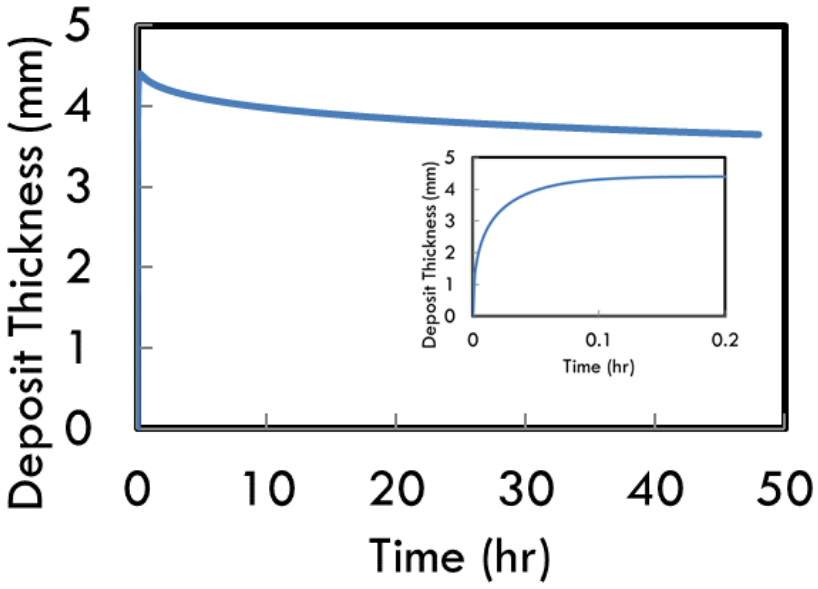

Figure 4-19: Predicted deposit thickness over long times for the experimental jacket radius, showing shrinkage due to depletion of wax in the bulk. The inset shows the shorter-time behavior.

4.6 Dimensionless Group Controlling Deposit Growth

In this section, a characteristic length and a dimensionless group are introduced to determine whether heat transfer or mass transfer controls the rate of deposit growth. The first of these is the heat transfer *characteristic length*, L_H.

$$L_H = \frac{k}{h_i}\left(\frac{WAT - T_{cw,avg}}{T_b - WAT}\right) \tag{4-33}$$

L_H provides an estimate of the maximum deposit thickness attainable under heat-transfer-controlled growth. An analogous characteristic mass transfer thickness L_M proportional to $\frac{D_{eff}}{k_c}$ could be defined. Roughly speaking, these thicknesses are those for which the corresponding Biot number is roughly unity; i.e., the thickness at which the internal and external resistances to heat or mass transport are equal.

The dimensionless group is a Biot ratio number (Bir). The conventional Biot number $\frac{h_i \delta}{k}$ is defined as the ratio of resistance δ/k to heat transfer within a body of thickness δ due to conduction, to resistance $1/h_i$ to heat transfer through a boundary layer outside of that body. An analogous mass transfer Biot number $\frac{k_c \delta}{D_{eff}}$ can also be defined. Taking the ratio of the mass transfer Biot number to the heat transfer Biot number yields Equation (4-34). This *Biot ratio* could also be obtained by taking the ratio of the heat transfer characteristic length L_H to the analogous length for mass transfer.

$$Bir = \frac{k_c}{D_{eff}} \frac{k}{h_i} = \frac{k_c}{D_{eff}} \frac{\alpha}{\hat{h}_i} \tag{4-34}$$

Here α is the thermal diffusivity, $\alpha = \frac{k}{\rho \widehat{c_p}}$, and $\hat{h}_i = \frac{h_i}{\rho \widehat{c_p}}$. When Bir >> 1, then the characteristic mass transfer thickness is less than the corresponding characteristic heat transfer thickness. Bir >> 1 means that the external mass transfer to the deposit comes into balance with the internal mass transfer before the deposit is thick enough for this balance to be reached for heat transfer. In this case, after an initial period in which the mass transfer Biot number is small and the soluble wax concentration at the front C_{si} drops below the bulk concentration C_{sb}, the mass transfer Biot number grows large enough that C_{si} reaches C_{sb} well before the heat transfer Biot number has reached unity. This leads to a heat-transfer control of the later stages of front growth. Bir << 1, on the other hand, signifies a prolonged regime in which mass transfer from the bulk to the interface limits the growth of the deposit. For cases where C_{pi} is close to zero, calculation of Bir allows easy identification of the conditions under which either a gelation-only model or a more comprehensive model would be needed to estimate the growth of a wax deposit. We now compute Bir and L_H for several set of conditions, including the ones previously shown in Figures 4-19 through 4-11, and the new ones presented in Table 4-4.

The two cases with lowest k_c discussed in Section 4.5 have a Bir of 1.1 and 0.12 respectively. Recall that these are the ones that have very slow growth rates. This low value of Bir, around unity or less, supports the previously discussed observations that these cases are dominated at long times by external mass transfer. Note that in these hypothetical cases where we decrease the k_c, we kept the heat transfer coefficients the same. In real systems, when k_c is low, for instance in a viscous oil, the heat transfer coefficients will also be low, hence Bir is not necessarily less than unity when k_c is low.

Several other cases where T_{jac}, and h_i were varied to yield different final thicknesses are also shown in Table 4-4. It can be seen that the simple estimate of L_H correlates well, but is generally larger than the final deposit thickness from simulations. Thus, L_H does indeed provide a quick measure of the final deposit thickness.

Table 4-4: L_H and Bir for various cases. Parameters not shown in this table are the same as Table 4-3. *These are the same cases from Section 4.5.

T_{jac} (°C)	h_i (W/m2/°C)	k_c (m/s)	Final deposit thickness from simulation (mm)	L_H (m)	Bir
*35	250	10^{-4}	3.8	5.1	108
*35	250	10^{-5}	3.8	5.1	11
*35	250	10^{-6}	3.8	5.1	1.1
*35	250	10^{-7}	3.8	5.1	0.12
35	200	10^{-4}	4.6	6.3	133
35	200	10^{-5}	4.6	6.3	13.4
35	200	10^{-6}	4.6	6.3	1.35
35	300	10^{-4}	3.3	4.2	89
35	300	10^{-5}	3.3	4.2	8.9
35	300	10^{-6}	3.3	4.2	0.89
33	250	10^{-4}	8.0	12.4	108
33	250	10^{-5}	8.0	12.4	10.7
33	250	10^{-6}	8.0	12.4	1.08
37	250	10^{-4}	2.5	3.2	108
37	250	10^{-5}	2.5	3.2	10.7
37	250	10^{-6}	2.5	3.2	1.07

4.7 Theoretical (With Yield Stress) vs. Experimental Deposit Thickness – Binary n-C28/nC12 Deposition

In this section, the deposit thickness trend and wax composition as a function of stirring rate are discussed. Changing the stirring rate in the cold finger system is expected to have effects analogous to those produced by changing the flow rate in a pipe flow. Heat and mass transfer rates are expected to be larger due to enhanced convective transport (corresponding to higher heat and mass transfer coefficients). In addition, a higher flow rate and thus a higher wall shear stress should shift C_{pi} to a higher value as a deposit with a higher solid content is required to withstand the higher stress imposed. To determine if C_{pi} influences significantly the growth rate of wax deposits in the cold finger apparatus, experiments were carried out at different stirring rates.

In these tests, the jacketed beaker setting temperature, T_{jac}, was maintained at 35 °C, and the cold finger thermostatic bath set point, T_{cf}, was kept constant at 5 °C. Figure 4-20 shows the deposit thickness as a function of time for a binary mixture consisting of 90wt% n-C12 and 10wt% n-C28 at the three different stirring rates of 112, 174, and 417 rpm, where rates higher than these were avoided to prevent the vortex height from exceeding the height of the container. Because of the dependence of the vortex height on stirring speed, the height of the cold finger immersed in the oil and the surface area of the jacket beaker in contact with the oil changed with stirring speed, and these changes are accounted for in the modeling.

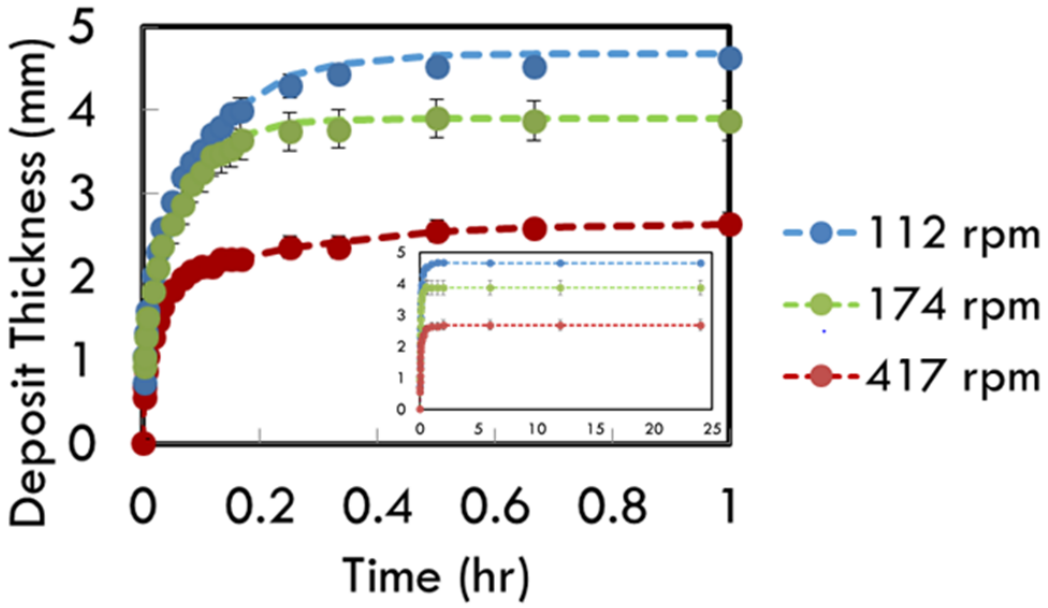

Figure 4-20: Deposit thickness versus time at different stirring rates, keeping T_{jac} at 35°C and T_{cf} at 5°C. Inset shows deposit thickness over the initial 1hr. The dashed lines serve as a guide to the trend.

Figure 4-20 shows that the deposit thickness increases over a period of around 30 minutes and then reaches a plateau. As the deposit thickens, it increasingly insulates the cold finger from the heat of the oil bath, eventually decreasing the heat flow into the cold finger to the point that it can be balanced by the heat flow from the jacket to the reservoir, so that the heat-transfer Biot number $\frac{h_i \delta}{k}$ reaches approximately unity, leading to the steady state. When the stirring rate increases, we see in Figure 4-20 that the deposit thickness decreases. At the higher stirring rate, the measured heat transfer coefficient, given in Figure 4-21, is higher, and a thinner deposit thickness δ, with a steeper temperature gradient and faster heat diffusion, is able to balance the heat transfer from the bath and bring the Biot number $\frac{h_i \delta}{k}$ to near unity, producing a steady state.

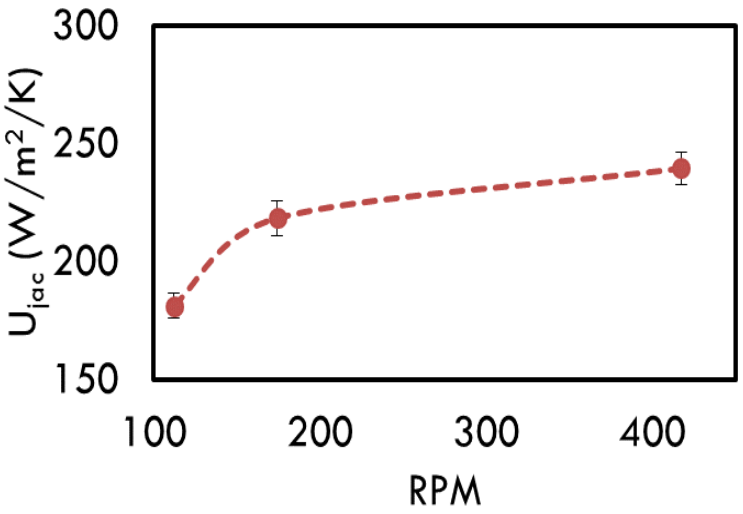

Figure 4-21: Overall jacket heat transfer coefficient, U_{jac} as a function of stirring rate.

It is important to remember that the critical solid wax concentration C_{pi} may also increase with increasing stirring rate. Thus, the decreasing deposit thickness with increasing stirring rate may not be completely explained by the increase in heat transfer coefficient alone, but could also be due to an increase in C_{pi}. However, as we will show, our experiments *with a single-component wax* have practically no influence of C_{pi}, which can therefore be taken to be zero.

Samples of the wax deposit were analyzed using HTGC after being collected from the outer edge of the deposit, which is directly behind the gel-oil interface, and from the inner edge, which is on the outer cold finger wall at the different times. Figure 4-22 shows that the fractions of the n-C28 in the outer and inner edges of the deposit, which includes both precipitated n-C28 and dissolved n-C28 trapped in the pore spaces of the deposit, start at the bulk solution value of 10wt% and increase with time, even well after the deposit thickness plateaus at around 30 minutes (see Figure 4-20). These results indicate that n-C28 in the bulk oil continues to diffuse into the gel, densifying the precipitated wax deposit. Figure 4-22 also demonstrates that the fraction of n-C28 is higher with a higher stirring rate. This experimental observation is a consequence of the thinner deposit and hence the increase in the concentration-gradient driving

force for diffusion. In addition, the mass transfer coefficient k_c also increases with the stirring rate (Figure 4-23), which delivers more wax to the deposit.

Note that, over time, the fraction of n-C28 at the outer edge of the deposit becomes higher than at the inner edge. Owing to the initially fast growth of the deposit, its composition of n-C28 is initially nearly uniform at around that of the bulk oil; that is, around 10wt%. Because the precipitation rate at the outer edge of the deposit is greater than that deeper within, the outer edge eventually becomes more enriched in n-C28 than does the inner edge.

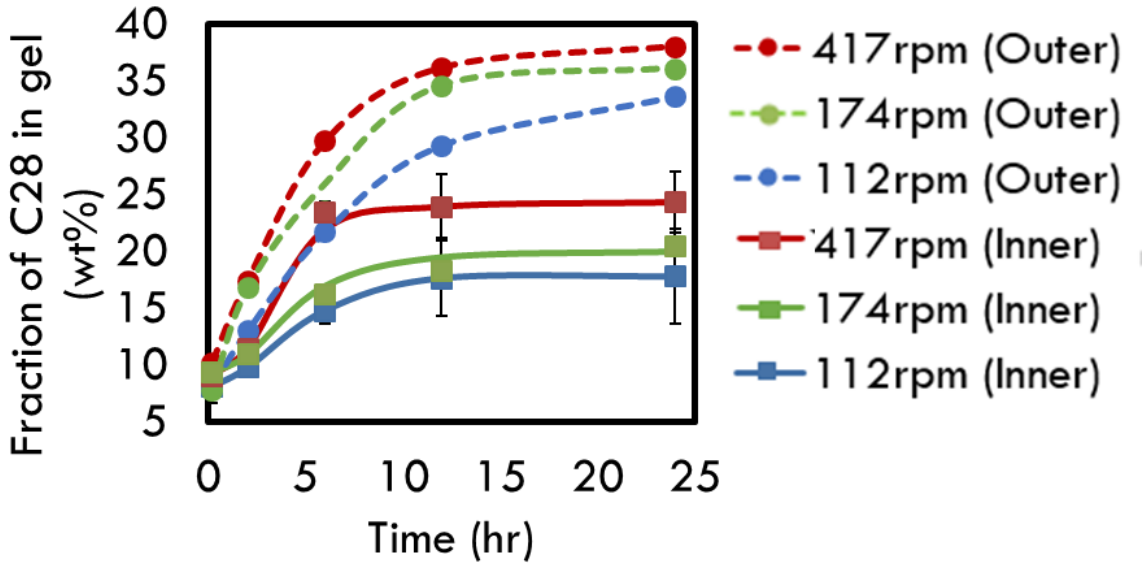

Figure 4-22: Fractions of C28 in the deposit from the outer and inner edges of the deposit as a function of time.

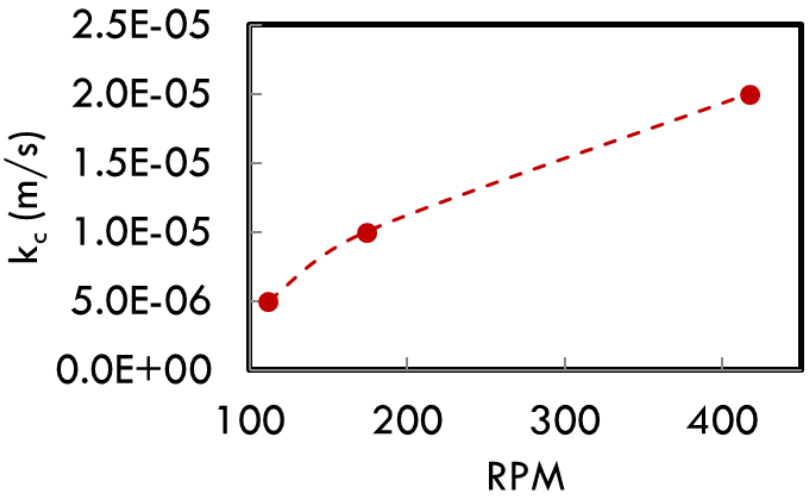

Figure 4-23: Measured mass transfer coefficient, k_c as a function of stirring rate.

We now use the model to simulate the results of deposition at the lowest and highest stirring rates, 112 and 417 rpm. All parameters are listed in Table 4-5. We take the precipitation rate constant k_r to be $1s^{-1}$, which is asymptotically fast so that higher values produce the same results, and C_{pi} is taken to be 0.

Table 4-5: Parameters used to simulate the highest and lowest stirring rate cold finger experiments, 112 & 417 rpm.

Parameter	112 rpm	417 rpm
T_{jac} (°C)	35	35
$T_{cw,avg}$ (°C)	7.1	8.2
$r_{cf,outer}$ (m)	0.005	0.005
r_{jac} (m)	0.0325	0.0325
L_l (m)	0.07	0.08
L_{cf} (m)	0.06	0.055
ρ (kg/m^3)	800	800
$\hat{c}_p$ (J/kg/°C)	2100	2100
ΔH (J/kg)	200,000	200,000
k (W/m/°C)	0.16	0.16
U_{jac} (W/m^2/°C)	181	240

h_i (W/m^2/°C)	216	410
h_{cf} (W/m^2/°C)	1720	3160
V_A (cm^3/mol)	507	507
K_α	10	10
C_{sb}(kg/m^3), t = 0	80 (10wt%)	80 (10wt%)
k_c (m/s)	5 x 10^{-6}	2 x 10^{-5}
k_r (s^{-1})	1	1
C_{pi} (kg/m^3)	0	0
C_{pb}(kg/m^3)	0	0

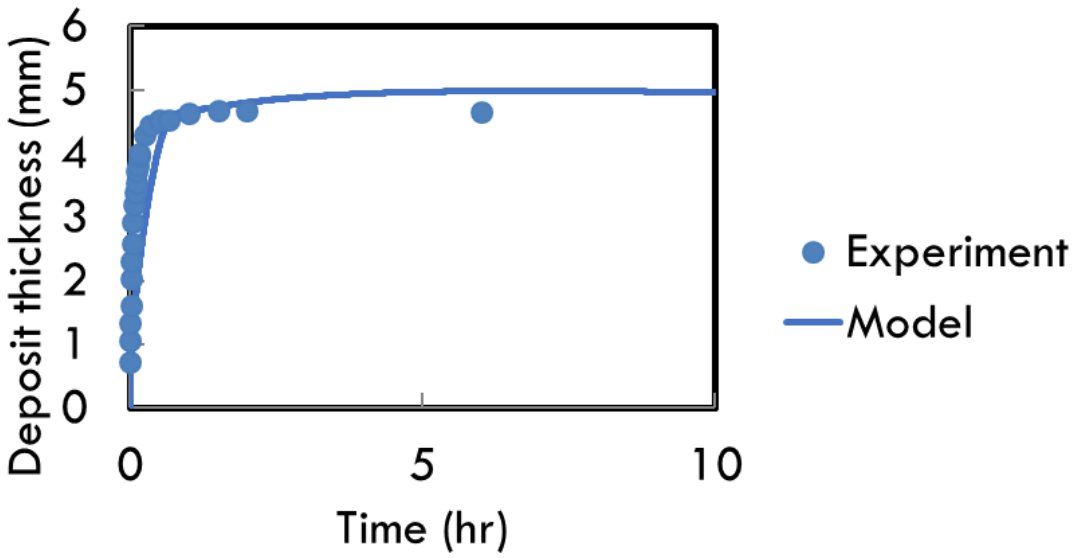

Figure 4-24: Deposit thickness vs. time for the lowest stirring rate, 112 rpm.

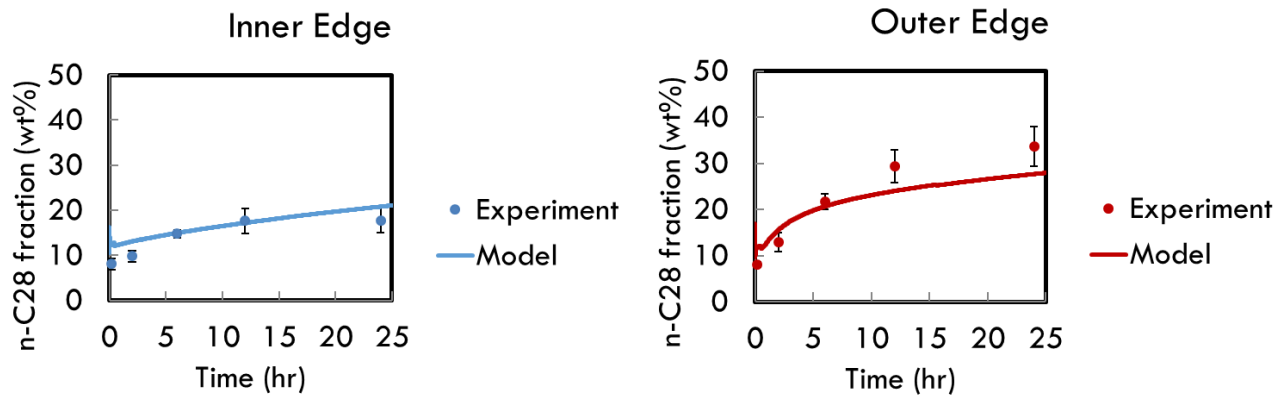

Figure 4-25: Inner and outer deposit compositions for the lowest stirring rate, 112 rpm. To obtain the plotted predictions at the inner and outer edge, the predicted wax composition profiles, including both precipitated and dissolved wax, were integrated over the inner and outer 2 mm of the deposit (when thickness is greater than 4 mm) or the inner and outer halves of the deposit (when thickness is less than 4 mm).

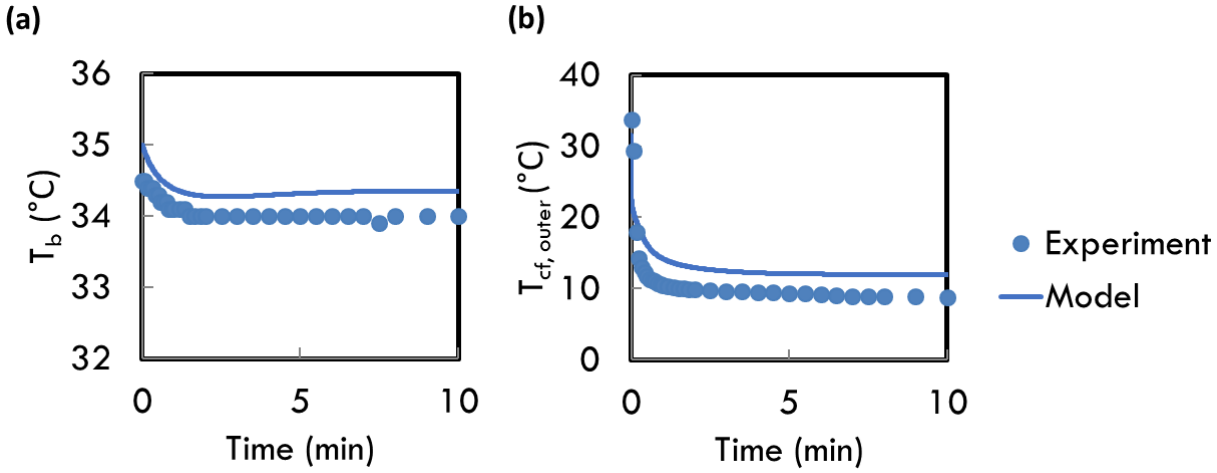

Figure 4-26: (a) Bulk temperature T_b vs. time, and (b) cold finger outer surface temperature, $T_{cf,outer}$ vs. time for the lowest stirring rate, 112 rpm.

Figures 4-24 through 4-26 show that for the lowest stirring speed the model captures nearly quantitatively the deposit thickness growth as well as the time evolution of deposit composition and temperatures by assuming fast precipitation and $C_{pi} = 0$, which implies that the wax forms a gel as soon as the first precipitates form.

The corresponding good agreement between predictions and measurements for the fastest stirring speed, 417 rpm, are shown in Figures 4-27 through 4-29 again with the same values of k_r

and C_{pi}, but with increased values of heat and mass transfer coefficients, in accord with the values given in Table 4-5. Comparing these results with those of Figures 4-24, 4-25, and 4-26 shows that the deposit thickness decreases with increasing stirring rate. Since the same model predicts both results for high and low stirring speeds, with the same model and model parameters except for the measured heat and mass transfer coefficients and to some extent the height of the liquid and the cooling water temperature, it follows that the thinner deposit at higher stirring speed can be explained solely by the increase in heat and mass transfer rates in the jacketed beaker. These comparisons show that: (1) the model successfully captures deposition in the cold finger at two stirring rates, and (2) the binary n-C12-n-C28 model oil does not behave like a complex wax mixture due to the fact that it easily forms a solid gel at low C_{pi}, low enough to be set to zero, and the deposit growth rate is predominantly controlled by the heat transfer rate. The *Biot ratio* for the lowest and highest stirring rate experiments discussed here are 37 and 76 respectively, well into the heat-transfer-dominated regime.

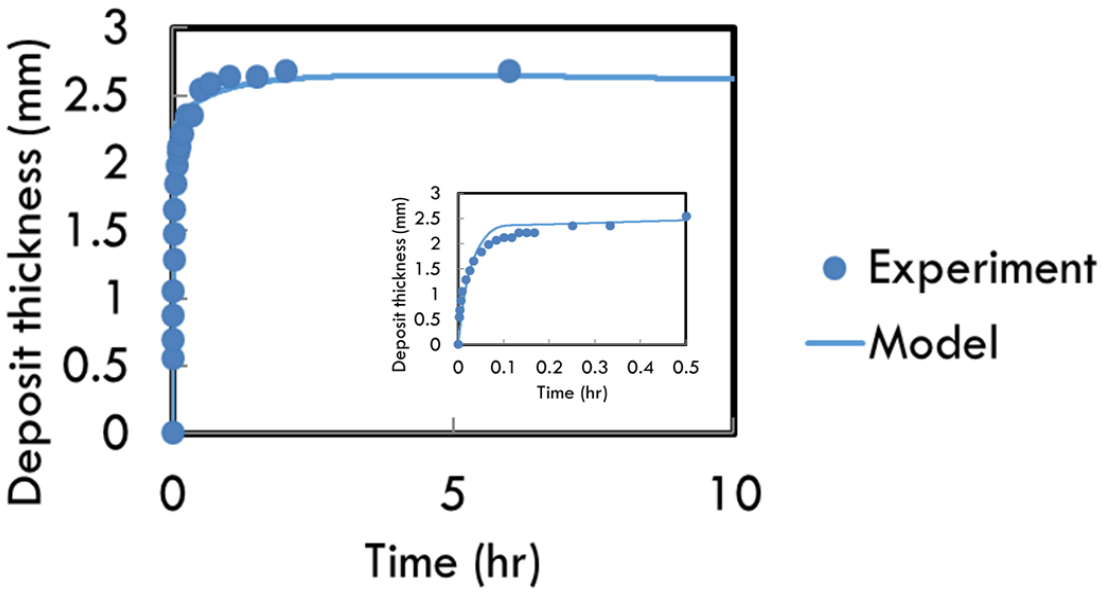

Figure 4-27: Deposit thickness vs. time for the highest stirring rate, 417 rpm. The inset shows the deposit thickness during the first half hour.

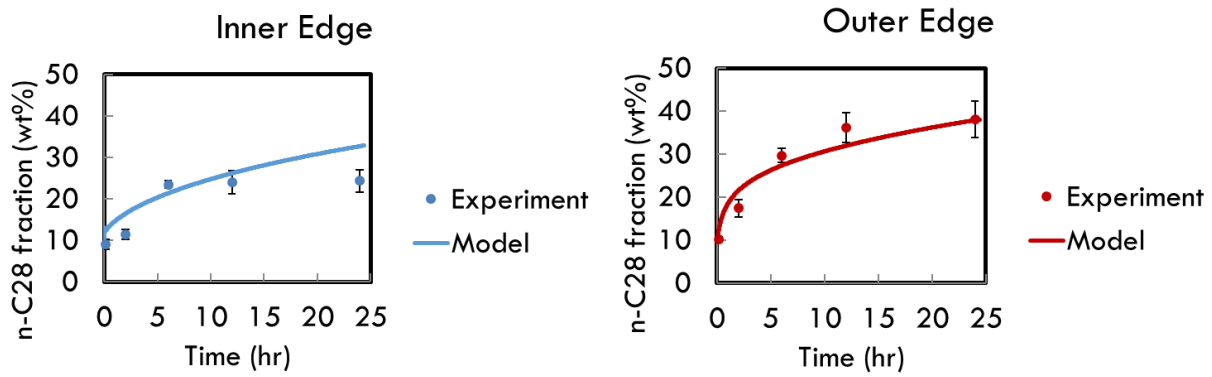

Figure 4-28: Inner and outer deposit compositions for the highest stirring rate, 417 rpm. To obtain the plotted predictions at the inner and outer edge, the predicted wax composition profiles, including both precipitated and dissolved wax, were integrated over the inner and outer halves of the deposit.

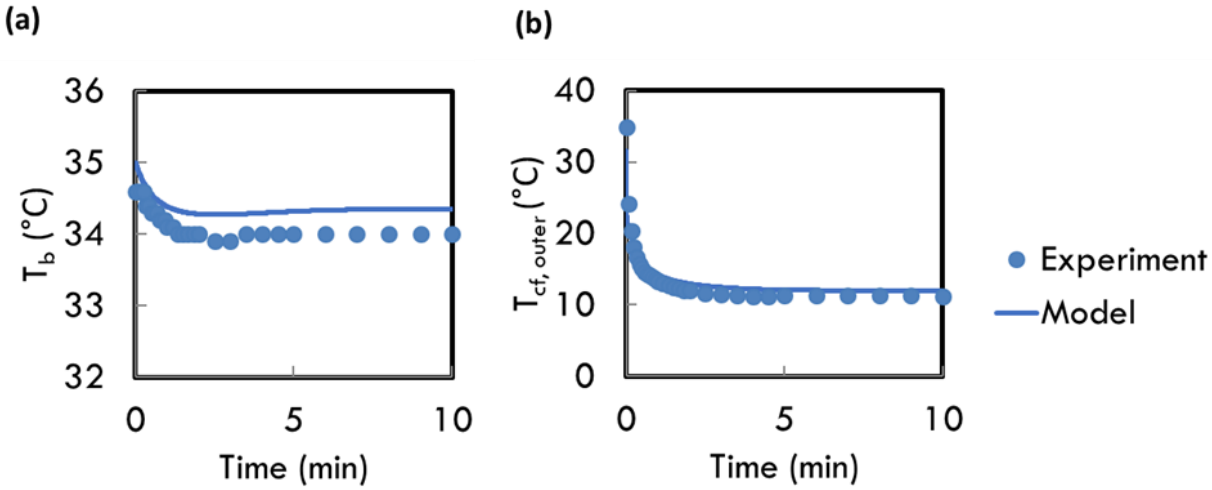

Figure 4-29: (a) Bulk temperature T_b vs. time, and (b) cold finger outer surface temperature, $T_{cf,outer}$ vs. time for the highest stirring rate, 417 rpm.

To identify if the *Biot ratio* can ever be less than unity in real waxy oils, we will now recast the *Biot ratio* definition in terms of Nusselt number, Nu and Sherwood number, Sh. Nu and Sh are typically related to the Reynolds number, Re, Prandtl number, Pr, and Schmidt number, Sc, in the following forms:

$$Nu = \frac{h_i L}{k} = a_h \, Re^b \, Pr^c \tag{4-35}$$

$$Sh = \frac{k_c L}{D_{w/o}} = a_m \, Re^b \, Sc^c \tag{4-36}$$

In Equations (4-35) and (4-36), a_h, a_m, b, and c are constants, and L is a characteristic length, in our case the radius of the cold finger. These equations can be rearranged to obtain h_i and k_c, and upon substituting these into Equation (4-34), the following form of *Biot ratio* can be obtained:

$$Bir = \left(\frac{a_m}{a_h}\right)\frac{D_{w/o}}{D_{eff}}\left(\frac{Sc}{Pr}\right)^c = \left(\frac{a_m}{a_h}\right)\frac{D_{w/o}}{D_{eff}}(Le)^c \tag{4-37}$$

The ratio Sc/Pr is also known as the Lewis number, Le, which is the ratio of thermal diffusivity α to the mass diffusivity $D_{w/o}$. The ratio $\frac{D_{w/o}}{D_{eff}}$ is equal to or greater than unity and increases with time as the deposit gets denser with solid precipitated wax. The diffusion coefficients α and $D_{w/o}$ are approximately 10^{-7} and 10^{-10} m^2/s respectively for oils, so that Le is on the order of 10^3. The exponent c is typically less than unity, and for stirred tanks it has been found to be 0.5.[51] The coefficients a_h and a_m are similar in magnitude and we can take their ratio to be of order unity. This puts the *Biot ratio*, according to Equation (26), within the range between 10 and 100, well above unity. This analysis shows that for cases where C_{pi} is close to zero, gel growth rate should always be heat-transfer controlled, as suggested by Mehrotra and coworkers[21,27,29,30,32,36,40–42].

4.8 Theoretical (With Yield Stress) vs. Experimental Deposit Thickness – Dilute n-C36/mineral oil Deposition

A condition that could push deposit growth into the mass-transfer-controlled regime is when C_{pi} is significantly above zero. To demonstrate such a case, we ran a deposition experiment using a dilute waxy model oil composed of 0.8wt% n-C36 in a light mineral oil (Crystal Plus

tech-grade mineral oil CP 70T from STE Oil) that was barely able to form a gel at a temperature as low as 5°C due to its low wax content despite having a WAT of 40°C. We found that the growth of gel thickness of this oil at 5°C cold-finger temperature was not only slow and unable to be explained by transient heat transfer, but was also non-monotonic, with the gel sometimes breaking free from the cold finger and then re-growing. Sampling of the deposit just after it had formed also showed that the gel contained a total wax with a concentration approximately six times the wax concentration in the oil, signifying that enrichment of precipitated wax near the vicinity of the cold finger occurred first before a stable gel was able to form.

These observations support our earlier prediction that a finite value of C_{pi} can slow down the growth rate. We compared the predictions of our model to these experimental results in Figure 4-30 and Table 4-6. The parameters used for this simulation are shown in Table 4-7, where all except C_{pi}, k_r, and K_α were either measured or known apriori. Both k_r and K_α were kept the same as those used in previous experiments for the 10wt% n-C28 oil ($k_r = 1\ s^{-1}$ for fast precipitation, as is reasonable and $K_\alpha = 10$). C_{pi} on the other hand was adjusted to 43 kg/m^3 or around 5 wt% wax to fit the data at long times. Results using $C_{pi} = 0$ are shown in a dashed line for comparison.

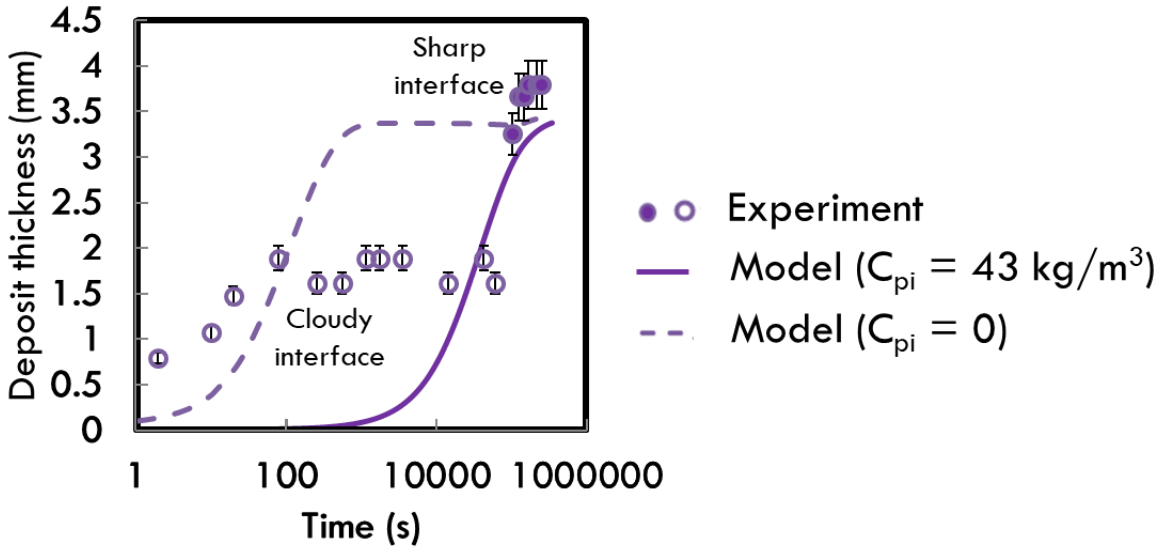

Figure 4-30: Experimental vs. theoretical deposit thickness for the deposition of 0.8wt% n-C36 in mineral oil. Note that the time axis is in log scale.

Table 4-6: Experimental vs. theoretical deposit wax content for the deposition of 0.8wt% n-C36 in mineral oil.

Time when deposit was collected	Experimental total n-C36 concentration of deposit (wt%)	Theoretical total n-C36 concentration of deposit (wt%)
24 hr	4.8	5.9
96 hr	9.8	10.8

Table 4-7: Parameters used to generate the curve shown in Figure B-2 and theoretical total n-C36 concentration of deposit in Table B-1.

Parameter	
T_{jac} (°C)	44
$T_{cw,avg}$ (°C)	6.7
$r_{cf,outer}$ (m)	0.005
r_{jac} (m)	0.090
L_l (m)	0.185
L_{cf} (m)	0.06
ρ (kg/m^3)	853

$\hat{c}_p$ (J/kg/°C)	2100
ΔH (J/kg)	200,000
k (W/m/°C)	0.16
U_{jac} (W/m^2/°C)	163
h_i (W/m^2/°C)	321
h_{cf} (W/m^2/°C)	2830
V_A (cm^3/mol)	507
K_α	10
C_{sb}(kg/m^3), t = 0	6.8 (0.8wt%)
C_{pb}(kg/m^3), t = 0	0
k_c (m/s)	5 x 10^{-7}
k_r (s^{-1})	1
C_{pi} (kg/m^3)	43 (5wt%)

The results in Figure 4-30 suggests that C_{pi} changes from a small value at short times, needed to fit the early-time deposition, but then abruptly increases as the deposit becomes thicker and heavier, leading to breakage and sloughing of deposit beyond the initial thin layer, until mass transfer delivers enough wax that a denser deposit with higher C_{pi} can be deposited. The breakage is likely initiated near the surface of the gel by the flow. Because n-C36 crystals are relatively large in size and are very ordered, any breakage occurring on the surface may trigger a chain reaction of breakage deeper into the gel, causing a significant drop in the deposit thickness. We expect that for a multicomponent oil, where the crystals are much smaller and more circular, such a breakage would not cause a significant decrease in deposit thickness. Rather, the growth should be rather smooth and monotonic.

A more in-depth study on dilute and multicomponent waxy oils must be carried out to fully understand the significance and impact of C_{pi} on deposition and to identify if the cases with

higher C_{pi} values presented in Chapter 4.5 are realistic. Such a study could include varying the initial concentration of wax in the oil and the stirring rate.

4.9 Conclusions

An experimental technique to measure wax deposition thickness as a function of time via visual monitoring in the Cold Finger apparatus was implemented. Using this technique, the wax deposition thickness versus time was measured and recorded for various jacket and cold finger temperatures. Three model systems were used to study wax deposition: pure n-C28, a binary mixture of n-C28 and n-C12, and a dilute mixture of n-C36 and mineral oil.

The deposition of pure n-C28 is governed only by conventional heat transfer and solidification physics, as one would expect. The heat transfer model accurately predicted the deposit thickness as a function of time after the heat transfer coefficients from jacket to bulk stirred oil, and from this oil to the deposit had been measured and used in the prediction.

The deposition of wax from a binary mixture of 10wt% n-C28 and 90wt% n-C12 is governed by heat transfer, mass transfer and solubility of wax, where these processes are coupled. It was found that the initial growth of the deposit is governed by transient heat transfer and for very short times (i.e. $t < 20$ minutes), the deposit composition, which includes both solidified n-C28 wax and the oil entrained within its pore spaces, was nearly identical to that of the oil. However, over longer times, as the deposit ages, enrichment of solid within the deposit due to inward diffusion of n-C28 and consequent expulsion of n-C12 occurs and has a pronounced effect on deposit density and hardness.

For the lowest cold-finger temperatures, the thickness of the deposit formed from a binary mixture of n-C28 and n-C12 also eventually decreases over time as the deposit ages. It was found that this decrease in deposit thickness is due to a gradual decrease in the WAT of the

oil phase which is a result of a decrease in n-C28 concentration in the n-C12 oil due to the continued diffusion of soluble n-C28 into the wax deposit, and its consequent depletion in the oil. An experiment in which the oil WAT is kept constant prevented the decreased in deposit thickness at long time, and thus confirmed the effect of oil phase WAT on the deposit thickness.

The deposition of wax from a dilute mixture of 0.8wt% n-C36 in mineral oil behaves differently from that of a binary mixture of 10wt% n-C28 and 90wt% n-C12. It was found that the growth of the deposit is slow, taking more than 20 hrs to reach a gel with a stable thickness. Further, the deposit sometimes was observed to slough off into the oil due to a weak gel. It was concluded that dilute waxy oils require enrichment of precipitated waxes locally before a stable gel can form. As a result, the gel growth is slow and limited by the rate of mass transfer of wax molecules to the surface. Once a stable deposit has formed, the deposit ages in a similar manner to other wax deposits.

A new transport model has been developed that predicts the formation of paraffin wax deposits and their aging from wax-containing oils. The behavior of the model was explored and compared with results measured in a cold-finger experiment. The model includes transient energy and mass balances that must be solved simultaneously while allowing for the possible effects of yield stress on the deposition through a critical solid wax concentration at the deposit-fluid interface, C_{pi}. This new parameter is the precipitated wax concentration needed to withstand the shear stress imposed by the flow at the interface and reflects the dependence of the deposit yield stress on precipitate concentration and the fluid shear stress at the interface. While most our studies in a cold finger apparatus, with a single dissolved wax component at 10% by weight, show no indication that C_{pi} is significantly different from zero, we did find indications of its importance when wax content in the oil is low, around 1%. In addition, we expect its influence

to be much more significant for multi-component waxes for which precipitation occurs more gradually with changing temperature than for a single-component wax. We also allow the phase change from dissolved to precipitated wax to have a finite rate following a first-order reversible reaction rate law, but find our experimental results are explained well using an asymptotically high rate, implying instantaneous equilibrium can be assumed between precipitated and dissolved wax.

The most influential parameters in our experiments, namely the heat and mass transfer coefficients, are measured in the cold-finger apparatus at different stirring speeds, and the measured values are used in successful predictions of experimental results. Because of the reversible phase change, the model can predict the redissolution of precipitated waxes that may occur during deposit aging, which has been observed experimentally. In addition to obtaining the time evolution of the deposit thickness, this model also correctly predicts: (1) the spatial and temporal evolution of temperature and wax concentration in the deposit, and (2) the temporal evolution of temperature and wax concentration in the fluid which are assumed to be spatially uniform. We also identify a new dimensionless group, the *Biot ratio* Bir, which controls whether the approach to a final deposit thickness in an infinite oil bath is controlled by mass transfer (for low Bir) or by heat transfer (for high Bir). For oils with low C_{pi} however, Bir is always high, signifying heat-transfer-controlled growth. However, even in this typical limit, mass transfer has a significant effect on the early evolution of deposit thickness and wax concentration near the front. Over intermediate times (hours), it also influences the aging of the deposit as wax migrates into its interior, increasing the concentration of precipitated wax over time. Finally, over still longer time periods (days), mass transfer governs the shrinkage of the deposit thickness as it continues to age, due to depletion of wax from the oil reservoir, and the consequent decrease in

wax appearance temperature. While the equations were developed to predict wax deposition onto a cold finger, similar equations can be adapted to other geometries as well, such as pipe flow.

4.10 Nomenclature

t	Time (s or hr)
ρ	Density of the oil and deposit (kg/m^3)
ΔH	Specific latent heat of wax crystallization (J/kg)
δ	Deposit thickness (m or mm)
k	Thermal conductivity of deposit (W/m/°C)
$\hat{c}_p$	Specific heat capacity of oil and deposit (J/kg/°C)
α	Thermal diffusivity of oil and deposit (m^2/s)
T	Temperature at a radial location in the deposit (°C)
T_{jac}	Set point temperature of heating water (°C)
$T_{jac,in}$	Temperature of water entering jacket (°C)
$T_{jac,out}$	Temperature of water leaving jacket (°C)
T_{cf}	Set point temperature of cooling water (°C)
$T_{cw,in}$	Temperature of cooling water entering cold finger (°C)
$T_{cw,out}$	Temperature of cooling water leaving cold finger (°C)
$T_{cf,out}$	Temperature on the cold finger outer surface(°C)
T_b	Temperature of the oil (°C)
T_i	Temperature at the deposit-oil interface (°C)
r	Radial coordinate (m)
$r_{cf,in}$	Inner radius of stainless steel cold finger (m)
$r_{cf,out}$	Outer radius of stainless steel cold finger (m)
r_{jac}	Inner radius of jacketed beaker (m)
L_l	Height of liquid in the jacketed beaker (m)
L_{cf}	Height of gel deposit along the cold finger axis (m)
U_{jac}	Overall heat transfer coefficient for the heat transfer between the jacket and the solution (W/m^2/°C)

U_i	Overall heat transfer coefficient for the heat transfer between the solution and the coolant inside the cold finger ($W/m^2/°C$)
h_{cf}	Heat transfer coefficient for the heat transfer between the inner wall of the cold finger and the coolant ($W/m^2/°C$)
h_i	Heat transfer coefficient for the heat transfer between the oil and the deposit ($W/m^2/°C$)
$\hat{h}_i$	Normalized heat transfer coefficient for the heat transfer between the oil and the deposit (m/s)
A_{jac}	Jacketed beaker surface area (m^2)
A_i	Deposit-oil interfacial area (m^2)
m_{liq}	Mass of oil in the reservoir (kg)
V_{liquid}	Volume of oil in the reservoir (m^3)
$m_{total\ C28}$	Total mass of n-C28 (kg)
C_s	Soluble (i.e., dispersed) n-C28 concentration (kg/m^3)
$C_{s,eq}$	Soluble wax concentration at the solubility limit (kg/m^3)
C_p	Precipitated wax concentration in the deposit (kg/m^3)
C_{sb}	Soluble wax concentration in the bulk oil (kg/m^3)
C_{pb}	Precipitated wax concentration in the bulk oil (kg/m^3)
k_r	Precipitation rate constant (s^{-1})
$D_{w/o}$	Soluble wax diffusivity in precipitate-free oil based on the Hayduk-Minhas equation (m^2/s)
D_{eff}	Effective soluble wax diffusivity in the deposit (m^2/s)
μ	Viscosity of precipitated wax-free oil (mPa s)
V_A	Molar volume of wax molecule (cm^3/mol)
K_α	Dimensionless wax crystal aspect ratio

Chapter 5 Conclusions and Future Directions

Chapter 3 is dedicated to discussing wax deposition experiments were preformed using various mixtures ranging from pure wax, to a single-component wax in a binary mixture, to a multicomponent commercial wax mixtures. This study found that gelation can happen to an oil allowing the deposit growth to be controlled by heat transfer. In other oil systems, the growth can be slow and dictated by the mass transfer rate. Regardless of which mechanism controls the growth rate, molecular diffusion of soluble waxes from the oil into the deposit continue to happen for as long as a concentration gradient exists and waxes in the oil have not been completely depleted. Another novel phenomenon that was discovered is that the aging of the deposit can lead to the shrinkage of the deposition as a result of the depletion of waxes in the oil as wax diffused into the gel for as long as a concentration gradient exists. It was found that this shrinkage tends to occur for an experimental setup with a finite volume container where depletion of wax can be significant. This study also found that shear stress impacts deposition in dilute oil systems where a much greater concentration of precipitated wax is required to form a stable gel. Here, the growth rate of the deposit is slow due to being mass transfer controlled. Other characteristics of a wax gel are retained however, such as aging of the deposit.

Chapter 4 dives deeper into the question of how the transition from heat transfer controlled to mass transfer controlled growth can occur. A model was developed that predicts concentration and temperature fields using heat and mass transport fundamentals. The model has been shown to be capable to capturing the experimental behavior as observed on the cold finger apparatus. A characteristic length and a dimensionless group, the ratio of the mass transfer to

heat transfer Biot numbers, were proposed as a quick analysis on the expected behavior of deposition. The characteristic length was found to correlate well with the final steady state thickness predicted in the case of no wax depletion in the bulk oil. This is a useful number to calculate to quickly assess the maximum possible deposit thickness at any given condition without having to solve the complete model. Using the ratio of mass transfer to heat transfer Biot numbers, it was found that for oils that can form gel at very low precipitated wax concentrations, this ratio of Biot numbers is much greater than unity, signifying that their gel growth rate is heat transfer controlled via gelation. It was then deduced that mass transfer controlled growth can only take place when the critical concentration of precipitated wax required to form a gel is much greater than zero. The findings from this dissertation help identify under what conditions wax will grow by heat transfer and at what conditions will it grow by mass transfer followed a proper mathematical tool to make these predictions. The model developed in this dissertation is also comprehensive and was validated experimentally for a pure wax and a single-component-wax binary oil.

There are still a number of uncharted territories that need to be explored to increase the accuracy of the existing deposition model. The first of these is the study on the rheological properties of these waxy mixtures, specifically the yield stress under various flow conditions and oil properties. There is currently no technique that could be taken to measure the appropriate yield stress and other relevant rheological parameters that are inputs to the momentum balance of the deposition model or the parameter C_{pi} introduced in the model developed in this dissertation. A potential approach is to utilize rheometry to find the correlation between the shear stress and the precipitated wax concentration needed to arrest flow. There are two steps to take to obtain this correlation. The first step is to measure the gelation temperature of the oil of interest, which

is the temperature where the oil stops flowing when cooled under shear. Once could perform a constant shear rate cooling of an oil sample, cooling from a temperature above the WAT to a temperature low enough that the constant shear stress imposed can no longer sustain flow of the sample. When the shear rate is monitored as a function of time (or equivalently temperature), the shear rate can be seen to decrease gradually after the temperature gets below the WAT due to the existence of a yield stress in the presence of precipitated wax, and eventually reaches zero as shown in Figure 5-1. The temperature at which the shearing stops is considered the gelation temperature and the yield stress when this arrest occurs is equal to the imposed constant shear stress. Figure 5-1 shows the behavior of two model oils previously discussed in this dissertation when subjected to this procedure.

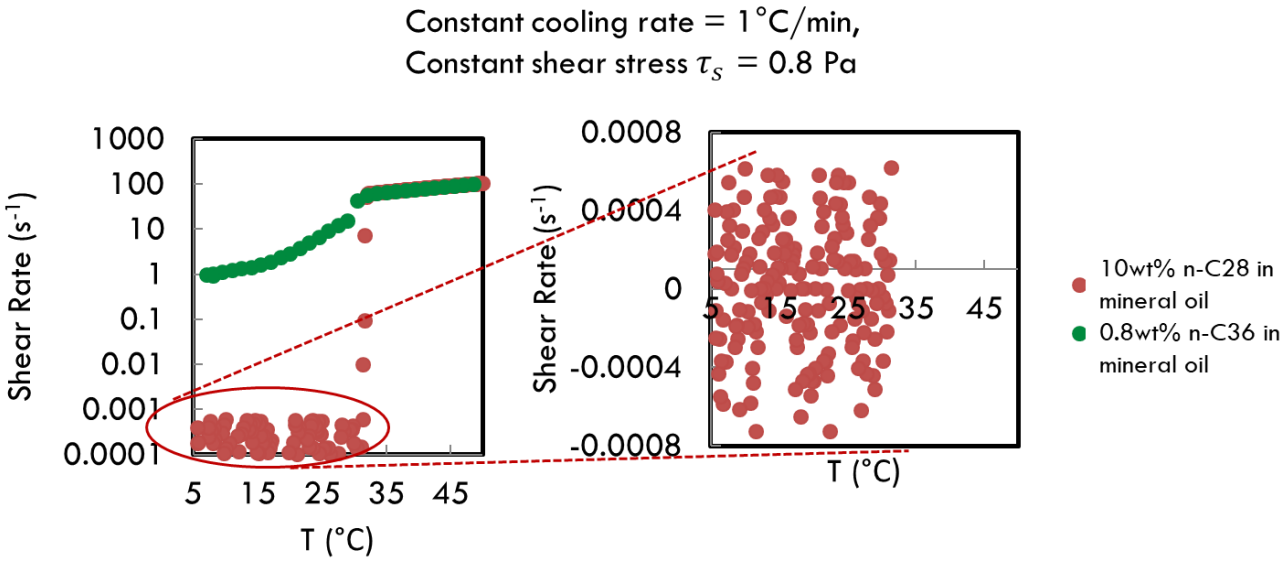

Figure 5-1: The shear rate measured as a function of temperature as the model oil was cooled from above WAT to 5°C under a constant shear stress of 0.8 Pa and a cooling rate of 1°C/min to get the gelation temperature. The fluctuation in the shear rate around zero implies that the flow has essentially arrested.

It can be seen that under the conditions tested, the dilute 0.8wt% n-C36 oil does not arrest even at 5°C whereas the 10wt% n-C28 oil gels at 33°C, consistent with the observations discussed in Chapters 3 & 4. The step two of this two-step approach to finding the relationship between yield

stress and critical solid wax concentration to form a gel, C_{pi}, is to measure concentration the of precipitated waxes at the gelation temperature measured during step one. This can be done experimentally or computationally. However, experimental measurement can be challenging for multicomponent oils. Computationally one could use comprehensive thermodynamic model that has been validated, such as the model by Coutinho[33,52,53] which has been proven to be reliable. Once C_{pi} has been obtained, one could either use this value in the model developed in Chapter 4 or take a further step and do a mapping between C_{pi} and the yield stress. This mapping can then be used in other wax deposition models that solve momentum balances. One significant challenge would be in determining the right constant shear stress and cooling rate to use in the measurements as waxy oils' rheological behavior is sensitive their cooling and mechanical histories. One would have to identify the relevant cooling and mechanical histories for a pipe or cold finger deposition, depending on the situation.

Another uncharted territory is the modeling of the transport with multicomponent waxes. Real crude oils contain a continuous distribution of wax molecules with varying molecular masses that although behave similarly, have different solubility behaviors. To take on this challenge, the existing deposition should be coupled to a reliable thermodynamic model such as the model by Coutinho. Accomplishing this would be very powerful as more real data can be benchmarked against the model. While adding the number of wax components can be numerically expensive, this feat can this be done by lumping similarly behaved waxes into a single group. For instance, a mixture with 50 wax molecules can be broken down into five groups, making computational effort easier.

To solve for the moving front problem discussed in Chapter 4 for a multicomponent diffusion, one has to deal with the increasing number of unknowns. For an oil with n number of

components, there are n number of overall wax mass balances at the front. For the k-th component, this is given by:

$$D_{eff,k}\frac{\partial C_{s,k}}{\partial r}_{i^-} + \left(C_{si,k} + C_{pi,k}\right)v_i = k_c\left(C_{sb,k} - C_{si,k}\right) + \left(C_{sb,k} + C_{pb,k}\right)v_i \tag{5-1}$$

Here, $C_{si,k}$, $C_{pi,k}$ and v_i are all unknowns, resulting in 2n +1 extra unknowns. We assume that the interface is at equilibrium, such that $C_{si,k}$ and the temperature are coupled through the thermodynamic model. This assumption together with n number of overall wax mass balances at the front bring down the number of unknown to just one. The last constraint is the precipitated wax concentration at the interface, C_{pi}, required to withstand the shear stress of the flow. For a multicomponent wax mixture, the precipitated wax concentration at the interface of each component, $C_{pi,k}$, must add up to C_{pi}.

$$\sum_{k}^{n} C_{pi,k} = C_{pi} \tag{5-2}$$

Equation (5-1) can be rearranged to obtain $C_{pi,k}$ as a function of everything else, and upon substituting this $C_{pi,k}$ into Equation (5-2) followed by a rearrangement to isolate v_i, one would arrive at the following equation:

$$v_i = \frac{\sum_k^n k_c\left(C_{sb,k} - C_{si,k}\right) - \sum_k^n D_{eff,k}\frac{\partial C_{s,k}}{\partial r}_{i^-}}{C_{pi} - \sum_k^n\left(C_{sb,k} + C_{pb,k} - C_{si,k}\right)} \tag{5-3}$$

Equation (5-3(5-1) can be used to solve for the moving front velocity v_i. After v_i is solved, one can then go back to Equation (5-1) to solve for $C_{pi,k}$ of the individual waxes, or wax groups. This approach may require an iterative procedure because of the coupling between the thermodynamic model, the front velocity and each wax mass balance. Upon solving this problem, concentration fields of all the wax components can be resolved spatially and temporally and can be compared with the experimental data in Chapter 3.

Appendices

Appendix A - Method of Measuring Deposit Thickness on Cold Finger

The location of the gel-oil interface (and thus the deposit thickness) was determined from analyzing images taken from video recording the deposition process. This technique was made possible by the clear boundary that exists between the gel and the oil. This technique will not work for oil that is not transparent, which will be the case, for example, if the oil temperature is below the WAT. A conversion factor is needed to convert the apparent deposit thickness as seen in snapshots from the video into actual deposit thickness because light refracts as it travels through different media (oil, glass, and water) and because of the glass curvature. The relationship between apparent and actual deposit thickness was obtained from a photograph of a ruler with length comparable to the diameter of the jacketed vessel placed inside the jacketed beaker filled with mineral oil. The relationship between apparent and actual deposit thickness was verified by comparing deposit mass calculated based on deposit thickness with the deposit mass measured directly at the end of an experimental run (Figure A-I).

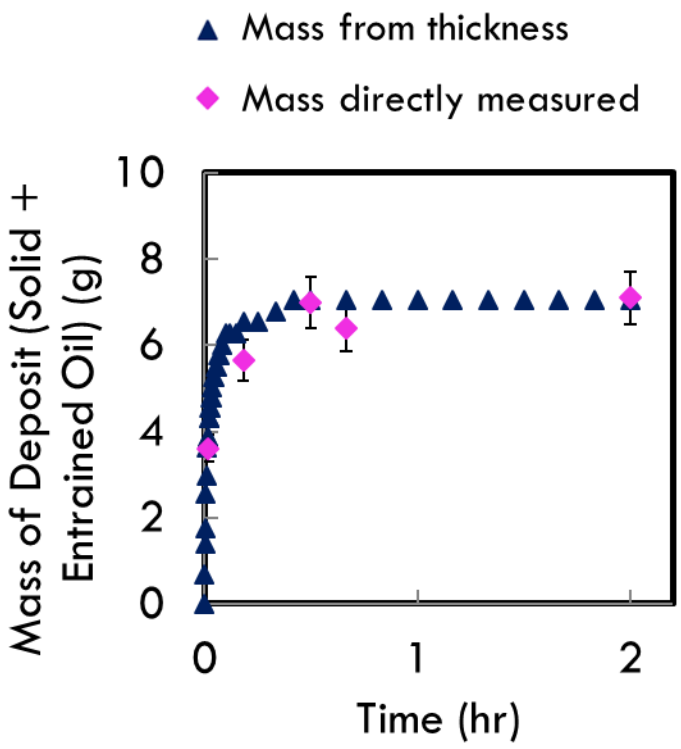

Figure A- I: Mass of deposit measured at the end of an experimental run (magenta diamonds) compared to the mass calculated from measured thickness (dark blue triangles). The two techniques are in agreement.

Appendix B - Thermodynamic Model by Coutinho

The Coutinho model was used to calculate the soluble wax concentration at equilibrium, i.e. solubility limit. The model employs Equation B-1 to calculate the Gibbs free energy difference between the solid and liquid phases.

$$\Delta G_{liquid \rightarrow solid} = \frac{\Delta H_m}{R T_m}\left(\frac{T_m}{T} - 1\right) + \frac{\Delta H_{tr}}{R T_{tr}}\left(\frac{T_{tr}}{T} - 1\right) \tag{B-1}$$

Here, ΔH_m is the specific heat of fusion, T_m is the melting point, and the subscript tr refers to the transition point. Once $\Delta G_{liquid \rightarrow solid}$ is calculated, the distribution of wax between the solid and liquid phases can be determined using Equation B-2.

$$\Delta G_{liquid \rightarrow solid} = -RT \ln \frac{s_i \gamma_i^S}{x_i \gamma_i^L} \tag{B-2}$$

s_i and x_i are the solid and liquid molar fractions of component i, whereas γ_i^S and γ_i^L are the solid and liquid phase activity coefficients of component i, and R is the gas constant. The liquid phase activity coefficient is based on the Flory free volume theory which takes into account entropy effects as well as free volume effects. These considerations are reflected in Equations B-3 and B-4.

$$\ln \gamma_i^L = \ln \frac{\phi_i}{x_i} + 1 - \frac{\phi_i}{x_i} \tag{B-3}$$

$$\phi_i = \frac{x_i\left(V_i^{\frac{1}{3}} - V_{wi}^{\frac{1}{3}}\right)^{3.3}}{\Sigma x_j\left(V_j^{\frac{1}{3}} - V_{wj}^{\frac{1}{3}}\right)^{3.3}} \tag{C-4}$$

V_i and V_{wi} are the molar volume and the Van der Waals volume of component i. For the solid phase activity coefficient, one of the approaches used by Coutinho is using the Wilson model. The Wilson model is not as comprehensive as the UNIQUAC model that resolves different solid phases, but we found that the Wilson model is sufficient in capturing the behaviors resolved by our experiments. The Gibbs excess energy from the Wilson equation can be manipulated to reach the following relationship between the molar composition and the solid activity coefficient of component i, γ_i^S:

$$\ln \gamma_i^S = -\ln\left(\Sigma_j \Lambda_{ij} x_j\right) + 1 - \Sigma_j \frac{\Lambda_{ji} x_j}{\Sigma_k \Lambda_{jk} x_k} \tag{B-5}$$

Here, Λ_{ij} is given by Equations (B-6) through (B-8).

$$\Lambda_{ij} = \exp\left(-\frac{\lambda_{ij} - \lambda_{ii}}{RT}\right) \tag{B-6}$$

$$\lambda_{ii} = -\frac{1}{3}\left(\Delta \mathrm{H}_{sub,i} - RT\right) \tag{B-7}$$

$$\lambda_{ij} = \alpha_{ij} \min\left(\lambda_{ii}, \lambda_{jj}\right) \tag{B-8}$$

$\Delta \mathrm{H}_{sub,i}$ is the heat of sublimation of component i. Using this model, the solubility curve such as shown in Figure 2-1 can be generated.

Bibliography

1. EIA. *Fossil Fuels Still Dominate U.S. Energy Consumption despite Recent Market Share Decline - Today in Energy - U.S. Energy Information Administration (EIA)*.; 2016. https://www.eia.gov/todayinenergy/detail.php?id=26912.

2. Cusick D. Fossil Fuel Use Continues to Rise. *Sci Am*. October 2013. https://www.scientificamerican.com/article/fossil-fuel-use-continues-to-rise/.

3. McFarland A. *In 2018, the United States Consumed More Energy than Ever Before*.; 2019. https://www.eia.gov/todayinenergy/detail.php?id=42335.

4. Musser BJ, Kilpatrick PK. Molecular characterization of wax isolated from a variety of crude oils. *Energy and Fuels*. 1998. doi:10.1021/ef970206u

5. Singh P, Venkatesan R, Fogler HS, Nagarajan N. Formation and aging of incipient thin film wax-oil gels. *AIChE J*. 2000;46(5):1059-1074. doi:10.1002/aic.690460517

6. Singh P, Venkatesan R, Scott Fogler H, Nagarajan NR. Morphological evolution of thick wax deposits during aging. *AIChE J*. 2001. doi:10.1002/aic.690470103

7. Huang Z, Lee HS, Senra M, Scott Fogler H. A fundamental model of wax deposition in subsea oil pipelines. *AIChE J*. 2011. doi:10.1002/aic.12517

8. Burger ED, Perkins TK, Striegler JH. Studies of Wax Deposition in the Trans Alaska Pipeline. *JPT, J Pet Technol*. 1981. doi:10.2118/8788-PA

9. Weingarten JS, Euchner JA. METHODS FOR PREDICTING WAX PRECIPITATION AND DEPOSITION. *SPE Prod Eng*. 1988. doi:10.2118/15654-pa

10. Cabanillas JP, Leiroz AT, Azevedo LFA. Wax Deposition in the Presence of Suspended Crystals. *Energy and Fuels*. 2016. doi:10.1021/acs.energyfuels.5b02344

11. Navaneetha Kannan S, Daraboina N, Venkatesan R, Sarica C. Settling and re-entrainment of wax particles in near-gelling systems. *AIChE J*. 2018. doi:10.1002/aic.15948

12. Golchha A, Sarica C, Venkatesan R. Settling of wax particles in near-gelling systems under quiescent conditions. In: *Proceedings of the Annual Offshore Technology Conference*. ; 2015. doi:10.4043/25652-ms

13. Singh P, Fogler HS, Nagarajan N. Prediction of the wax content of the incipient wax-oil gel in a pipeline: An application of the controlled-stress rheometer. *J Rheol (N Y N Y)*. 1999. doi:10.1122/1.551054

14. Zheng S, Saidoun M, Mateen K, Palermo T, Ren Y, Fogler HS. Wax deposition modeling with considerations of non-Newtonian fluid characteristics. In: *Proceedings of the Annual Offshore Technology Conference*. ; 2016.

15. Zheng S, Saidoun M, Palermo T, Mateen K, Fogler HS. Wax Deposition Modeling with Considerations of Non-Newtonian Characteristics: Application on Field-Scale Pipeline. *Energy and Fuels*. 2017. doi:10.1021/acs.energyfuels.7b00504

16. Venkatesan R, Nagarajan NR, Paso K, Yi YB, Sastry AM, Fogler HS. The strength of paraffin gels formed under static and flow conditions. *Chem Eng Sci*. 2005. doi:10.1016/j.ces.2005.02.045

17. Dimitriou CJ, McKinley GH. A comprehensive constitutive law for waxy crude oil: A thixotropic yield stress fluid. *Soft Matter*. 2014. doi:10.1039/c4sm00578c

18. Geri M, Venkatesan R, Sambath K, McKinley GH. Thermokinematic memory and the thixotropic elasto-viscoplasticity of waxy crude oils. *J Rheol (N Y N Y)*. 2017. doi:10.1122/1.4978259

19. Kané M, Djabourov M, Volle JL. Rheology and structure of waxy crude oils in quiescent and under shearing conditions. In: *Fuel*. ; 2004. doi:10.1016/j.fuel.2004.01.017

20. Fong N, Mehrotra AK. Deposition under turbulent flow of wax-solvent mixtures in a bench-scale flow-loop apparatus with heat transfer. In: *Energy and Fuels*. ; 2007. doi:10.1021/ef0603784

21. Bidmus H, Mehrotra AK. Measurement of the liquid-deposit interface temperature during solids deposition from wax-solvent mixtures under static cooling conditions. *Energy and Fuels*. 2008. doi:10.1021/ef700588y

22. Ehsani S, Mehrotra AK. Validating Heat-Transfer-Based Modeling Approach for Wax Deposition from Paraffinic Mixtures: An Analogy with Ice Deposition. *Energy and Fuels*. 2019. doi:10.1021/acs.energyfuels.8b03777

23. Ehsani S, Haj-Shafiei S, Mehrotra AK. Experiments and modeling for investigating the effect of suspended wax crystals on deposition from ‘waxy’ mixtures under cold flow conditions. *Fuel*. 2019. doi:10.1016/j.fuel.2019.01.089

24. Ehsani S, Mehrotra AK. Effects of shear rate and time on deposit composition in the cold flow regime under laminar flow conditions. *Fuel*. 2020. doi:10.1016/j.fuel.2019.116238

25. Parthasarathi P, Mehrotra AK. Solids deposition from multicomponent wax-solvent mixtures in a benchscale flow-loop apparatus with heat transfer. *Energy and Fuels*. 2005. doi:10.1021/ef0497107

26. Tiwary D, Mehrotra AK. Phase Transformation and Rheological Behaviour of Highly Paraffinic “Waxy” Mixtures. *Can J Chem Eng*. 2008. doi:10.1002/cjce.5450820121

27. Bhat N V., Mehrotra AK. Modeling of deposit formation from “Waxy” mixtures via moving boundary formulation: Radial heat transfer under static and laminar flow conditions. *Ind Eng Chem Res*. 2005. doi:10.1021/ie050149p

28. Bhat N V., Mehrotra AK. Modeling of deposition from “waxy” mixtures in a pipeline under laminar flow conditions via moving boundary formulation. *Ind Eng Chem Res*. 2006. doi:10.1021/ie0601706

29. Tiwary R, Mehrotra AK. Deposition from wax-solvent mixtures under turbulent flow: Effects of shear rate and time on deposit properties. In: *Energy and Fuels*. ; 2009. doi:10.1021/ef800591p

30. Arumugam S, Kasumu AS, Mehrotra AK. Modeling the static cooling of wax-solvent mixtures in a cylindrical vessel. In: *Proceedings of the Biennial International Pipeline Conference, IPC*. ; 2012. doi:10.1115/IPC2012-90691

31. Kasumu AS, Mehrotra AK. Solids deposition from two-phase wax-solvent-water “waxy” mixtures under turbulent flow. In: *Energy and Fuels*. ; 2013. doi:10.1021/ef301897d

32. Kasumu AS, Mehrotra AK. Solids deposition from wax-solvent-water “waxy” mixtures using a cold finger apparatus. *Energy and Fuels*. 2015. doi:10.1021/ef501835b

33. Coutinho JAP. A thermodynamic model for predicting wax formation in jet and diesel fuels. *Energy and Fuels*. 2000. doi:10.1021/ef990203c

34. Huang Z, Zheng S, Fogler HS. *Wax Deposition : Experimental Characterizations, Theoretical Modeling, and Field Practices*.; 2015.

35. Lu Y, Huang Z, Hoffmann R, Amundsen L, Fogler HS. Counterintuitive effects of the oil flow rate on wax deposition. In: *Energy and Fuels*. ; 2012. doi:10.1021/ef3002789

36. Bidmus H, Mehrotra AK. Measurement of the liquid-deposit interface temperature during solids deposition from wax-solvent mixtures under sheared cooling. *Energy and Fuels*. 2008. doi:10.1021/ef800542a

37. Paso KG, Fogler HS. Bulk stabilization in wax deposition systems. *Energy and Fuels*. 2004. doi:10.1021/ef034105+

38. Quan Q, Gong J, Wang W, Gao G. Study on the aging and critical carbon number of wax deposition with temperature for crude oils. *J Pet Sci Eng*. 2015. doi:10.1016/j.petrol.2015.03.026

39. Singh P, Youyen A, Fogler HS. Existence of a critical carbon number in the aging of a wax-oil gel. *AIChE J*. 2001. doi:10.1002/aic.690470921

40. Haj-Shafiei S, Serafini D, Mehrotra AK. A steady-state heat-transfer model for solids deposition from waxy mixtures in a pipeline. *Fuel*. 2014. doi:10.1016/j.fuel.2014.07.098

41. Arumugam S, Kasumu AS, Mehrotra AK. Modeling of solids deposition from “waxy” mixtures in “hot flow” and “cold flow” regimes in a pipeline operating under turbulent flow. *Energy and Fuels*. 2013. doi:10.1021/ef401315m

42. Bidmus HO, Mehrotra AK. Solids deposition during “cold flow” of wax-solvent mixtures in a flow-loop apparatus with heat transfer. *Energy and Fuels*. 2009. doi:10.1021/ef900224r

43. Mahir LHA, Vilas Bôas Fávero C, Ketjuntiwa T, Fogler HS, Larson RG. Mechanism of Wax Deposition on Cold Surfaces: Gelation and Deposit Aging. *Energy and Fuels*. 2019;33(5):3776-3786. doi:10.1021/acs.energyfuels.8b03139

44. Hayduk W, Minhas BS. Correlations for prediction of molecular diffusivities in liquids. *Can J Chem Eng*. 1982. doi:10.1002/cjce.5450600213

45. Cussler EL, Hughes SE, Ward WJ, Aris R. Barrier membranes. *J Memb Sci*. 1988. doi:10.1016/S0376-7388(00)80877-7

46. Crank J. *Free and Moving Boundary Problems*. Clarendon Press, Oxford; 1984.

47. Crank J, Nicolson P. A practical method for numerical evaluation of solutions of partial differential equations of the heat-conduction type. *Math Proc Cambridge Philos Soc*. 1947. doi:10.1017/S0305004100023197

48. Rice RG, Do DD. *Applied Mathematics and Modeling for Chemical Engineers*. 2nd Editio. Hoboken, NJ: Wiley; 2012.

49. Mahir LHA, Vilas Bôas Fávero C, Ketjuntiwa T, Fogler HS, Larson RG. Mechanism of Wax Deposition on Cold Surfaces: Gelation and Deposit Aging. *Energy and Fuels*. 2019. doi:10.1021/acs.energyfuels.8b03139

50. Huang Z. Application of the Fundamentals of Heat and Mass Transfer to the Investigation of Wax Deposition In Subsea Pipelines. 2011. http://hdl.handle.net/2027.42/89634.

51. Versteeg GF, Blauwhoff PMM, van Swaaij WPM. The effect of diffusivity on gas-liquid mass transfer in stirred vessels. Experiments at atmospheric and elevated pressures. *Chem Eng Sci*. 1987. doi:10.1016/0009-2509(87)80060-X

52. Coutinho JAP, Stenby EH. Predictive local composition models for solid/liquid equilibrium in n-alkane systems: Wilson equation for multicomponent systems. *Ind Eng Chem Res*. 1996. doi:10.1021/ie950447u

53. Coutinho JAP, Edmonds B, Moorwood T, Szczepanski R, Zhang X. Reliable wax predictions for flow assurance. *Energy and Fuels*. 2006. doi:10.1021/ef050082i